Intermittent Drug Treatment of BRAF^{V600E} Melanoma Cells Delays Resistance by Adaptive Resensitization to Drug Rechallenge

by

Andrew J. Kavran

B.S., Montana State University, 2015

A thesis submitted to the

Faculty of the Graduate School of the

University of Colorado in partial fulfillment

of the requirements for the degree of

Doctor of Philosophy

Department of Biochemistry

2021

Committee Members:

Natalie Ahn, Chair

Aaron Clauset

Xuedong Liu

Sabrina Spencer

Tin Tin Su

Kavran, Andrew J. (Ph.D., Biochemistry)

Intermittent Drug Treatment of $BRAF^{V600E}$ Melanoma Cells Delays Resistance by Adaptive Resensitization to Drug Rechallenge

Thesis directed by Prof. Natalie Ahn and Prof. Aaron Clauset

Melanoma patients receiving drugs targeting BRAFV600E and MEK1/2 invariably develop resistance and continue progression. Based on preclinical studies, intermittent treatment involving alternating periods of drug withdrawal and rechallenge has been proposed as a method to delay the onset of resistance. The beneficial effect of intermittent treatment has been attributed to drug addiction, where drug withdrawal reduces the viability of resistant cells due to MAP kinase pathway hyperactivation. However, the mechanistic basis of the intermittent effect is incompletely understood. We show that intermittent treatment with the $BRAF^{V600E}$ inhibitor, LGX818/encorafenib, suppresses growth compared to continuous treatment in human melanoma cells engineered to express $BRAF^{V600E}$, p61-$BRAF^{V600E}$, or $MEK2^{C125S}$ oncogenes. While drug addiction is clearly observable, it fails to account for the advantageous effect of intermittent treatment. Instead, growth suppression is best explained by resensitization during periods of drug removal, followed by cell death after drug readdition. Continuous treatment leads to transcriptional responses prominently associated with chemoresistance in melanoma. By contrast, cells treated intermittently reveal a subset of transcripts that switch between successive cycles of drug removal and rechallenge, and reverse the expression of some, but not all, mediators of cell invasiveness and the epithelial to mesenchymal transition. These transcripts change during periods of drug removal by adaptive phenotype switching, rather than selection pressure. Resensitization occurs against a background of sustained expression of melanoma resistance genes, producing a transcriptome distinct from that of the initial drug-naïve cell state. We conclude that phenotypic plasticity leading to drug resensitization can underlie the beneficial effect of intermittent treatment.

Large-scale biological data sets are often contaminated with noise, which can impede accurate

inferences about the underlying processes. We describe a general method for automatically reducing noise in large-scale biological data sets. These network filters use an interaction network to identify groups of correlated or anti-correlated measurements that can be combined to better recover an underlying biological signal, similar to image denoising. Applied to synthetic and real data sets, network filters accurately decrease the noise and improve the accuracy of machine learning tasks. Our results indicate the broad potential utility of network filters to applications in systems biology.

Acknowledgements

Completing the projects in this thesis would not be possible without my advisors Natalie Ahn and Aaron Clauset who have guided me through graduate school and helped me to become an independent scientist and thinker. You two are excellent scientists and mentors with such broad and deep command of science, I hope to emulate you both someday. To the rest of my thesis comittee: Xuedong Liu, Sabrina Spencer, and Tin Tin Su, thank you for your guidance along the way. The experiments and analyses you suggested and the reagents and cell lines you've provided have made my work much stronger.

Theresa Nahreini and Joe Dragavon cannot be thanked enough for their dedication to make the cell culture, flow cytometry, and microscopy facilities run smoothly. This department could truly not function without them. To all my lab mates past and present, thank you for all the input and fun times along the way. Scott Stuart and MK Connacher deserve special thanks for training me to be a good bench scientist. They taught me all those little things you have to do in a protocol that no body writes down, and I'm sure this has saved me months of repeating experiments that would have otherwise failed.

To the IQ Biology staff especially Kristen Powell, Amber McDonald, and Andrea Stith. Thank you for leading such an excellent program that gave me the foundation to conduct interdisciplinary science. IQ Biology is so important to train the next generation of biological scientists, and I look forward to seeing how you evolve the program. Also to the Biochemistry staff, especially Pamela Williamson who helped me transition from IQ Biology to the biochemistry department.

My wonderful Mom and Dad, sister and brothers, nephew and nieces have been there for me

every step of the way. They are an endless source of entertainment, fun stories, and relief from grad school. I love spending time with you, especially when we go off on big family vactions to Australia, Hawaii, and Disney World.

For all the friends I met along the way through grad school, especially Graycen Wheeler and Kelsie Anson. Spending every week of COVID times on zoom watching Drag Race, playing Stardew Valley, or just hanging out have kept me sane this past year. And thank you for groaning "BOOOOO" whenever I make a terrible pun.

And of course to my boyfriend, Tom Rivas. I can't begin to express my appreciation for you and how you've changed me. I could not have finished my PhD if not for your constant love and support. Thank you for laughing at my bad jokes. I love you and can't wait to go on more adventures with you.

Contents

Chapter

Tables

Table

Figures

Figure

Chapter 1

Introduction

1.1 Melanoma disease statistics, biology, and disease progression

Cutaneous melanoma is a cancer originating from melanocytes in the skin. This cancer is relatively less common than other skin cancers, accounting for only 1-4% of all skins cancer cases. However, it the most deadly form making up 75% of yearly skin cancer deaths [1,2]. Year after year, cutaneous melanoma diagnoses are becoming more common in the United States. The incidence rate in 1980 was 10.5 per 100,000, and it has more than doubled in 2018 to 25.3 [3]. While the overall 5-year relative survival of melanoma from 2011-2017 was 93%, the key to surviving melanoma is early detection. If the cancer has not spread from the primary site, the disease is typically cured by resecting the nevus with a 99.4% 5-year relative survival rate. Once the cancer metastasizes in stage later stages, the survival rate sharply drops. Patients with regional lymph node metastases have a 5-year relative survival is 68%, and with distant metastases it decreases to 29.8% [3].

The typical first step in melanoma neoplastic transformation is ultraviolet radiation induced mutagenesis. The most frequently transforming mutation is in the BRAF kinase (discussed in section 1.2.1). Transformed melanocytes clonally expand and form a nevus (Fig. 1.1) [4,5]. However, the BRAF mutation alone typically does not cause cancer due to oncogene induced senescence. After a few days of clonal expansion, the negative regulator of the G1-S cell cycle transition $p16^{INK4a}$ is increased [6]. However, the upregulation of $p16^{INK4a}$ may not be the driving force of oncogene induced senescence [7, 8]. Inflammatory cytokines IL6 and IL8 may also play a role in activating senescence pathways [9].

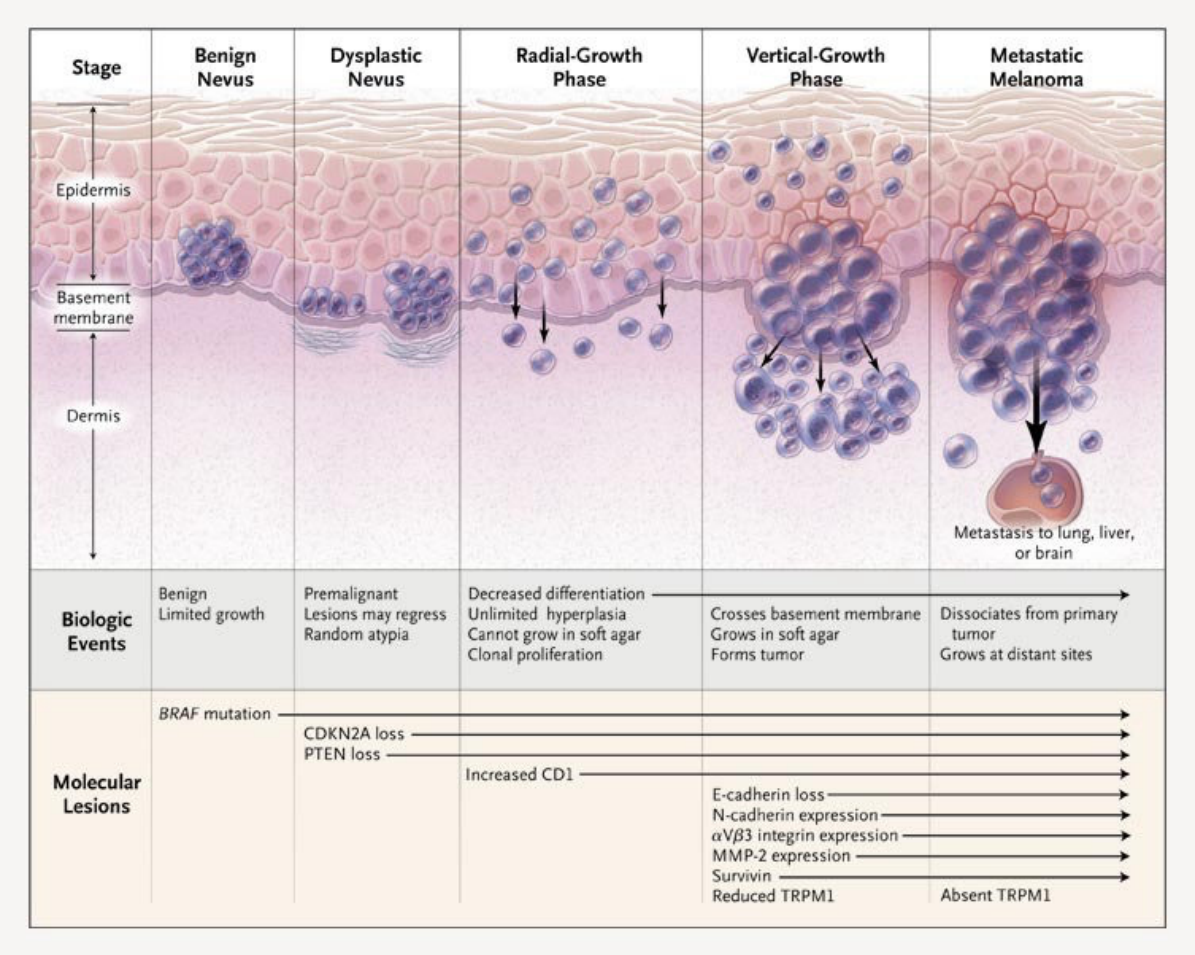

Figure 1.1: Model of spontaneous melanoma disease progression. Melanomas progress in a step-like manner from a benign overgrowth of a nevus to distant metastasis. Cells acquire prototypical mutations at each step, which are associated with UV radiation. Reproduced with permission from [2], Copyright Massachusetts Medical Society.

The next step in melanoma progression involves mutations in CDKN2A or PTEN. CDKN2A is the gene that codes for the $p16^{INK4a}$ tumor supressor protein. This gene is mutated in 30-40% of familial forms of melanoma [10]. On the other hand, PTEN loss of function mutations are much more common in spontaneous melanomas resulting from sun damage. The PTEN phosphatase negatively regulates the PI3K/AKT signaling pathway, which is a cell signaling pathway important for cell survival and proliferation [2]. Loss of function in these genes helps to activate abberant cell proliferation (Fig. 1.1).

In the radial growth phase of melanoma, the cells invade farther in the dermal layers of the skin but they do extend into the subcutaneous fat level. They develop over-expression of the cell-cycle protein, cyclin D1, which accelerates their proliferation (Fig. 1.1) [11]. Then in the vertical growth phase, the cells invade deeper into the skin layers and start migrating to the lymph nodes (Fig. 1.1). The tumor cells in this phase undergo a transition similar to the epithelial to mesenchymal transition (EMT) seen in epithelial cancers and during normal development. A switch from the cellular adhesion protein E-cadherin to N-cadherin is a classical step in EMT and is seen in melanoma [12]. Additionally, expression of the intermediate filament vimentin, a classical marker of mesenchymal cells, is expressed during this stage [12]. At this stage the signaling ligand WNT5A becomes highly expressed, which makes melanoma cells more motile and may initiate the EMT process [13, 14]. Finally, in metastatic melanoma, satellite tumors form in the brain, lungs, and liver.

1.2 Mitogen activated protein kinase (MAPK) signaling pathway

All cells integrate extracellular signals to respond and adapt to their environment. Perhaps the most studied mammalian signaling pathway is the mitogen activated protein kinase (MAPK) pathway [15]. This pathway is highly conserved throughout Eukaryotes, but it is absent in Archaea and Bacteria. In normal, non-cancerous cells, secreted extracellular proteins bind to membrane proteins on target cells acting as a signal to enter the cell-cycle and grow. As this pathway is important for cell proliferation, it is highly dysregulated in many human cancers and a frequent target of oncogenic mutations [16]. In melanoma specifically, about 90% of cases have an oncogenic mutation in one of the MAPK pathway proteins [17].

The signal transduction of extracellular cues to the cytoplasm and nucleus have been studied deeply for decades. One defining characteristic of the pathway architecture is the three-tiered kinase cascade. This means one kinase phosphorylates and activates a second kinase, which then goes on to do the same for the third, master kinase. The biochemical details of the proteins and signal transduction of the MAPK pathway are described in the following sections.

1.2.1 RAFs

The RAFs lie at the top of the three tiered kinase cascade. Also called MAP3Ks, these proteins phosphorylate the MEKs. Structurally, there are 3 conserved regions. The N-terminal conserved region is composed of a RAS-binding domain (RBD) and cysteine rich region [18]. Like its name indicates, the RBD will bind to Ras at the plasma membrane and release the protein from its autoinhibited conformation. The protein can also undergo phosphorylation which fully activates its kinase activity.

There are three isoforms in mammals, called A, B, and C. BRAF is particularly important in human cancer as it is mutated in about 15% of all types of cancer. In particular, over 50% of melanomas have a mutation in BRAF. Valine 600 is the most common site of mutagenesis, with glutamate being the substitution in 80% of tumors [17, 19]. This residue lies in between the activation loop phosphosites at T599 and S602 [18], and the charged residue likely mimics the effect of phosphorylation [19].

1.2.2 MEKs

The MAP Kinase Kinases (MEKs, MKKs, or MAP2Ks) are the intermediate step of the MAPK pathway. These kinases have dual specificity for tyrosine and threonine residues that activate the master kinase ERK [20]. RAFs classically activate the MEKs through phosphorylation on two serine residues, but other proteins like c-MOS can also activate MEK [21, 22]. The concentration of MEK in cells is thought to be the key to if cells display graded or switch-like MAPK pathway activation [23]. Constitutive activation mutations in MEKs are sufficient to transform cells [24].

1.2.3 ERKs

The final kinase of the MAPK pathway are the MAP kinases themselves. Commonly known as ERK1/2, these kinases have hundred of phosphorylation targets in the cytoplasm and nucleus [25, 26]. The targets themselves have a broad range of molecular classes from transcription factors,

cytoskeletal elements, apoptotic proteins, kinases, and phosphatases.

One of the most well known functions is the promotion of cell proliferation through stimulating transcription of cyclin D1 [27] to enter the cell cycle. The cyclin D1 gene promoter has AP-1 sites that immediate early ERK targets FOS and JUN can bind [28, 29]. Traditionally, MAPK signaling was only considered important during G1-S phase transition where the restriction-point is, but more recent evidence shows that cells sense MAPK signaling throughout the whole cell cycle [30]

Another critical function of ERKs is pro-survival cell signaling. ERK regulates the transcription and phosphorylation of some BCL-2 family proteins [31]. In particular, ERK reduces the transcription of pro-apoptotic protein BIM. ERK phosphorylates and inhibits the transcription factor FOXO3A, which normally induces BIM transcription. Furthermore, BIM has ERK phosphorylation sites, which prevent it from binding other pro-apoptotic proteins and also targets it for degradation [32].

While ERK is the most important kinase of the MAPK pathway, only a few cancer causing mutations have been identified. The mutants E322K and D319N in ERK2 occurs in the common docking (CD) binding motif where ERK binds its substrates and negative regulators [33,34]. Recent studies have shown that these may inhibit interactions with phosphatases that normally inactivate ERK [35].

1.2.4 Upstream effectors and oncogenic mutations

Cells with $BRAF^{V600E}$ mutations have constitutive MAPK pathway activation without the need for external signals. But protein components at the plasma membrane are necessary to start the signal cascade in $BRAF^{WT}$ cells, and some are these proteins have oncogenic mutations in melanoma. The first step in MAPK signal transduction is receptor tyrosine kinases (RTK) binding to growth factors and mitogens on the extracellular side of cells. This binding induces dimerization and cross-phosphorylation of tyrosine residues [36,37]. The most relevant RTK in many cancer cells is EGFR, as it can contribute the oncogenesis and malignancy [38]. While oncogenic mutations in EGFR are not common in melanoma, they are important for lung cancer. Particularly the EGFR

mutation L858R promotes aggressive late-stage cancer [39].

The phosphorylation on EGFR is recognized by SHC and GRB2 by their SH2 domains [40]. GRB2 interacts through its SH3 domain with the G-protein guanine exchange factor (GEF) SOS and promotes its localization to the plasma membrane [41]. There, it is able to activate the small monomeric GTPase RAS by promoting its exchange of GDP for GTP.

RAS is one of the most frequently mutated proteins in human cancer, with estimates between 16% and 27% across all cancers [42]. These are most common in the isoform KRAS, followed by isoforms NRAS and HRAS. In melanoma, mutations in NRAS accounts for about 25% of cases and they are frequently somatic [17]. Oncogenic mutations in BRAF and NRAS are largely mutually exclusive in patients before drug treatment. There are three hotspots for RAS mutations: G12, G13, and Q61 [42]. Mutations of these residues reduce GTP hydrolysis and/or exchange rate [43]. Hence these mutations create a hyperactive RAS by promoting its association with GTP. Different cancer types preferentially mutate specific RAS isoforms and hotspot codons. In melanoma, NRAS is most frequently mutated at glutamine 61 to either arginine, lysine, leucine, or histidine [17].

RAS signaling is regulated through a GTPase activating protein (GAP). These proteins enhance the GTPase activity of RAS and consequently convert RAS into its inactive GDP bound form. The relevant RAS GAP in melanoma is called NF1 [44, 45]. This tumor suppressor protein has loss of function mutations in about 15% of melanoma cases, and it sometimes co-occurs with BRAF mutations [17]. Thus, NF1 mutant melanomas also have upregulated MAPK signaling though the suppression of negative pathway regulation.

1.3 MAPK pathway targeted therapies

Until the early 2010s, the treatment options for metastatic melanoma were limited, and patients did not respond well. The only FDA approved therapies were dacarbazine and interleukin-2 (IL2) [46]. But therapies targeted to the MAPK pathway have revolutionized treatment and extended the progression free survival of patients [47]. With about 90% of melanomas harboring a mutation in the MAPK pathway, the pathway clearly is important for cancer cell fitness and

inhibiting it has lead to beneficial therapeutic responses.

Vemurafenib was the first FDA approved BRAF inhibitor (BRAFi) for metastatic melanoma [48]. This ATP competitive inhibitor preferentially binds to $BRAF^{V600E}$ and other active mutants over inactive $BRAF^{WT}$ [49]. Dabrafenib was FDA approved next. This drug has a similar profile to vemurafenib, but is more selective for $BRAF^{V600E}$ mutants than $BRAF^{WT}$ or CRAF [50]. Encorafenib is the latest FDA approved BRAF inhibitor, and its very slow dissociation rate (half-life $\approx$ 30 h) from $BRAF^{V600E}$ and higher specificity set it apart from vemurafenib and dabrafenib [51]. While these inhibitors show potent activity in $BRAF^{V600E}$ and other activating mutants, they can actually lead to so called "paradoxical activation" of the MAPK pathway at subsaturating concentrations in $BRAF^{WT}$ cells. The inhibitors can bind to $BRAF^{WT}$ and $CRAF^{WT}$ and induce a conformation that allows dimerization and activation of the non-ligand-bound protomer [52].

Since these BRAF inhibitors are not effective for $BRAF^{WT}$ cancers, MEK inhibitors are used for RAS mutant cancers and as a double agent therapy with BRAFi. There are three currently FDA approved MEK inhibitors (MEKi) used to treat metastatic melanoma: Cobimetinib, Trametinib, and Binimetinib. Unlike the BRAF inhibitors, these are allosteric inhibitors [53]. They bind to a site adjacent to the ATP nucleotide and favor an inactive conformation [54]. Current first line of care of metastatic melanoma involves BRAFi and MEKi combination treatment. Patients receiving encorafenib and binimetinib combination treatment have a median 15 month progression free survival, and median 33 month overall survival [55].

1.4 Acquired drug resistance to targeted therapies

While many patients will respond to BRAF or MEK inhibition, nearly all patients will develop resistance and relapse [56]. This acquired drug resistance is distinct from intrinsic resistance, where about 50% patients do not respond to drug treatment [57]. Acquired resistance to MAPK pathway inhibitors typically comes in the form of reactivating the MAPK pathway under drug treatment. A common acquired resistance mechanism is BRAF amplification [58]. The consequence of amplification is that there is an excess of uninhibited BRAF that can stimulate the pathway.

Increasing drug concentrations can inhibit MAPK signaling in BRAF amplified cells *in vitro* but at dosages too high for patients [58].

A splice variant of $BRAF^{V600E}$ has been identified in patients that can confer resistance to BRAF inhibitors. Called p61-$BRAF^{V600E}$, this variant has a truncated C-terminal domain with loss of the RAS binding domain [59]. Truncation of the RBD promotes homo-dimerization and subsequent activation of the MAPK pathway. Vemurafenib, Dabrafenib, and Encorafenib can inhibit monomeric $BRAF^{V600E}$, but due to negative cooperativity, they do not efficiently inhibit dimers [60, 61].

Mutations in MEK may reactivate the MAPK pathway to confer drug resistance. The C125S mutation in MEK2 creates a hyperactive mutant that promotes ERK phosphorylation [62, 63]. Introducing MEK mutations to *in vitro* cell culture models show that MEK^{C125S} cell lines have at least a 100 fold shift in the drug concentration that inhibits 50% of growth (IC_{50}) for both Dabrafenib and Trametinib compared to $BRAF^{V600E}$ [63]. However, the MEK^{C125S} mutant cell line was equally sensitive to downstream interference of the pathway by the ERK1/2 inhibitor Vertex-11e, indicating the promise of triple agent therapy (BRAFi, MEKi, ERKi) to counter drug resistance.

While NRAS and BRAF mutations appear mutually exclusive in pre-treatment tumors, patients with BRAF mutant tumors may acquire NRAS mutations to resist drug treatment [62, 64]. While $BRAF^{V600E}$ may still be inhibited in these tumors, NRAS can signal in parallel through CRAF to reactivate ERK signaling.

1.5 Non-mutational mechanisms of drug tolerance

Before cells acquire irreversible genomic drug resistance mechanisms, BRAFi and/or MEKi treatment induces non-mutational changes in melanoma cells that allow them to survive and proliferate. This non-mutational adaption is typically called drug tolerance, while mechanisms involving genomic changes like mutations, and copy number variants are drug resistance. The time scale of drug tolerance is much quicker than drug resistance, on the order of hours to weeks. True drug

resistance is developed within several months [65]. Drug tolerant cells are prone to DNA damage, which might enhance the acquisition of drug resistance mechanisms [66].

One mechanism of drug tolerance induced very quickly after drug treatment is the relief of MAPK pathway negative feedback. Under constitutive $BRAF^{V600E}$ signaling, negative regulators of the pathway are upregulated, such as SPRY, DUSP, and MIG6. Transcription of these genes is downregulated upon BRAFi. Consequently, cells become responsive to RTK signaling through NRAS and CRAF and reactivate the pathway [67]. A recent study by Gerosa et al. show in BRAFi treated melanoma cells ERK activation is pulsitile and driven by secreted paracrine factors [68]. This was evidenced spikes in ERK activation by cells close together spatially, and also treatment with several different RTK inhibitors. Inhibition of this receptor driven signaling significantly reduced cell growth compared to BRAFi alone.

In the longer term, melanoma cells undergo transcriptional reprogramming to tolerate drug treatment. It is now widely accepted that melanoma cells exist in (at least) two different transcriptional states [69, 70]. The "proliferative" state is characterized by high expression of melanocytic differentiation transcription factors SOX10 and MITF and downstream target genes MLANA and TYR. The "invasive" cell state is de-differentiated and expresses neural crest lineage marker NGFR, high RTK expression like AXL, EGFR, and high WNT5A. The proliferative/invasive state distinction has repeatedly been shown to be be predictive of drug tolerance in melanoma cells [71–77]. This phenotype switching is similar to the epithelial to mesenchymal transtion seen in other cancers and is a drug tolerance mechanism [78–80].

Besides a switch in MITF mediated transcription, another mechanism driving this transcriptional state and drug sensitivity is a change is a switch in transcription factors LEF1 and TCF4 [81]. These transcription factors are associated with the WNT signalling, and are differentially expressed in the proliferative and invasive states. LEF1 is higher in the proliferative state, and has been shown to be down regulated in patients with BRAFi refractory tumors [82]. This is associated with signaling through the cannonical WNT/β-catenin pathway, which enhances BRAFi induced apoptosis [83, 84]. The non-cannonical WNT pathway, driven by WNT5A, drives down-

regulation of LEF1 and increased expression of TCF4 [81]. Signaling through WNT5A has a long standing association with drug resistance and invasion in melanoma [72, 85]

1.6 Intermittent drug treatment in melanoma

In a landmark study, Das Thakur et al. show that alternating periods of drug removal and drug addition of melanoma patient derived xenograph (PDX) mice lead to delayed resistance to the BRAF inhibitor vemurafenib [86]. These melanoma tumors had a BRAF amplification that made the tumors resistant to continuous drug treatment, but still susceptible to intermittent treatment where mice were dosed 4 weeks on drug followed by a 2-week drug holiday (i.e. no drug treatment). The researchers found that these cells had a bi-phasic growth response to vemurafenib. At very high and very low concentrations of vemurafenib, the cells showed reduced fitness compared to intermediate concentrations of drug. The resistant cells also showed higher phosphoERK levels compared to the parental sensitive tumor cells.

Through these observations, the study proposed a model to explain why intermittent treatment was more beneficial than continuous treatment. Drug treatment selects for cells that can re-activate the MAPK pathway under drug treatment. These cells out grow under continuous inhibitor treatment, allowing the disease to progress. When drug is removed from drug resistant cells, this creates a selection pressure against them and they lose fitness. Drug removal also creates a positive selection for drug sensitive cells to re-emerge, making the tumor once again sensitive to drug treatment. This alternating selection between drug sensitive and drug resistant cells continues with the alternating periods of drug treatment and drug withdrawal.

The phenomenon that drug resistant melanoma cells show hampered fitness in the absence of inhibitor, compared to intermediate inhibitor concentrations has been termed “drug addiction”. Other studies have further characterized the molecular mechanisms of melanoma drug addiction. Through an unbiased CRISPR-Cas9 screen, Kong et al. found that knockout of ERK2, but not ERK1, rescued the drug addiction phenotype [87]. Knocking out the AP-1 transcription factors JUNB and FRA1 (encoded by FOSL1) also rescued drug addiction. This is supported by another

study that found JUNB and FRA1 were increased in drug addicted cells upon drug removal [88]. Kong et al. further show that cells undergo a phenotype switch from a melanocytic, proliferative state to a neural-crest like invasive state upon drug removal. This observation is relatively surprising because most drug resistant melanoma cells are already in an undifferentiated, invasive state. In another study by Leung et al., the researchers performed an shRNA screen against 7,800 genes and found that only shRNAs targeting BRAF and MEK1 significantly reduced the drug addiction phenotype [89]. This lead them to conclude that not one single downstream target of ERK is necessary for drug addiction in contrast with Kong et al. They also found that hyperactive ERK1 and ERK2 can lead to drug addiction. Thus, these contrasting studies demonstrate that different cellular contexts manifest drug addiction in divergent ways. A key piece missing from these studies is how patients' tumors respond after drug withdrawal and rechallenge.

Intermittent dosing has become a promising strategy that may lead to longer responses to targeted therapies. However, there are conflicting studies on whether such a strategy would be widely applicable. Most notably, a phase II clinical trial of metastaic melanoma patients showed that continuous treatment had better progression free survival and intermittent treatment with dabrafenib and trametinib. The study also reported that overall survival was not different between the groups [90]. Despite the disappointing results from this clinical trial, may retrospective and prospective clinical case studies have shown the promise of intermittent dosing. About one third of the total patients in these studies have shown a response to a second rechallenge with drugs after a drug holiday [91–96].

The main project of this thesis is to understand the molecular and cellular mechanisms underlying the beneficial response to intermittent drug treatment. The results from my study may lead to important advances for optimizing patients' responses to intermittent drug treatment.

1.7 Outline of thesis

In Chapter 2 of this thesis, I will describe the work I've done on elucidating the mechanisms of intermittent drug treatment in $BRAF^{V600E}$ melanoma cells. This was done jointly with Scott

Stuart, a former postdoctoral fellow in the lab, and under the mentorship of Natalie Ahn. This work is currently under review at *Proc. Natl. Acad. Sci. USA*. Chapter 3 consists of a computational project to denoise large-scale biological data through network based methods, which has been published (Kavran, A.J., Clauset, A. Denoising large-scale biological data using network filters. *BMC Bioinformatics* 2021;22:157). All computational experiments and coding was done by myself under the mentorship of Aaron Clauset. I will discuss implications of the results of these projects and future directions in Chapter 4.

Chapter 2

Intermittent drug treatment of $BRAF^{V600E}$ melanoma cells delays resistance by adaptive resensitization to drug rechallenge

2.1 Background

The discovery that nearly half of melanomas harbor activating mutations in the protein kinase BRAF led to a breakthrough in the treatment of metastatic melanoma [19, 97]. Inhibitors targeting the most prevalent BRAF mutations, $BRAF^{V600E/K}$, or its downstream targets, MAP kinase kinases 1 and 2 (MEK1/2), show clinical benefit in about 65% of $BRAF^{V600E/K}$-positive melanoma patients when administered continuously [98–100]. However, resistance invariably develops, limiting median overall survival to approximately 2 years [101, 102]. Many resistance mechanisms reactivate the MAP kinase (MAPK) pathway providing a growth advantage in the presence of inhibitor. Known mechanisms include $BRAF^{V600E}$ amplification, alternative splicing of $BRAF^{V600E}$, and other oncogenic mutations (e.g. $MEK2^{C125S}$, $NRAS^{Q61K}$) [58, 59, 64, 101–105]. Adaptive resistance also occurs in the absence of genomic alterations and can involve transcriptional changes through epigenetic mechanisms that promote the epithelial-mesenchymal transition, melanocyte de-differentiation, and neural crest stem cell-like reemergence [73, 74, 76, 77, 82, 106–112].

An emerging body of evidence has suggested that intermittent dosing schedules, in which periods of treatment with targeted therapeutics are interrupted by periods of drug removal, might have advantages over continuous treatment [91, 97, 113]. Preclinical studies with patient-derived xenograft (PDX) melanomas or xenografts from established human melanoma cell lines showed that intermittent dosing can delay drug resistance and tumor growth compared to continuous

dosing [75, 86, 88, 114, 114]. Clinical reports and a phase 2 clinical trial have shown dozens of cases where melanoma patients develop resistance and progress when treated with BRAF or MEK1/2 inhibitors, but then show further response when retreated after a drug holiday period [75, 92–96]. By contrast, a phase 2 trial of intermittent dosing with dabrafenib and trametinib showed worse progression free survival and no difference in overall survival compared to continuous treatment [90]. The reasons for variability in patient responses and trial outcomes is unknown, and may reflect an incomplete understanding of mechanisms underlying the response to intermittent treatment.

The current model explaining the beneficial response to intermittent treatment postulates the importance of drug addiction. Here, the viability of resistant cells decreases upon drug removal, due to the hyperactivation of MAPK signaling which promotes apoptosis or cell cycle arrest [86–88, 97, 114–116]. Intermittent scheduling is thought to alternate between selection pressure against drug-sensitive cells during periods of drug treatment, and selection against drug-resistant cells during periods of drug withdrawal. However, there is limited evidence that patient or xenograft tumors significantly regress when drug is withdrawn, as predicted by the drug addiction model. Instead, xenograft tumors usually increase in volume with drug withdrawal and decrease volume after drug rechallenge [86, 117, 118]. This raises the possibility that other mechanisms besides drug addiction may contribute to improved outcomes seen with intermittent treatment.

Here we use an in vitro strategy to examine cell autonomous responses of metastatic melanoma cells to intermittent treatment with the BRAF inhibitor, LGX818/encorafenib. We report that an intermittent schedule with LGX818 substantially lowers cell viability compared to continuous treatment, in a manner that correlates with the degree of MAPK pathway activation. Both drug addiction following prolonged LGX818 treatment, and drug resensitization following withdrawal can be observed over the multicycle time course. However, cell loss is greatest during periods of drug rechallenge, indicating that resensitization is the dominant mechanism underlying the efficacy of the intermittent schedule. Transcriptome profiling through cycles of drug treatment and withdrawal reveal that resensitization is a reversible process that involves adaptive switching between states of drug resistance and drug sensitivity. Importantly, the transcriptome of the resensitized

state can be distinguished from that of the initial, drug-sensitive state of naïve cells, and occurs against a background of sustained elevation of MAPK signaling and known resistance mechanisms. Genes controlling adaptive switching between cell states may be useful targets to delay the onset of resistance in melanoma.

2.2 Results

2.2.1 $BRAF^{V600E}$ amplification confers resistance to $BRAF^{V600E}$ and MEK1/2 inhibitors

In order to generate cells with amplified BRAF/MAPK signaling, $BRAF^{V600E}$ was overexpressed in a human metastatic melanoma cell line (WM239A) under the control of a cumate-inducible promoter (Fig. 2.1A). The oncogene was engineered as a fusion with green fluorescent protein (GFP), used to confirm expression across the stable cell population after optimizing induction time and cumate concentration (Fig. 2.1B-D). A self-cleaving T2A sequence ensured complete separation of GFP from $BRAF^{V600E}$ following expression (Fig. 2.1E).

Induction of $BRAF^{V600E}$ increased the levels of active, phosphorylated ERK1/2 (ppERK), as measured by anti-ppERK immunoreactivity and gel mobility retardation (Fig. 2.2A,B). Elevated MAPK signaling was confirmed by phosphorylation of the ERK substrate, RPS6KA (ppRSK, Fig. 2.2B). Both ERK and RSK phosphorylation were completely blocked by 500 nM LGX818 (Fig. 2.2C). Partial $BRAF^{V600E}$ expression and pathway activation was apparent even in the absence of cumate (Fig. 2.2A, 2.1B,D).

Dose response experiments were used to measure the effect of $BRAF^{V600E}$ overexpression on drug tolerance. Cells with amplified $BRAF^{V600E}$ increased IC_{50} by 50-fold over control cells harboring empty vector (Fig. 2.2D). Similar increases in IC_{50} were seen in dose response measurements with MEK162/binimetinib (Fig. 2.5B). Thus, $BRAF^{V600E}$ overexpression strongly increased cells' tolerance towards $BRAF^{V600E}$ and MEK inhibitors.

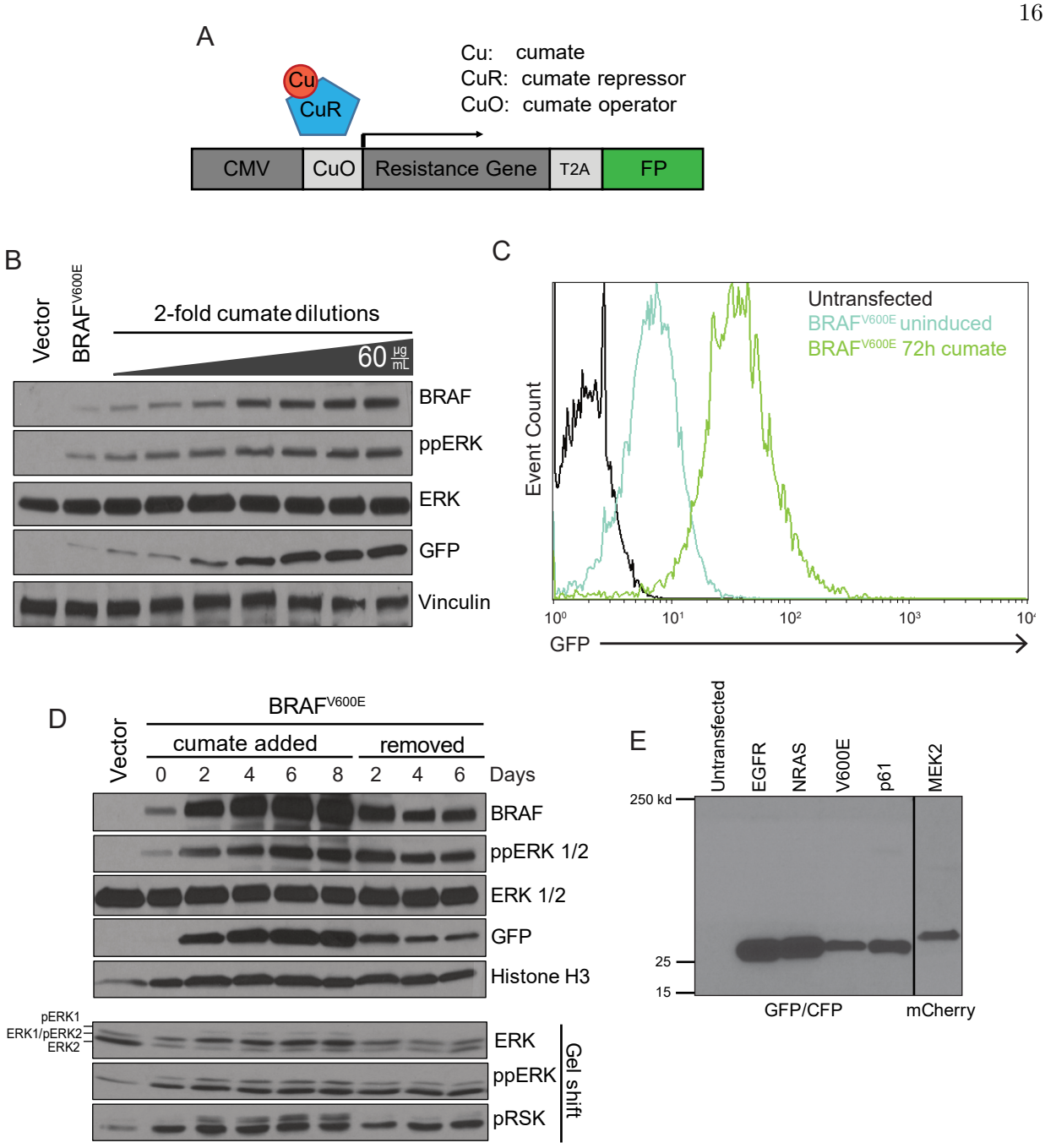

Figure 2.1: Design of inducible oncogene expression vectors and characterization of expression. **A.** Oncogenes were expressed from stably integrated cumate-inducible PiggyBac vectors as fusion proteins with fluorescent proteins (FP) separated by a self-cleaving T2A sequence. **B.** WM239A cells stably transfected with vectors for expression of BRAFV600E were induced for 72 h with serial 2-fold dilutions of cumate, starting with a maximal concentration of 60 μg /mL. **C.** Flow cytometry analysis of GFP as a reporter for BRAF^{V600E} expression, before or after cumate for 72 h. **D.** Cells with the BRAF^{V600E} vector were induced with 30 μg/mL cumate for up to 8 days, after which cumate was removed and cells were cultured in absence of cumate for up to 6 days. Cells were collected on the indicated days with or without cumate. **E.** Immunoblot showing a single band corresponding to the cleaved FP in each cell line, confirming complete cleavage of the fusion protein after induction.

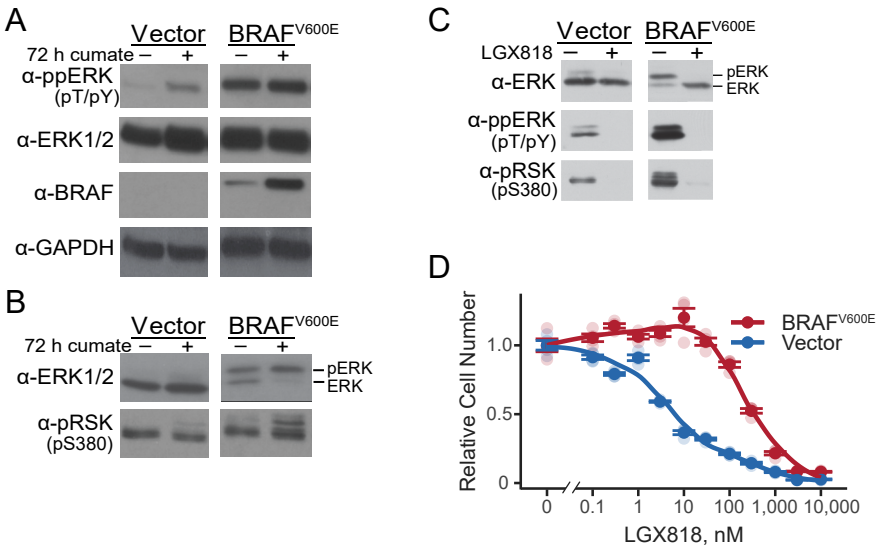

Figure 2.2: Characterization of melanoma cells with $BRAF^{V600E}$ amplification. **A.** WM239A metastatic melanoma cells stably overexpressing BRAFV600E or empty vector were either untreated or induced with cumate for 72 h, monitoring phosphorylated ERK1/2, total ERK1/2, BRAF and GAPDH by Western blotting. **B.** Western blots of cell lysates separated by low bisacrylamide SDS-PAGE to resolve different phosphoforms of ERK1/2 and phosphorylated p90RSK. **C.** WM239A cells overexpressing BRAFV600E or empty vector were cumate-induced for 72 h and then treated with 500 nM LGX818 or DMSO carrier for 2 h. Lysates were separated by low-bis SDS-PAGE. Full blots are available in Figure ref. **D.** WM239A-BRAFV600E cells were induced with cumate for 72 h, reseeded into 96 wells, and treated for 72 h with varying concentrations of LGX818. Cell numbers were measured using the CellTiter-Glo 2.0 assay, plotting mean ± s.e.m. (n=4) in dark symbols and individual measurements in light symbols.

2.2.2 Comparison of intermittent and continuous treatment

In order to compare intermittent vs continuous treatment schedules, cells were seeded in 96 well dishes and cultured for four weeks, monitoring cell viability at the end of each week (Fig. 2.3A). Intermittent timecourses followed a schedule of 7 days on drug followed by 7 days off drug. Thus, cells were treated with 500 nM LGX818 during weeks 1 and 3 and drug was removed in weeks 2 and 4. In parallel, cells were treated continuously with 500 nM LGX818 over the entire four-week period.

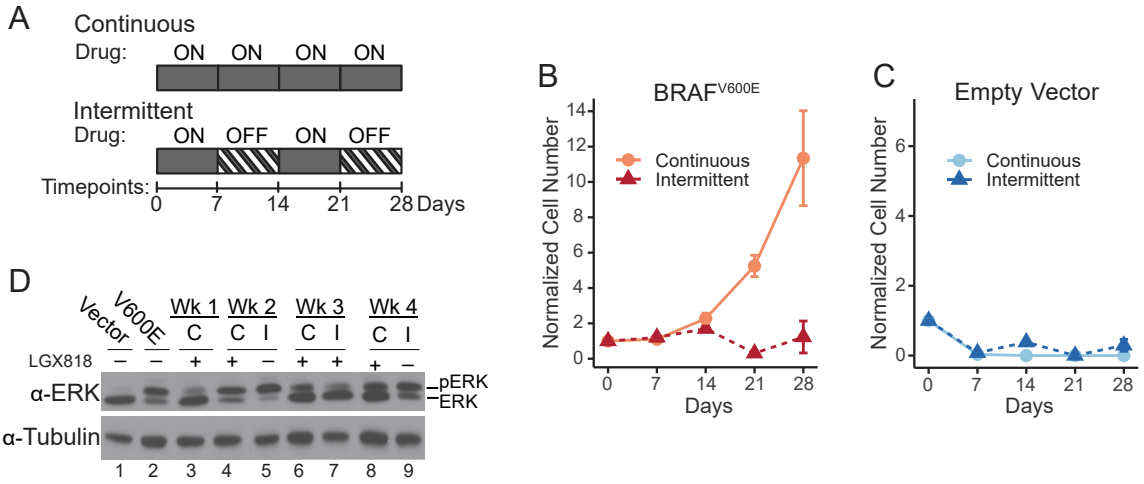

Figure 2.3: Intermittent treatment inhibits cell expansion compared to continuous treatment. **A.** Cells were cumate-induced for 72 h, reseeded in 96 wells, and cultured for 28 days under continuous or intermittent treatment conditions with 500 nM LGX818. The intermittently treated cells followed a schedule with 7 days on LGX818 and 7 days off, changing media on days 3, 5, and 7 of each week. At the end of each week, cell numbers were quantified using CellTiter-Glo assays and normalized to the initial number of cells seeded. Cell numbers (mean ± s.e.m) measured at each time point for **B.** WM239A-BRAFV600E cells (n = 5 or 6) and **C.** WM239A empty vector cells (n = 6) are shown for continuous and intermittent treatments. **D.** Western blots of lysates separated by low-bis SDS-PAGE show ERK phosphorylation in cells expressing empty vector (lane 1); BRAFV600E (lane 2); and $BRAF^{V600E}$ cells treated continuously "C" or intermittently "I" across the 4 weeks with 500 nM LGX818.

Cells treated continuously grew slowly for the first two weeks after which a drug tolerant population emerged (Fig. 2.3B). By contrast, cells treated intermittently yielded cell numbers that were initially similar to the continuous experiment for the first two weeks, but then declined after

drug rechallenge in week 3 (Fig. 2.3B). Thus, intermittent treatment inhibited the cell expansion seen with continuous treatment. Control cells expressing empty vector were strongly suppressed with either treatment schedule (Fig. 2.3C).

In order to compare responses to $BRAF^{V600E}$ against other oncogenes associated with resistance in melanoma, cells were engineered to individually express $MEK2^{C125S}$, $EGFR^{L858R}$, $NRAS^{Q61K}$ or the p61-$BRAF^{V600E}$ splice variant [59,103,104]. Like $BRAF^{V600E}$, cells expressing p61-$BRAF^{V600E}$ or $MEK2^{C125S}$ substantially increased the phosphorylation of ERK and RSK as well as IC_{50} with LGX818 or MEK162 (Figs. 2.4, 2.5). Cells expressing p61-$BRAF^{V600E}$ displayed the greatest resistance to LGX818, with 10-fold higher IC_{50} than that of $BRAF^{V600E}$ or $MEK2^{C125S}$. By contrast, $EGFR^{L858R}$ or $NRAS^{Q61K}$ only modestly increased ERK or RSK phosphorylation and IC_{50} (Figs. 2.4, 2.5). ERK and RSK phosphorylation were suppressed in all cells by 500 nM LGX818, MEK162 or the inhibitor combination (Fig. 2.6).

During continuous treatment with LGX818, cells expressing $MEK2^{C125S}$ or p61-$BRAF^{V600E}$ remained static for the first week, after which a resistant population emerged (Fig. 2.7A,B). Like $BRAF^{V600E}$, cells expressing $MEK2^{C125S}$ declined with intermittent treatment and remained inhibited for the duration of the time course (Fig. 2.7A). Intermittent treatment with LGX818 or MEK162 only partially inhibited growth of cells expressing p61-$BRAF^{V600E}$ compared to continuous treatment (Fig. 2.7B,C). However, cells were substantially reduced by intermittent treatment with a combination of LGX818 + MEK162 (Fig. 2.7D), indicating that strong inhibition of the MAPK pathway during periods of drug addition is important for maximal efficacy. Cells expressing $EGFR^{L858R}$ or $NRAS^{Q61K}$ were strongly repressed by either intermittent and continuous treatment, both which effectively inhibited expansion over the 4 week time course (Fig. 2.7E,F). Thus, intermittent treatment showed greater efficacy compared to continuous treatment, but only in cells with the highest levels of ERK activation and the strongest resistance to inhibitor.

Studies invoking the drug addiction model for intermittent dosing have reported pronounced elevation of ppERK with $BRAF^{V600E}$ amplification [86]. Therefore, we characterized the corresponding responses to continuous or intermittent treatment in our $BRAF^{V600E}$ cell system. West-

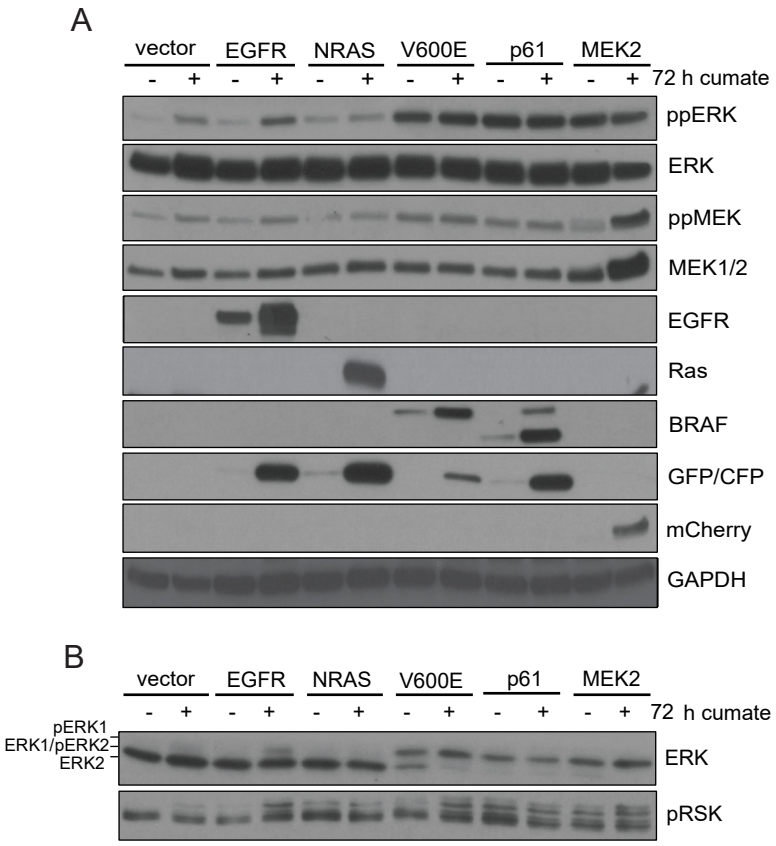

Figure 2.4: Effects of oncogene expression on ppERK signaling. **A.** WM239A cells with integrated constructs of different oncogenes were untreated or cumate-induced for 72 h prior to harvesting lysates for Western blotting of the indicated proteins. **B.** The same lysates were separated by low-bisacrylamide SDS-PAGE to resolve different phosphoforms of ERK1/2 and phosphorylated p90RSK (pS380).

ern blots showed that ppERK increased with $BRAF^{V600E}$ induction and decreased after the first week of continuous treatment (Fig. 2.3D, lanes 2,3). Subsequently, ppERK was elevated compared to continuous treatment after weeks 2 and 4 of drug removal (Fig. 2.3D lanes 5 and 9), decreasing when drug was added back during week 3 (Fig 2.3D, lane 7). Thus, while continuous treatment with LGX818 maintained lower levels of ERK activation, intermittent treatment elevated ERK during periods of drug removal to a degree equal to or greater than seen with the initial induction of $BRAF^{V600E}$ (Fig 2.3D, lanes 2,5,9).

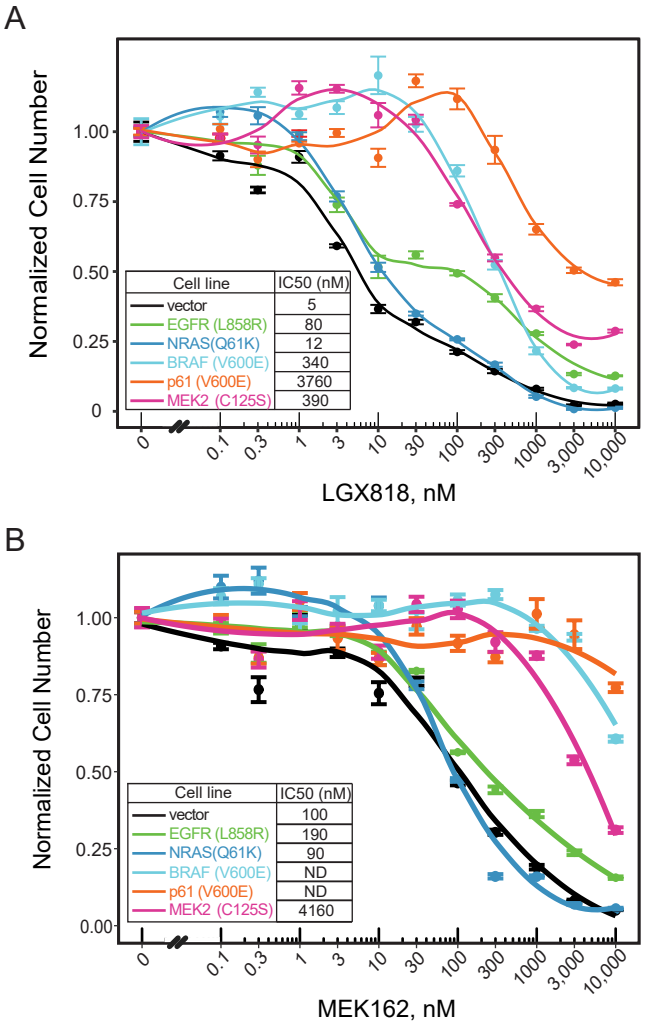

Figure 2.5: Effects of oncogene expression on drug tolerance. **A.** WM239A cells were cumate-induced for 72 h, then seeded in 96 wells and treated with varying amounts of LGX818 (n = 4). **B.** Cells were induced as in **A** but treated with MEK162 for 72 h (n = 4).

2.2.3 Intermittent treatment reverses drug addiction and resensitizes cells to LGX818

To better understand the effect of the intermittent treatment schedule on drug sensitivity and drug addiction, we characterized the LGX818 dose response of $BRAF^{V600E}$ cells collected at the end of each week of a continuous or intermittent time course. In this experiment, cells were cumate-induced to express $BRAF^{V600E}$ showed greater drug tolerance (IC_{50} = 130 nM) than cells

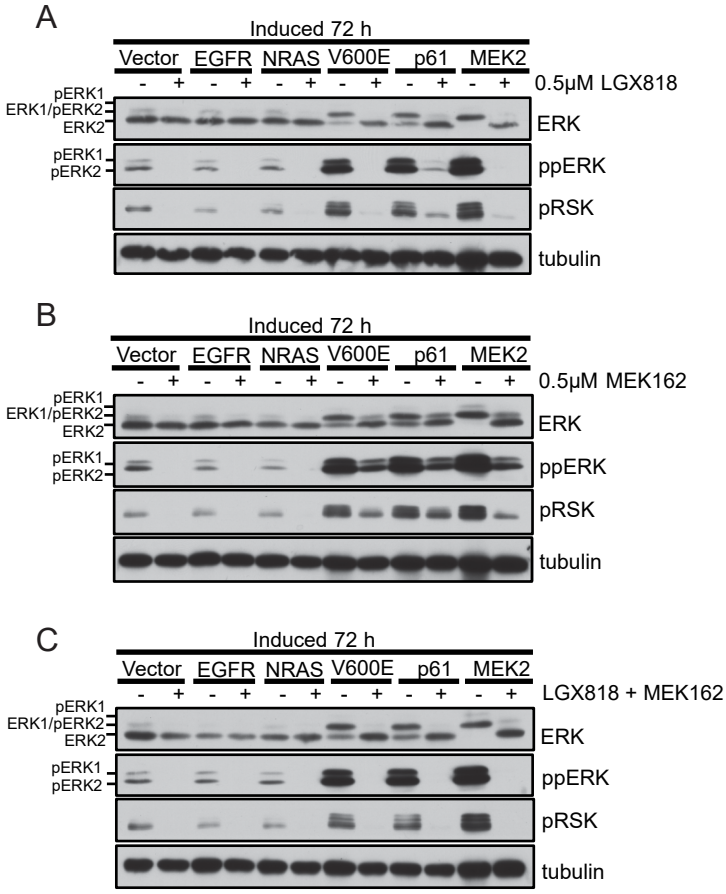

Figure 2.6: Supression of ppERK signaling by drugs in oncogene expressing WM239A cells. WM239A cells were cumate-induced for 72 h and then treated for 2 h with **A.** 500 nM LGX818, **B.** 500 nM MEK162, or **C.** 500 nM LGX818 + 500 nM MEK162. Lysates were separated by low-bisacrylamide SDS-PAGE to monitor phosphorylation of ERK (pTpY) and p90RSK(pS380).

with empty vector (IC_{50} = 5 nM) (Fig. 2.8A). After continuous treatment with 500 nM LGX818 for 7 days, the IC_{50} increased to 860 nM, and remained sustained at 1000-1200 nM over successive weeks (Fig. 2.8A). Continuous treatment also resulted in drug addiction, as evidenced by a 30-45% reduction in cell numbers at 0 nM LGX818 relative to their maximum levels at 100 nM (Fig. 2.8A). Thus, drug addiction accompanied tolerance to LGX818 in our experimental system, consistent with previous models of resistance to MAPK pathway inhibitors [86, 88, 115–117].

By contrast, cells treated intermittently varied in their dose response to LGX818, depending on whether they were collected after periods of drug addition or drug removal. Removing LGX818

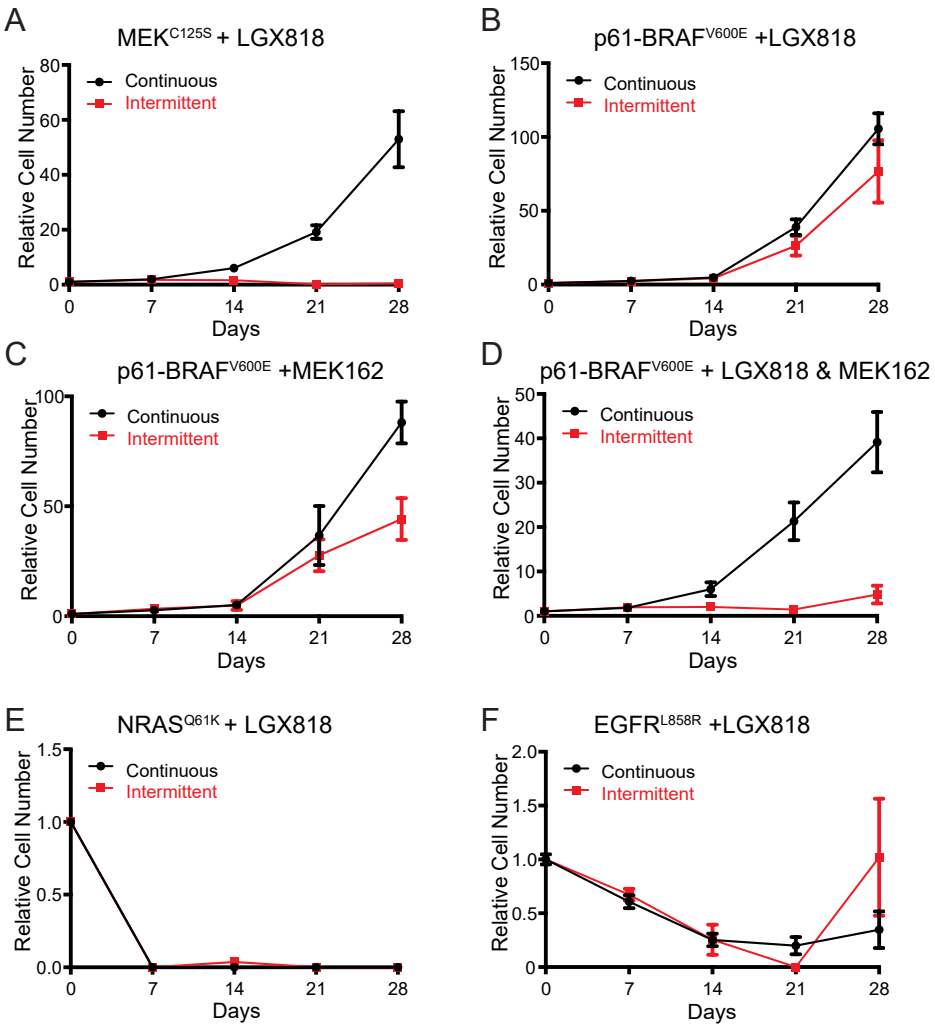

Figure 2.7: Growth curves of WM239A cells engineered to express different inducible oncogenes. WM239A cells were cumate-induced for 72 h, seeded in 96 wells, and cultured for 4 weeks under continuous or intermittent treatment conditions. The intermittent treatment cycle was 7 days on drug and 7 days off drug. Cells individually expressed **A.** MEK2^{C125S}, (B-D) BRAF-p61^{V600E}, (E) NRAS^{Q61K}, or (F) EGFR^{L858R}. The inhibitors used were **A, B, E, F** 500 nM LGX818, **C** 500 nM MEK162, or **D** 500 nM LGX818 + 500 nM MEK162.

in week 2 reduced the IC_{50} to 300 nM, a 3-fold decrease from cells treated with drug in week 1 (Fig. 2.8B). At the same time, removing LGX818 a decreased the extent of drug addiction, as shown by the recovery of cell viability at 0 nM LGX818 (Fig. 2.8B). Rechallenge with LGX818 in week 3 reversed this behavior, increasing both IC_{50} and drug addiction back to the levels seen with continuous treatment. Removing LGX818 in week 4 decreased the IC_{50} and decreased drug

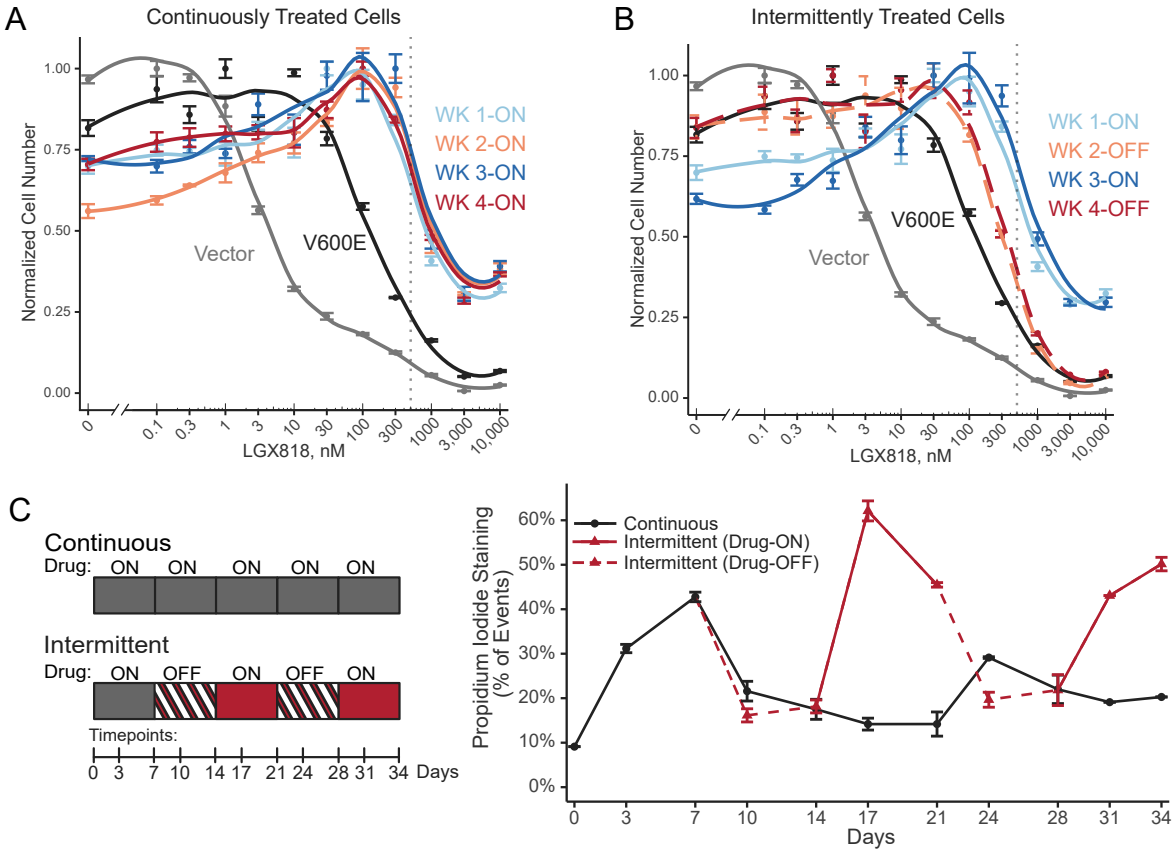

Figure 2.8: Intermittent treatment resensitizes cells to LGX818. WM239A-BRAF^{V600E} cells were cumate-induced for 72 h and seeded in 10 cm dishes followed by **A.** continuous or **B.** intermittent treatments with 500 nM LGX818. At the end of each week, cells were trypsinized, reseeded into 96 wells, and treated for 72 h with varying concentrations of LGX818 (n = 4). Cells with empty vector or BRAFV600E were also assayed for their dose response to LGX818. Both panels A and B display the same data for empty vector, BRAFV600E, and week 1-continuous, for ease of comparison. The gray dotted vertical line indicates 500 nM LGX818. **C.** Cell death across continuous and intermittent schedules was measured on days 3 and 7 of each week for five weeks. Adherent and nonadherent cells were collected together, stained with propidium iodide (PI), and analyzed by flow cytometry. The media was changed on days 3, 5, and 7 of each week. During the media change on day 5, nonadherent cells were collected by centrifugation of the conditioned media and returned to the dish for flow cytometry analysis on day 7. Measurements report average percentage of PI-positive cells (n=2 independent experiments), and error bars represent the range.

addiction back to levels comparable with week 2. Thus, each cycle of drug removal switched cells to a state with resensitization to BRAF inhibitor and each cycle of drug addition increased the extent of drug addiction.

2.2.4 Cell loss during intermittent treatment primarily involves resensitization after drug removal

Conceivably, either drug addiction or drug resensitization could account for the loss of cell viability observed with intermittent treatment. In order to explore the contribution from each mechanism, we quantified cell death at different times during periods of drug addition or removal. On one hand, if drug addiction were the dominant mechanism, cell loss should be highest during drug-off weeks when ERK hyperactivation would be predicted to promote cell death. On the other hand, if drug resensitization were more important, cell loss should be highest during drug-on weeks when cells would be susceptible to rechallenge with LGX818.

To examine this, cells were seeded in 10 cm dishes and treated with continuous or intermittent schedules over 5 weeks. Samples were taken on days 3 and 7 of each week, collecting all adherent and floating cells for analysis of cell viability by propidium iodide (PI) staining using and flow cytometry (Fig. 2.8C). Continuous treatment led to substantial cell loss during week 1, which fell to lower levels over successive weeks (Fig. 2.8C) with the expansion of cells able to persist or grow in the presence of LGX818 (Fig. 2.3B). Parallel flow cytometry measurements showed $BRAF^{V600E}$ expression increaseding over the first two weeks of continuous treatment, then maintained over successive weeks (Fig. 2.9).

In cells treated intermittently, the percentages of PI-positive cells during drug-off periods (days 10, 14 and 24, 28) were comparable to those in cells treated continuously (days 10-28). However, cell death dramatically increased during periods of drug rechallenge (days 17, 21 and 31, 34) where the percentage of PI-positive cells reached levels as high as 60% (Fig. 2.8C). These results indicate that the reduction in cell fitness with intermittent treatment is best explained by the occurrence of resensitization during periods of drug withdrawal, followed by cell loss when cells are rechallenged with LGX818. This was consistent with the measurements of cell numbers during intermittent treatment, which decreased only when drug was readded in week 3 (Fig. 2.3B).

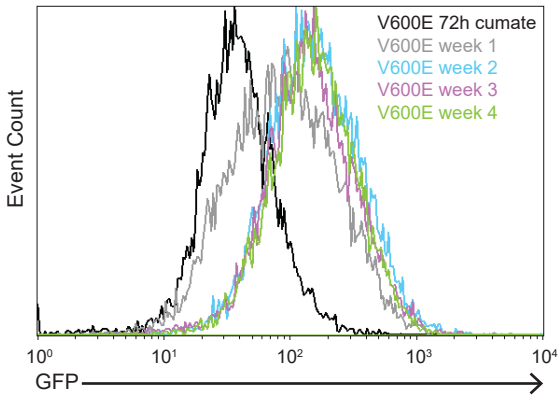

Figure 2.9: Continuous treatment with LGX818 enriches cells with elevated $BRAF^{V600E}$ expression. Cells were treated with 30 μg /mL cumate for 72 h to induce expression of BRAFV600E, then cultured with 500 nM LGX818 for 4 weeks. Cells were collected at the end of each week and analyzed by flow cytometry using GFP as a reporter for BRAFV600E expression.

2.2.5 Transcriptomic responses to continuous and intermittent treatment

In order to explore gene expression changes that accompany drug resensitization, RNA-seq was used to examine cells expressing $BRAF^{V600E}$ after each week of intermittent or continuous treatment with LGX818 (Fig. 2.10A). Cell viability measurements conducted in parallel matched those observed previously, where resistant cells emerged after 2 weeks of continuous treatment with LGX818 and intermittent treatment delayed outgrowth (Fig. 2.11). Datasets were also collected on cells with empty vector, $BRAF^{V600E}$ induced for 72 h, and $BRAF^{V600E}$ induced for 72 h then treated with 500 nM LGX818 for 20 h. These were performed as controls to measure gene expression responses to acute activation or inhibition of the MAPK pathway without long-term selection. Each condition was analyzed in triplicate, except for duplicates of the week 4-continuous condition.

Principal component analysis showed that nearly 70% of the variance across the samples could be accounted for by the first two principal components. Plotting PC1 against PC2 distributedseparated each the samples into one of three easily identifiable groups (Fig. 2.10B). One group included cells with empty vector, 72 h induced $BRAF^{V600E}$, and 72 h $BRAF^{V600E}$ + 20 h LGX818 (Fig. 2.10B, Group 1). A second group contained all cells that were continuously treated (weeks

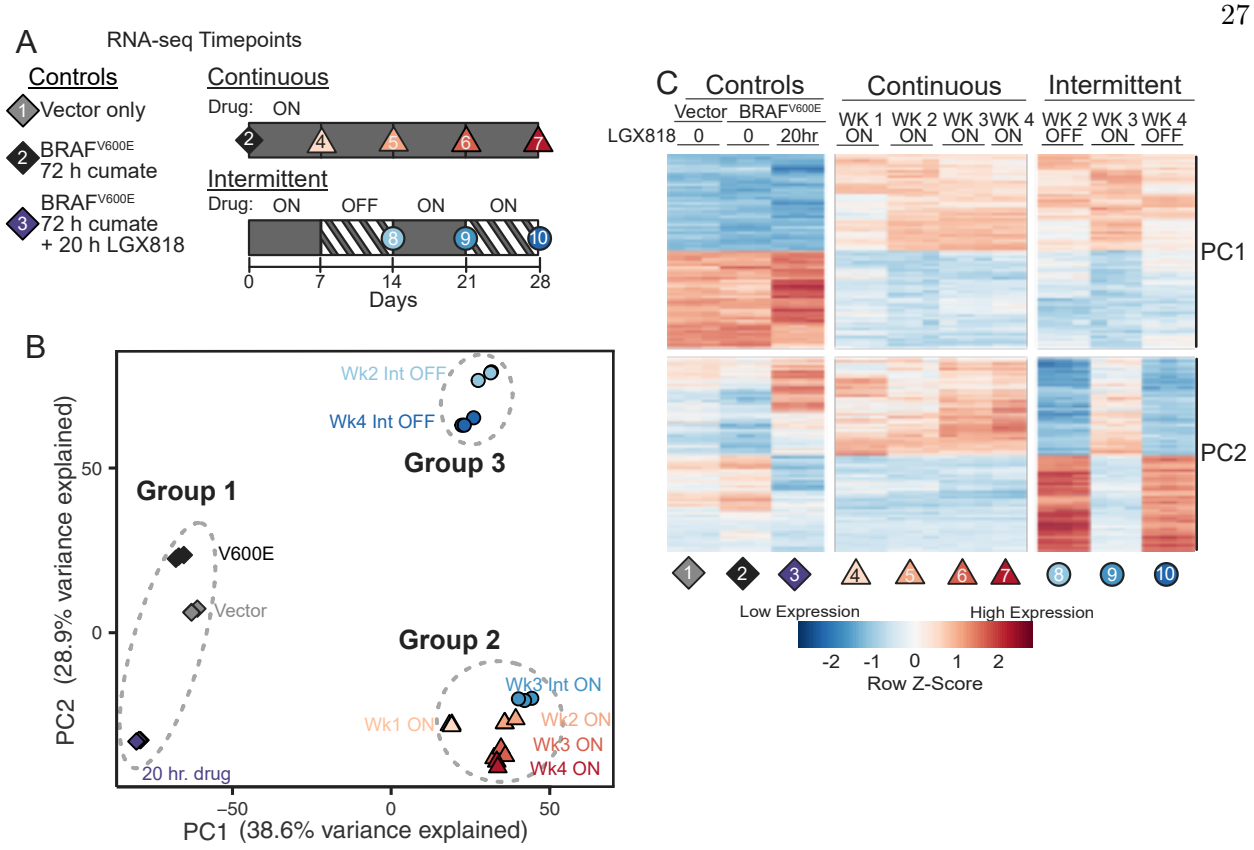

Figure 2.10: Transcriptomic profiling of continuous and intermittently treated cells. **A.** Schematic of RNA samples collected from WM239A-BRAF^{V600E} cells comparing continuous and intermittent drug treatment with 500 nM LGX818. Each condition was collected in biological triplicates, except for week 4-continous (sample 7) which was collected in duplicates, for a total of 29 samples. **B.** Principal component analysis (PCA) of the 6000 highest variance genes. PC1 and PC2 account for almost 70% of the variance of in these genes. The 10 different experimental conditions visibly cluster into 3 separate groups. **C.** Heatmap of the 400 genes most positively or negatively associated with PC1 or with PC2. Each row is mean centered and scaled to unit variance.

1-4), as well as cells from intermittent week 3, when drug was reintroduced (Fig. 2.10B, Group 2). The third group included cells treated intermittently in weeks 2 and 4, when drug was removed (Fig. 2.10B, Group 3). Thus, thise analysis revealed a striking effect of intermittent treatment, in which cells with drug removed in weeks 2 and 4 were grouped together and were well separated from cells with drug readded in week 3.

Significantly, the separation between Groups 1 and 2 mainly occurred along the PC1 axis, suggesting transcriptomic changes resulting from long-term treatment with LGX818. The separa-

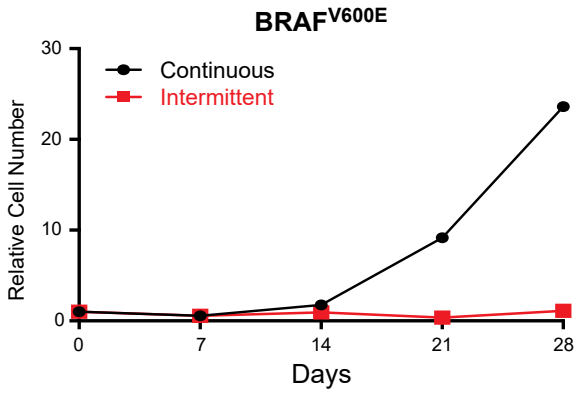

Figure 2.11: Growth curves of WM239A-BRAF^{V600E} cells during the RNA-seq experiment. Cells were plated in 10 cm dishes in parallel with cells harvested for RNA-seq, quantifying cell numbers for continuous and intermittent RNA-seq experiments using the Cell Titer-Glo assay (n=1).

tion between cells collected in successive weeks of intermittent treatment occurred primarily along the PC2 axis, corresponding to reversible movement between Groups 2 and 3 (Fig. 2.10B). This suggested that PC2 largely reflects reversible transcriptomic changes accompanying drug removal and drug readdition. A heatmap of the genes highly contributing to either principal component showed that most PC1 gene expression changes after week 1 were sustained in subsequent weeks with either continuous or intermittent treatment (Fig. 2.10C). In contrast, PC2 transcripts reversibly switched in expression between the drug-on and drug-off periods during the intermittent time course (Fig. 2.10C). Analysis of the complete gene expression datasets showed strong correlations between cells with drug readded during week 3 and those continuously treated throughout weeks 1-4 (Fig. 2.12). This confirmed that rechallenging cells with LGX818 recapitulates the transcriptomic state of continuously treated cells. Thus, reversible changes in the transcriptome accompany the ability of cells to switch between drug-resistant and -resensitized states during the intermittent time course.

2.2.6 Transcriptome changes associated with drug tolerance

We asked if the transcripts altered in response to continuous LGX818 treatment might reflect genes that function in cancer drug tolerance, using gene set enrichment analysis [119, 120].

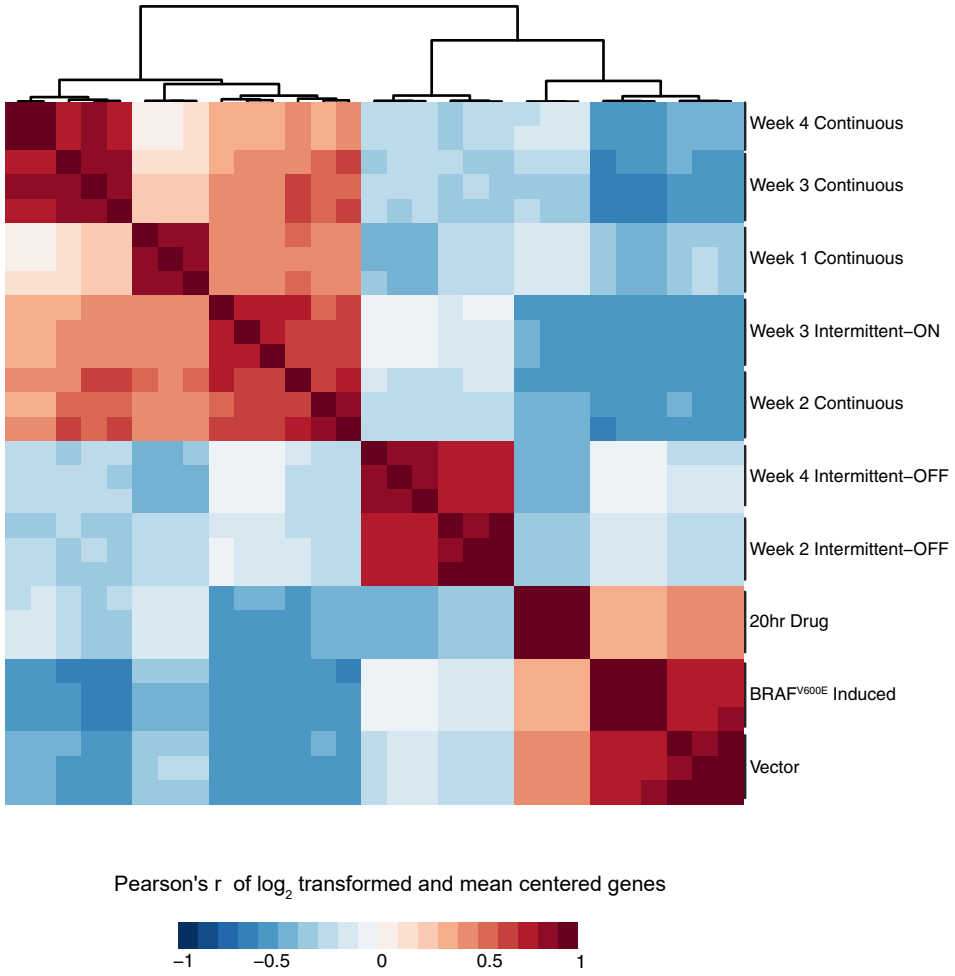

Figure 2.12: Correlation matrix of RNA-seq datasets. The normalized counts for each sample were log2 transformed and mean-centered per gene. Pearson's correlation coefficient r was calculated for all pairwise comparisons of samples. The matrix was clustered using hierarchical clustering.

The PC1 genes that increased expression with prolonged treatment were enriched in molecular signatures associated with resistance to $BRAF^{V600E}$ and MEK inhibitors, including markers of the epithelial-mesenchymal transition (EMT), NFkB signaling, inflammatory markers, and hypoxia, while genes that decreased expression were enriched in gene sets associated with a proliferative, melanocytic phenotype (Fig. 2.13A). These signatures are characteristic of the invasive, dedifferentiated melanoma phenotype associated with melanoma malignancy [73,74,76,77]. The PC2 genes that reversibly decreased upon drug removal were negatively associated with gene signatures

characteristic of the invasive phenotype, suggesting partial reversal of invasion/EMT processes.

We next assessed how the expression levels of genes responsive to continuous LGX818 treatment correlated with drug tolerance across human melanoma cell lines. RNA-seq data from 34 $BRAF^{V600}$ mutant melanoma cell lines available from the cancer cell line encyclopedia (CCLE) [121] were used to perform hierarchical clustering based on the expression levels of transcripts highly associated with PC1. These cell lines formed two main clusters, denoted A and B in Fig. 2.13B. The gene expression patterns of cell lines in Cluster A resembled transcript levels in our drug-naïve cells (Group 1 in Fig. 2.10B), while cell lines in Cluster B showed greater similarly to our cell system after long term treatment with LGX818 (Groups 2 & 3, Fig 2.10B). The degree of tolerance among CCLE cell lines, measured by IC_{50} for the BRAF inhibitor, PLX4720, correlated well with cluster membership, largely separating drug-sensitive cells in Cluster A from drug-resistant cells in Cluster B. The analysis reveals that the transcript changes associated with LGX818 resistance in WM239A cells can explain the variance in baseline drug tolerance across many other $BRAF^{V600}$ mutant cell lines. Therefore, the transcriptome responses to continuous treatment in our experimental model are consistent with the those associated with drug tolerance across melanoma systems.

It was noteworthy that the transcriptomes of cells in Group 3, characterized by drug removal, were distinct from those of cells with empty vector or induced $BRAF^{V600E}$ in Group 1 (Fig. 2.10B, C). This implies that the resensitized cell state generated by LGX818 removal differs from the initial sensitive state of drug-naïve cells. Prominent among the PC2 transcripts that switched reversibly following drug removal and subsequent rechallenge were those that were weakly or in some cases non-responsive to $BRAF^{V600E}$ induction in drug-naïve cells (Fig. 2.10C). This implies that many PC2 genes normally respond weakly to MAPK signaling, but acquire greater responsiveness to this pathway after a week of continuous exposure to drug. Thus, the resensitized cell state includes new transcriptional responses that only occur after MAPK signaling is activated by drug removal.

We also compared transcript changes corresponding to known resistance genes in melanoma. To do this, we curated a list of 71 genes that were reported to control tolerance towards $BRAF^{V600E}$ and/or MEK inhibitors in melanoma cell lines and tumors (genes and references in Table S4). These

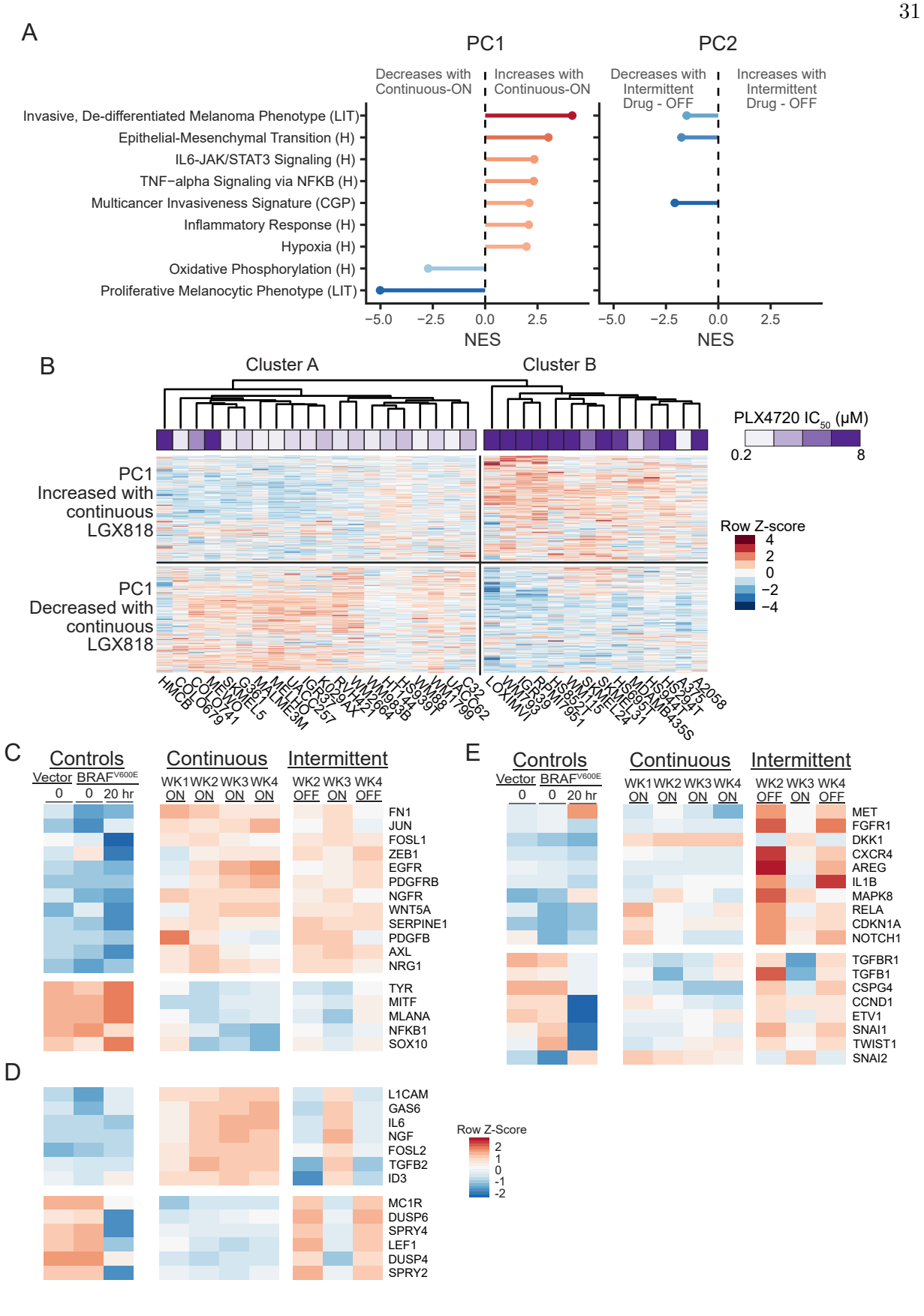

Figure 2.13: Reversible transcriptome changes are associated with EMT. Continued on next page.

Figure 2.13: **A.** Gene set enrichment analysis (GSEA) was performed on genes associated with PC1 and PC2. The gene loadings for each PC were used as the ranks. Shown are the normalized enrichment scores (NES) for selected gene sets matched to PC1 with significant FDR adjusted p-values (q< 0.002). The NES for the same gene sets matched to PC2 are shown for cases where the FDR adjusted p-value is less than q < 0.05. Gene sets were from Molecular Signature Database for Hallmark "H", Chemical and Genetic Perturbations "CGP", or derived from the literature "LIT". **B.** Clustered heatmap of RNA-seq data of BRAFV600 mutant melanomas in the cancer cell line encyclopedia (CCLE). Only the 800 genes identified as PC1 associated in Fig. 4 are shown and used to cluster the cell lines. Cluster A mostly contained cell lines that were sensitive to BRAF inhibitor (lower IC50), PLX4720, while Cluster B mostly contained cell lines with greater drug tolerance (higher IC50). The two clusters show differential expression of genes that either increased or decreased with continuous treatment in our RNA-seq dataset. textbfC.-E. Heatmaps of RNA-seq data corresponding to literature-curated genes that have been implicated in melanoma drug resistance or sensitivity. **C** Known resistance genes that changed in response to continuous treatment and did not change with drug removal, predicting sustained resistance over the intermittent time course. **D** Resistance genes showing reversible expression between drug-on and drug-off weeks, that changed in a manner predicting resensitization upon drug removal. **E** Resistance genes showing reversible expression between drug-on and drug-off weeks, but predicting higher resistance during weeks of drug removal in the intermittent time course.

included signaling effectors, transcription factors, and mediators and markers of EMT, neural crest specification, and melanocyte differentiation. Forty-eight of the curated genes were significantly altered with continuous drug treatment, consistent with the emergence of resistant cell populations. For example, growth factor receptors and ligands, EMT and neural crest markers known to promote resistance (e.g. PDGFRB, EGFR, AXL, NGFR, WNT5A) [64, 71, 72, 108, 116] increased with continuous drug treatment, while genes associated with differentiation to the melanocyte lineage (e.g. MITF, TYR, MLANA, SOX10) [74, 108] decreased (Fig. 2.13C).

Among the curated genes associated with drug resistance in melanoma, some transcripts changed reversibly with LGX818 removal in a manner consistent with resensitization (Fig. 2.13D). For example, growth factors NGF and GAS6 decreased during drug-off weeks, which might predict lower signaling through their respective receptors, NGFR and AXL. Likewise, the transcription factor ID3, which promotes resistance to BRAF inhibitor [122], decreased after drug removal, while LEF1, which associated with greater sensitivity [82, 112, 116], increased. Negative feedback regulators of growth factor signaling, DUSP4/6 and SPRY2/4, reversibly increased after drug

removal, consistent with MAPK pathway reactivation [67, 123].

However, the majority of resistance genes from our curated list were inconsistent with resensitization, and in fact predicted sustained resistance with intermittent scheduling. These included growth factor receptors/ligands (AXL, NGFR, EGFR, PDGFRB, PDGFB, WNT5A) and transcription factors (JUN, FOSL1/FRA1, ZEB1) which remained elevated following drug removal, and differentiation markers (MLANA/MART1, TYR, MITF, SOX10) which remained repressed (Fig. 2.13C). Paradoxically, other responsive transcripts predicted increased resistance upon drug removal. For example, FGFR1, MET, AREG, TGFB1, IL1B and CSPG4 were all upregulated during drug-off weeks (Fig. 2.13E), which would be expected to increase receptor signaling and diminish sensitivity to BRAF inhibitors [116, 124–128]. Also included in this group were the transcription factors TWIST1, SNAI1 and RELA, which promote EMT via epigenetic repression of histone marks [129, 130], but increased when drug was removed (Fig. 2.13C, E), and SNAI2, which promotes the dedifferentiated, non-invasive phenotype [129] but increased with drug removal.

Taken together, our gene expression analyses revealed distinct molecular responses to the continuous and intermittent treatment regimens. Many transcripts altered by prolonged drug treatment corresponded to genes implicated in drug resistance in melanoma and were regulated in a manner consistent with the drug tolerant state observed with continuous treatment. Other transcripts switched expression between states of resistance and sensitivity, but only a subset of known resistance genes reversed in a manner consistent with resensitization upon drug removal.

2.2.7 Adaptive responses to intermittent treatment

As noted above, many transcript changes that were significant after the first 7 days of LGX818 exposure were sustained when drug was removed in weeks 2 and 4 (Fig. 2.13B). Their irreversibility may be due to slow rates of reversal, or to an initial selection for drug-tolerant cell subpopulations. On the other hand, nearly all genes that changed reversibly during the course of intermittent treatment were found to recover the transcriptome of continuously treated cells during week 3, when drug was readded. This implies an adaptive mechanism, responsive to epigenetic regulation.

However, bulk RNA-seq cannot distinguish between mechanisms involving adaptive transitions in cells switching from drug-resistant to drug-sensitive states, and mechanisms for selection pressure for sensitive cell subpopulations within a resistant majority.

To investigate these possibilities, we examined the dynamics of expression of the neural cell adhesion protein, L1CAM. Bulk transcript levels of L1CAM were elevated in cells treated for prolonged periods with LGX818, consistent with its role in promoting EMT and as a marker for melanoma drug resistance [106, 131, 132]. Its expression decreased following drug removal in a manner that was reversible in subsequent weeks of drug rechallenge and withdrawal (Fig. 2.13D). The changes in L1CAM protein expression at the single cell level were measured by flow cytometry at several timepoints during continuous and intermittent treatment using a fluorescently labeled primary antibody (Fig. 2.14A). We selected these timepoints in order to capture the cell population dynamics corresponding to reversal of expression during early stages of drug withdrawal. In drug naïve cells (Day 0), many cells expressed low levels of L1CAM, some overlapping with the nonspecific isotype control (Fig. 2.14B). After treating cells with LGX818 for 7 days, the median expression level increased by more than 10-fold over that of drug-naïve cells and remained high for 14 days of continuous drug treatment. In the intermittent schedule, L1CAM expression during the first three days of drug withdrawal gradually decreased in a unimodal fashion (Fig. 2.14B). The cells transiently expressed intermediate levels of L1CAM, which then decreased further to match the drug-naïve population by the end of the week. The unimodal populations with intermediate L1CAM were inconsistent with selection pressure against a subpopulation of drug-addicted cells, which would have predicted bimodal cell populations shifting from high to low L1CAM. Therefore, the transcript responses following drug withdrawal largely follows an adaptive mechanism for transcript switching, instead of selective depletion of drug-addicted cells.

2.3 Discussion

Our study demonstrates that adaptive mechanisms for cell switching from drug-tolerant to drug-resensitized states can explain the growth suppressive effects of treating melanoma cells inter-

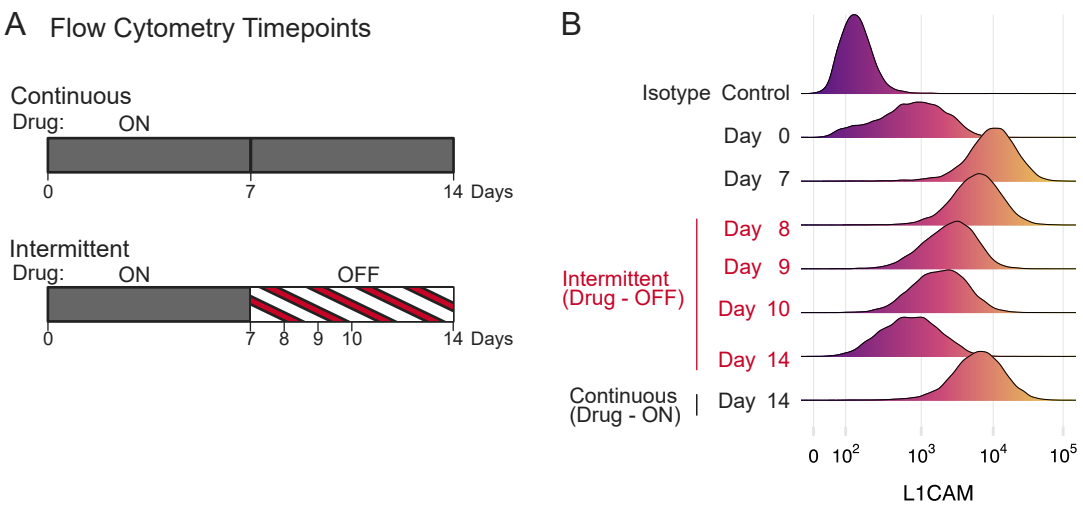

Figure 2.14: Cell resensitization is accompanied by adaptive gene expression changes in single cells, not by counterselection. **A.** WM239A-BRAF^{V600E} cells were cumate-induced for 72 h, seeded in 10 cm dishes, and cultured under continuous or intermittent treatment with 500 nM LGX818. At the indicated time points, cells were fixed and stained with a fluorescently labeled primary antibody for L1CAM and then analyzed by flow cytometry. **B.** Smoothed histograms of single cell L1CAM expression by flow cytometry at the different timepoints. Controls using a fluorescently labeled non-specific isotype control antibody confirmed specificity of binding to the target protein.

mittently with LGX818. The BRAF^{V600E} amplified cell model used in our study showed transcripts responsive to drug that corresponded well with resistance genes known to function across melanoma cell lines and tumors. Importantly, when drug tolerance was induced by prolonged treatment, the cells displayed both a drug addiction response after treatment and a drug resensitization response after drug withdrawal. Cell death was highest during periods of rechallenge, showing that cell viability was affected most by the resensitization to kinase inhibitor. Transcriptome analyses showed many gene expression changes that were readily reversible over the intermittent time course, nearly all which returned to levels seen in continuously treated cells when drug was reintroduced. This indicated that the responses to intermittent treatment were not due to selection pressure, as supported by the expression dynamics of L1CAM in single cell populations.

Previous studies have shown that drug addiction is caused by resistance mechanisms that maintain MAPK pathway signaling at submaximal levels in the presence of BRAF inhibitor, and hyperactivate MAPK signaling when drug is removed, thereby triggering apoptosis or cell ar-

rest [86–88, 115, 116]. Thus, it has been theorized that the intermittent treatment effect arises by alternating selection against drug-sensitive cells in the presence of BRAF inhibitor and counterselection against drug-addicted cells in the absence of inhibitor [97]. In our system, MAPK signaling was maximally activated following LGX818 withdrawal, based on increased phospho-ERK1/2 and the expression of downstream pathway targets such as DUSP and SPRY. But while drug addiction was evident, it clearly played a secondary role in the response to intermittent treatment. In cells treated continuously, cell viability was highest at 100 nM LGX818 and at 500 nM fell to levels less than or equal to that in the absence of drug (Fig. 2.8A). This explains why drug addiction did not contribute significantly to growth suppression with intermittent treatment in our experiments, because it would have had the largest effect at drug concentrations lower than we used. In patients, plasma concentrations of BRAF inhibitors approach or exceed micromolar levels [133, 134]. Therefore, drug addiction might also play a minor role in these settings, consistent with the observation that patient tumors do not regress upon drug removal.

Our findings are consistent with a role for phenotypic plasticity in drug tolerance, which has been well documented in $BRAF^{V600E}$ melanomas as well as other cancers [74, 76, 77]. Current models postulate elevated expression of resistance genes in rare cell populations, which in response to BRAF inhibitor, enhance resistance by promoting epigenetic pathways for dedifferentiation and transcriptional reprogramming [73, 82, 106–112]. Classes of transcripts that promote resistance include drivers of EMT and invasion (AXL^{high}, $WNT5A^{high}$, $TGFB^{hig}$h, $TWIST^{high}$, $SNAI1^{high}$) as well as markers of lineage development from differentiated melanocytes to neural crest stem cells ($NGFR^{high}$, $MITF^{low}$, $SOX10^{low}$) [73, 107–112]. Exploiting the reversibility of these adaptive regulatory events during early, non-mutational phases of drug tolerance has been proposed as a treatment strategy for cancer. Our findings concur and further show that adaptive mechanisms can underlie the beneficial response to an intermittent schedule.

Significantly, transcriptome profiling of our system revealed many resistance genes that changed with continuous drug treatment but were irreversible during the intermittent time course. These reflect adaptive responses to drug and/or the selection of cell populations able to persist

and survive during the first week of LGX818 treatment. This set included most genes characteristic of the invasive, neural crest phenotype and EMT. This means that resensitization after drug removal occurred in spite ofdespite a large number of resistance genes that did not reverse. Altogether, only a few genes implicated in resistance both displayed reversibility and changed in a direction consistent with resensitization. Leading candidates included LEF1, which is repressed in drug resistance melanoma and strongly associated with phenotype switching to the proliferative, non-invasive state [81, 82, 112], and ID3, which is elevated in resistant cells and whose depletion in resistant cells confers resensitization [122]. They did not include genes reported to regulate drug addiction in melanomas, such as JUNB, FOSL1, or CDKN1A [87, 115], consistent with a minimal influence of drug addiction on the intermittent treatment effect.

Interestingly, many transcripts that responded reversibly with each cycle of drug removal were elevated to levels well above those seen in drug-naïve cells. In fact, many reversible transcripts showed little or no response to short term induction of $BRAF^{V600E}$. This suggests that genes that were not normally downstream of MAPK signaling became pathway targets after 7 days of drug treatment. Conceivably, drug treatment may have enriched a subpopulation of cells with an expanded range of transcriptional responses. Alternatively, new targets may have been triggered by the hyperactivated MAPK signaling that followed drug withdrawal. Further definition of the cellular mechanisms involved in reversible resensitization may lead to novel targets and the potential contribution of MAPK signaling thresholds to the resensitized cell state.

The partial reversal of resistance gene expression upon drug removal helped explain the partial resensitization response of only a 3-fold decrease in IC_{50} . Therefore, the drug tolerant state in our hands appears to represent an intermediate to late stage in transcriptome reprogramming, with a few rapidly reversible and many slowly reversible resistance genes [108]. Conceivably, a longer period of drug withdrawal might have eventually returned cells to the initial transcriptome and sensitivity level of drug-naïve cells, as observed in other studies of transcriptome dynamics [111]. However, in order for intermittent treatment to block cell expansion, the amount of time needed for resensitization must be balanced against the faster cell doubling time during the period of drug

removal. Therefore, partial resensitization may be a practical condition needed for a successful intermittent treatment schedule.

So far, intermittent treatment of melanoma has been unproven, with clinical outcomes arguing for and against its potential effectiveness. On one hand, a recent phase II trial revealed worse progression-free survival in melanoma patients treated intermittently with dabrafenib + trametinib compared to those treated with continuous therapy (PFS 5.5 months on a 5-week on, 3-week off schedule vs 9.0 months continuous) [90]. On the other hand, retrospective and prospective studies of dozens of patients who progress on BRAF or MEK inhibitor have reported that more than one-third show a second clinical response after a drug holiday period [91–96]. Preclinical studies using xenografts have been mixed as well. While some have reported delayed emergence or complete suppression of resistant tumors using intermittent scheduling [75, 86, 88, 114] others have observed more rapid outgrowth of tumors [117, 118]. A notable report showed a substantial benefit of intermittent treatment in xenografts from a drug-resistant melanoma cell line, but only when the dosing schedule was tailored individually for each mouse [75]. Optimal scheduling was established using a predator-prey model for adaptive drug therapy which postulates expansion and loss of sensitive cells during drug-off and drug-on periods, respectively [135, 136]. Early stage clinical trials are ongoing to test these intriguing concepts for melanoma, breast and prostate cancer, and the possibility that personalized scheduling may be optimized by dynamic measurements of cancer blood markers [136–138].

In summary, our findings show that intermittent treatment can suppress cell growth and delay the emergence of drug resistance by transitioning from a drug-resistant state to a more sensitive state through adaptive transcriptional mechanisms. Significantly, this can occur against a background of many resistance genes that either fail to reverse when drug is removed or change in a manner that would paradoxically predict increased resistance. Thus, we propose that intermittent treatment generates a distinct cellular state that accompanies resensitization, which may include transcripts not normally regulated by MAPK signaling and are triggered by higher signaling thresholds. Genes controlling resensitization may be useful targets to augment or improve the response

duration of current treatment strategies for melanoma.

2.4 Materials and Methods

2.4.1 Cell Culture

The human metastatic melanoma cell line, WM239A, was a kind gift of Dr. Meenhard Herlyn, Wistar Institute and cells were expanded and stored in liquid nitrogen at passage 8. These cells harbor a heterozygous BRAFV600D mutation, confirmed by RNA-seq analysis. Cells were grown in RPMI1640 media supplemented with 10% fetal bovine serum (Gemini,# 100-500) and 1% penicillin/streptomycin (Gibco, # 15140163) and were maintained at 37°C and 5% CO2. Stable cell lines were made from WM239A cells at passage 20 and all experiments were performed within 5 passages of thawing cells. Inhibitors of BRAFV600E (LGX818/encorafenib, # S7108) and MKK1/2 (MEK162/binimetinib, # S7007) were from Selleck Chemicals. Long term cell cultures were seeded in 96-well plates at 500 cells per well or in 10 cm dishes at 86,000 cells per dish and growth media with or without drug were refreshed every Monday, Wednesday and Friday. Cell viability was measured using the CellTiter-Glo 2.0 Assay (Promega, # G9242) according to the manufacturer's protocol and calibrated against a standard curve of cells seeded at 2-fold dilutions between 125-64,000 cells per well. For dose response measurements, cells were seeded in 96-well plates at 2,500 cells per well and cell viability data were collected 72 h afterwards.

2.4.2 Plasmids and Cell Lines

Plasmids for expression of each resistance oncogene were constructed by Boulder Genetics. Briefly, open reading frames for human $BRAF^{V600E}$, p61-$BRAF^{V600E}$, $MEK2^{C125S}$, $EGFR^{L858R}$, and $NRAS^{Q61K}$ were inserted into an inducible PiggyBac vector (Systems Biosciences, # PBQM800 A-1). Plasmids and PiggyBac transposase (Systems Biosciences, # PB210PA-1) were electroporated into WM239A cells using the Neon transfection system (Invitrogen, # MPK10096) with 2 pulses x 20 ms pulse width at 1200 V. Stably transfected cells were selected for by addition of 1μg

/ ml puromycin to growth media for 7 days. Resistance genes were induced with 30 μg /ml cumate (Systems Biosciences, # QM150A-1) for 72 h, followed by treatment with LGX818 or MEK162.

2.4.3 Immunoblotting/Gel Shift Assays

Cells were lysed in RIPA buffer [10 mM Tris pH 8.0, 140 mM NaCl, 1% (v/v) Triton X100, 0.1% (w/v) SDS, 1 mM EDTA, 0.25% (w/v) sodium deoxycholate, 1 mM NaF, 1X EDTA-free protease inhibitors (Roche, # 11873580001) and 1X PhosStop phosphatase inhibitors (Roche, # 4906845001)] and sonicated at low power using a needle homogenizer. Protein concentrations were determined using the DC protein assay (Bio-Rad, # 5000111). Protein samples (10 μg/lane) were separated on Tris-glycine gels or 4-20% protean-TGX precast gradient gels (Bio-Rad, # 4561094) and proteins were transferred to PVDF-SQ membranes (Millipore, # ISEQ00010) for 1 h at 100 V. Membranes were incubated in primary antibody for 2 h at room temperature or overnight at 4 °C and in secondary antibody for 1 h at room temperature. Low-bis SDS-PAGE gels (10% acrylamide/0.13% bis-acrylamide) were used to separate unphosphorylated and phosphorylated forms of ERK1/2 (28). Antibodies for immunoblotting were from Cell Signaling Technology unless otherwise noted: ERK2 (# 4696), phospho-p44/p42 ERK1/2-pThr202/pTyr204 (# 4370), MKK1/2 (# 9122), phospho-MKK1/2-pSer217/pSer221 (# 9121), EGFR (# 4267), pan-Ras (Millipore, # OP40), BRAF (Santa Cruz Biotechnology, # sc-166), GFP (Santa Cruz Biotechnology, # sc-9996), mCherry (GeneTex, # GTX59788), GAPDH (# 5174), phospho-RSK (# 9335), and beta-tubulin (# 2146).

2.4.4 Propidium Iodide Assay for Cell Death

Cells were collected for flow cytometry by trypsinization and resuspension in PBS. In order to assess cell viability, cells grown in 10 cm plates were trypsinized from the plate and collected together with cells floating in media by centrifugation. Cells were then resuspended in PBS + 2 μg /ml propidium iodide (Sigma-Aldrich, # P4170), incubated for 20 min, and analyzed on a FACSCelesta flow cytometer (BD Biosciences). Flow cytometry was also used to quantify oncogene expression

by monitoring GFP, CFP or mCherry. For long term experiments, GFP calibration beads (Takara Bio, # 632594) were used to confirm consistency of the GFP signal over successive weeks. Flow cytometry data analysis was performed using Flowing Software 2 (http://flowingsoftware.btk.fi/) and FCSalyzer (https://sourceforge.net/projects/fcsalyzer/).

2.4.5 Flow cytometry analysis of L1CAM protein expression

Cells grown in 10 cm dishes were washed with twice with PBS and harvested by incubation in 0.5 mM EDTA in PBS at room temperature. Cells were centrifuged and resuspended in 50 μL PBS. Then the cells were fixed by diluting 4% PFA in PBS to the tube for a final concentration of 2% PFA. This incubated at 37°C for 5 minutes, and the PFA was quenched by adding 2.5 M glycine in PBS for a final concentration of 125mM. The cells were spun down at 300 rcf and washed once with 125 mM glycine in PBS. The cells were resuspended in ice cold 0.5% BSA in PBS and stored at 4°C. Once all the samples were collected, 150,000 cells per sample were aliquoted into tubes, centrifuged, and resuspended in 100 uL of 0.5% BSA in PBS and 2.5 μL of either L1CAM antibody conjugated to BV421 fluorescent dye (BD Horizon cat# 565733) or isotype control (BD Horizon # 562439). Cells were mixed by gentle vortexing and incubated in the dark on an orbital shaker for 1 hour at room temperature. The cells were washed twice and then resuspended in 0.5% BSA in PBS and analyzed on a FACSCelesta flow cytometer (BD Biosceinces). Data analysis was performed using custom scripts in R (v.4.0.3).

2.4.6 Gene Expression Profiling

Cells were rinsed with PBS, trypsinized, and centrifuged for 5 min at 300xg, then washed with 1 mL PBS and centrifuged again. After aspirating away PBS, cells were immediately frozen in liquid nitrogen and stored at -80^{o}C. At the end of the timecourse, all samples were thawed on ice and total RNA was purified using the Quick-RNA microprep kit (Zymo Research, # R1050) according to the manufacturer's protocol. RNA-seq was conducted by the Functional Genomics Shared Resource at the University of Colorado Cancer Center, Aurora CO. RNA quality was assessed using a 4200

TapeStation System (Agilent Technologies) and 100 ng RNA was used to prepare mRNA libraries using the Universal Plus mRNA-seq kit (NuGEN). Sequencing was performed on a HiSeq4000 System (Illumina) with 150 bp reads and 30 million reads per sample.

Adapter sequences and low quality base reads were removed using Trimmomatic (v.0.32, LEADING:3 TRAILING:3 SLIDINGWINDOW:4:15 MINLEN:36) (1). Reads were then mapped to the Homo sapiens genome (GRCh38) using the alignment software, HISAT2 (v.2.0.3-beta, –dta –rna-strandness F) (2). The resulting SAM file was converted to a sorted BAM file using SAMtools (v.0.1.18) (3). Reads that mapped to genes in the GRCh38.84.gtf annotation file were counted using the htseq-count script in HTSeq (v.0.6.1, -f bam -r pos -s yes -t exon -m union -i gene_id) (4). All downstream analyses were performed using R (v.4.0.3) and R Studio (v. 1.3.1093). Data were pre-filtered for genes that had at least 60 reads. The DESeq2 package (v.1.30.1) was used to normalize samples by library size and estimate dispersion factors (5). For visualizations and statistical learning methods, counts were log2 transformed using the vst (variance stabilizing transform log2) function in DESeq2. Principal component analysis was performed using the prcomp function on the vst transformed data that was mean centered and set to unit variance for the 6000 genes with the highest variance across the 29 samples. The top 400 genes with the most negative or positive loadings per principal component were assigned to that PC for visualization in a heatmap.

2.4.7 Analysis of melanoma cell lines in cancer cell line encyclopedia (CCLE)

RNA-seq unnormalized count data (version 18Q1) and drug sensitivity data (NP24.3009) were downloaded from the cancer cell line encyclopedia (CCLE) website. There were 34 BRAFV600 mutant melanoma cell lines with both RNA-seq data and IC50 data for PLX4720. The RNA-seq data for these cell lines was normalized to library size using DESeq2, and log2 transformed using the vst function, and each gene was mean centered and scaled to unit variance. This dataset was filtered for the 800 genes corresponding to PC1 in our dataset (Table S3), and the cell lines were clustered by hierarchical clustering.

2.5 Code and Data Availability

The RNA-seq data from this study can be accessed on NCBI GEO using the accession number GSE117123. The code used in this study is available at `https://github.com/andykavran/Intermittent_Drug_Treatment`.

Chapter 3

Denoising large-scale biological data using network filters

3.1 Background

System-wide molecular profiling data are often contaminated by noise, which can obscure biological signals of interest. Such noise can arise from both endogenous biological factors and exogenous technical factors. These factors include reagent and protocol variability, researcher technique, passage number effects, stochastic gene expression, and cell cycle asynchronicity. This variability can mask underlying biological signals when measuring cell state and how it changes under different conditions, e.g., in development [139, 140], cancer progression [141], and adaptive drug resistance [82,142]. Noise has also been implicated in the appearance of false signals and in the non-replicability of some studies [143, 144]. Identifying and correcting noisy measurements before analysis is likely to improve the detection of subtle biological signals and enable more accurate predictions in systems biology.

If correlations between related molecular signals are stronger than correlations among sources of noise, then distinct but related signals can be combined to denoise biological measurements, at the expense of a smaller effective sample size. There are three common approaches to identifying related signals: gene sets, subspace embedding, and networks. In the first category, methods like GSEA [120, 145] use the enrichment of genes within curated sets to project the data onto biologically relevant features. While gene sets can increase the power to identify differentially regulated processes, they are inherently coarse, and can themselves be noisy, incomplete, or biased, and thus may not generalize to novel processes. Subspace embedding techniques include PCA [146], cluster-

ing [147], and neural network autoencoders [148, 149]. These methods can capture novel gene-gene correlations, but they rarely incorporate biological information into the feature extraction, which can limit both interpretability and generalizability.

Molecular profiling data alone does not directly inform which measurements should be more or less related to each other. Networks that represent a molecular system's functional structure can provide this missing information. For example, protein-protein interaction, metabolic reaction, and gene regulation networks each encode precise and biologically meaningful information about which groups of measured protein expression levels, metabolite concentrations, or transcript levels are functionally related, and hence which measurements should be combined to filter out independent noise. Current network approaches use computationally intensive methods to identify which entities are most related, which can limit their utility for large networks and general usability [150, 151]

Among neighboring elements in the network, the underlying signals may be correlated (assortative) or anti-correlated (disassortative) [152]. For example, differential expression tends to correlate between neighboring genes in a regulatory network [153]. In contrast, inhibitory or compensatory interactions [154, 155] will tend to produce a disassortative relationship. Beyond pairs of measurements, networks can also exhibit large-scale mixing patterns among these interactions, such that a network may be more or less assortative in some regions and disassortative in others [156]. Existing network-based methods typically do not exploit this variability, and instead assume globally assortative mixing by applying a single filter to the whole network [150, 151, 157]. Mismatching the filter and the relationship type, e.g., an assortative filter with anti-correlated measurements, can further obscure the underlying biological signals. Here, we describe a general network-based method that can automatically detect large-scale mixing patterns and account for both assortative and disassortative relationships.

These network filters are closely related to kernel-based methods in image processing [158], in which groups of related pixels are transformed together to improve their underlying visual signal. Most such techniques leverage an image's underlying grid geometry to choose which pixels have related signals for denoising. Networks lack this geometry because a node's interactions are

inherently unordered, whereas the left- and right-hand neighbors of a pixel are clearly defined. This connection between network filters and image processing is rich with potentially useful ideas that could be adapted to process large-scale biological data. For instance, community detection in networks is a clear analog of the common "segmentation" step in image analysis, in which pixels are first partitioned into groups that represent the large-scale structure of an image, e.g., to separate foreground and background, or a car from the street, and then different filters are applied to each segment (module).

We first describe two classes of network filters, which combine measurement values from neighboring nodes to calculate an assortative or disassortative denoised value, and we describe a general algorithm that decomposes the network into structural modules and then automatically applies the most appropriate filter to the nodes and connections within each module. When applied to synthetic data where the true values and network structure are known, these filters substantially reduce errors relative to a baseline. In addition, we show how applying the wrong filter with respect to the underlying biological relationship can lead to increased errors. Finally, to test the practical utility of these methods in a more realistic setting, we investigate the impact of network filtering on a machine learning task in which we predict changes in human protein expression data when a healthy tissue becomes cancerous. Using the network filters to denoise the expression data before model training increases the subsequent prediction accuracy up to 43% compared to training on unfiltered data.

3.2 Methods

3.2.1 Synthetic data with known noise and structure

In the first experiment we generate simple non-modular random graphs using the Chung-Lu (CL) model [159–161] with $n = 100$ nodes and a degree distribution that, in expectation, follows a power law distribution $\Pr(k) \propto k^{-\alpha}$ with parameter $\alpha = 3$ for $k \geq 1$. If the generated degree sequence included a node with degree $k > 17$, a new degree sequence was sampled. This

choice ensured that no star-like subgraphs were created. In our analysis, only nodes in the largest connected component were included. This choice mitigates the bias experienced by low degree nodes, which are the most likely nodes to exist outside the largest component.

For each CL synthetic network, we generate node values using the procedure described below. We vary the assortativity coefficient $r \in [-0.8, 0.8]$ while drawing values from a Normal distribution with mean and variance $\mu = \sigma^2 = 100$. We simulate measurement noise by taking a random permutation of a uniformly random 25% of the node values. We then apply each of the networks filters (mean, median, sharp) to these noisy values, and calculate the mean absolute error (MAE) of the original and denoised values. We also apply netSmooth and Laplacian exponential kernel methods varying smoothing parameter values to this data, and calculate the MAE of original and denoised values. Results are averaged over 5000 repetition of this process.

To create noisy non-modular networks, we performed a random rewiring procedure previously described [162]. After generating a non-modular random graph using the CL model and generating metadata, we select a given proportion of edges to remove from the graph. Then, we placed the same number of new edges between any two nodes chosen uniformly at random, while ensuring that there were no multi-edges in the graph. Then the filters were applied to the noisy network as normal.

In the second experiment, we generate simple modular random graphs using the degree-corrected stochastic block model (DC-SBM) [163], with $\kappa = 5$ communities of $n_r = 100$ nodes each ($n = 500$ nodes total), and the same degree distribution as the non-modular case. The network's modular structure is specified using the standard "planted partition" model [163], in which the community mixing matrix ω_{rs} is given by a linear combination of a perfectly modular graph and a random graph, and has the form $\omega_{rs} = \lambda\omega_{rs}^{\text{planted}} + (1-\lambda)\omega_{rs}^{\text{random}}$, with $\lambda = 0.85$.

For each DC-SBM network, we generate node values with the following properties: (i) the distribution of values within each module are drawn from a module-specific Normal distribution with mean $\mu = \{110, 80, 60, 40, 20\}$ and variance $\sigma^2 = 25$, (ii) $\kappa' \in [0, 5]$ communities are assigned to have negative assorativity coefficients, and (iii) the within-community assortativity coefficients

are chosen uniformly at random on the interval $|r| \in [0.4, 0.7]$. These choices construct a hard test in which a filter's accuracy is effectively penalized if it uses nodes outside a given community to denoise a particular value. For the patchwork filter, we partition the network using three different classes of community detection algorithms. The "metadata-aware" DC-SBM [164] and spectral algorithm [165] partitioned the graph in $\hat{\kappa} = 5$ communities. Modularity maximization partitioned the graph into the number of clusters that maximizes the modularity function [166]. Noise is induced and accuracy is assessed as in the non-modular case, except that the nodes are randomly permuted within each module rather than the whole network.

3.2.2 Generating synthetic correlated measurements

We generate node values with a specified assortativity coefficient r_*, for a specified adjacency matrix A, using Markov chain Monte Carlo (MCMC). The assortativity coefficient r is defined as

$$r = \frac{\sum_{ij} (A_{ij} - k_i k_j / 2m) \, x_i x_j}{\sum_{ij} (k_i \delta_{ij} - k_i k_j / 2m) \, x_i x_j}$$

where k_i is the degree of node i, x_i is the value associated with node i, $2m = \sum_{ij} A_{ij}$ is twice the number of edges in the network, A_{ij} is the entry in the adjacency matrix for nodes i and j, and δ_{ij} is the Kronecker delta function.

Given a network A, a desired assortativity coefficient r_*, and a node value distribution $\Pr(x)$, we generate a set of node values as follows.

(1) Assign each node a value drawn iid from $\Pr(x)$.

(2) Calculate the current assortativity coefficient r_0.

(3) Set $t = 1$.

(4) While the difference between the desired and current assortativity coefficient $\Delta = |r_t - r_*| > \beta$, a specified tolerance, do:

- Pick a node i uniformly at random and assign it a new value x_i' drawn iid rom $\Pr(x)$.

- Calculate the corresponding assortativity coefficient r_t and difference $\Delta' = |r_t - r_*|$.
- If the new value does not improve the assortativity, i.e., $\Delta' > \Delta$ restore x_i. Otherwise, increment t.

(5) Return the node values $\mathbf{x}$ with the desired assortativity coefficient, r_*.

In our experiments, we set $\beta = 0.009$.

3.2.3 Diffusion-based denoising methods

We benchmark the network filters against two comparison methods that weight nodes based on different diffusion kernels. The Laplacian exponential diffusion kernel [151] $\mathbf{S}_\beta$ is defined as

$$\mathbf{S}_\beta = \mathrm{e}^{-\beta \mathbf{L}}$$

where β is a real valued smoothing parameter, and $\mathbf{L}$ is the graph Laplacian. The denoised data vector is found by multiplying the matrix and noisy data vector

$$\mathbf{x}_{\mathrm{Laplacian},\beta} = \mathbf{S}_\beta \mathbf{x} \ .$$

The netSmooth method [150] uses the personalized Pagerank [167] vector to weight each node. This kernel $\mathbf{K}$ is defined as

$$\mathbf{K}_\alpha = (1-\alpha)(\mathbf{I} - \alpha \mathbf{B})^{-1}$$

where $\mathbf{B}$ is a adjacency matrix that is degree normalized by column such that $\mathbf{B}_{ij} = \frac{1}{k_j}$ if there exists and edge between i and j, α is the smoothing parameter (also known as the restart probability), and $\mathbf{I}$ is the identity matrix. The denoised data vector is found by multiplying this kernel and the noisy kernel as such

$$\mathbf{x}_{\mathrm{netSmooth},\alpha} = \mathbf{K}_\alpha \mathbf{x} \ .$$

For simplicity, we call both β and α "smoothing parameter" throughout as they have a similar function for their respective methods.

3.2.4 Human protein expression and interaction

Protein expression data were drawn from the Human Protein Atlas (HPA) version 16 [168], which details protein expression in human tissues by large scale immunohistochemistry (IHC), for over 12,000 proteins in 20 tissue types, each in a healthy and cancerous state. We represented the IHC scores of not detected, low, medium, and high as numerical values of 0, 1, 2, and 3, respectively. In cases where a protein had scores from multiple patients, the numerical values were averaged together. Human protein interaction (PPIN) data were drawn from the HINT database [169], which combines data from several interactome databases and is curated for biological interactions with high levels of evidence. The HINT network contains $n = 12{,}864$ proteins and $m = 62{,}435$ undirected, unweighted edges.

To construct the network filter, we first map the data from the HPA to the PPIN. HPA proteins are indexed by their Ensembl IDs, while HINT proteins are indexed by their Uniprot IDs. A map from Ensembl IDs to Uniprot IDs was constructed using the HGNC BioMart tool. If a node had multiple mapped expression values, we averaged them. We allow protein expression values from HPA to map to multiple nodes if the Ensembl ID maps to multiple nodes in the PPIN. If the gene expression value does not map to any nodes in the PPIN, we discard these as they cannot be de-noised by the network filters. There is one protein in the cancer dataset and 283 proteins in the healthy tissue dataset missing protein expression values in no more than 2 cancers or healthy tissues. For these cases, we impute the missing data from the same protein in another cancer or healthy tissue uniformly at random (impute healthy from healthy, and cancer from cancer).

After keeping the largest connected component of nodes with associated HPA data values, these preprocessing steps produce a network with $n = 8{,}199$ proteins with IHC expression information across all 20 tissue types and both healthy and cancerous states, and $m = 37{,}607$ edges. The included healthy-cancerous tissue pairs are: breast, glioma, cervix, colorectal, endometrial, testicular, thyroid, renal, liver, lung, lymphoma, pancreas, prostate, skin, stomach, melanocyte, urinary, head and neck, ovary, carcinoid. For the healthy tissues, the protein expression values of

specific cells types that can give rise to the corresponding cancer were averaged together to form one vector (Table 3.1).

3.2.5 Predicting expression changes in human cancer

The machine learning task is to predict the changes in protein expression levels when a human tissue changes types from healthy to cancerous. We use K-nearest neighbors regression to learn a model that can predict these changes when given the expression levels of a healthy tissue (Fig. 3.1). We train and evaluate the model using leave-one-out cross validation, in which the model is trained on the observed changes in 19 healthy-cancerous tissue pairs, and is tested on one unobserved pair. We first train and evaluate the model on unfiltered data, and then compare its accuracy to a model where we apply a network filter to the expression data prior to training.

First, we applied principal component analysis (PCA) on the training set of 19 healthy tissue protein vectors as a feature extraction method. Next, using the embedded PCA space learned from the training set, we project the held-out healthy sample into the same PCA space. We then determine the K-nearest neighbors of the held-out healthy tissue by calculating the Euclidean distance of the first four principal components between this point and all other healthy tissues.

Given this identification of which healthy tissues are most similar to the left-out healthy tissue, we predict the protein expression changes for the held-out observation. We calculate the expression changes between cancerous and healthy tissues, which we call a "delta" vector. Then, we perform PCA on the 19 delta vectors to extract features. The weighted average of the delta vectors corresponding to the K-nearest neighbors learned from the healthy tissues are averaged together, where the weight is proportional to the inverse of the Euclidean distance to the held-out healthy tissue. Finally, we project the predicted delta vector from four principal components back to the $n = 8{,}199$ proteins and calculate the mean absolute error (MAE) of this vector and the actual delta vector.

The basic networks filters evaluated in this task have the form given in the main text. For the patchwork filter, the DC-SBM or spectral algorithms partition the PPIN into $\kappa = 10$ communities,

Table 3.1: Cell types from the Human Protein Atlas dataset averaged together to form a single healthy tissue vector

Healthy Tissue	**Cell Types Averaged**
Breast	Breast Adipocytes, Breast Glandular Cells
Glia	Cerebral Cortex Glial Cells, Hippocampus Glial Cells, Caudate Glial Cells
Cervix	Cervix Uterine Glandular Cells, Cervix Uterine Squamous Epithelial Cells
Colorectal	Colon Endothelial Cells, Colon Glandular Cells, Rectum Glandular Cells
Endometrium	Endometrium Cells in Endometrial Stroma, Endometrium Glandular Cells
Testes	Epididymis Glandular Cells, Seminal Vesicle Glandular Cells, Testis Cells in Seminiferous Ducts, Testis Leydig Cells
Thyroid	Thyroid Glandular Cells
Kidney	Kidney Cells in Glomeruli, Kidney Cells in Tubules
Liver	Liver Bile Duct Cells, Liver Hepatocytes
Lung	Lung Pneumocytes
Lymph	Lymph Node Germinal Center Cells, Lymph Node Non-Germinal Center Cells
Pancreas	Pancreas Exocrine Glandular Cells, Pancreas Islets of Langerhans
Prostate	Prostate Glandular Cells
Skin	Skin Fibroblasts, Skin Keratinocytes, Skin Epidermal Cells
Melanocyte	Skin Melanocytes
Stomach	Stomach Glandular Cells
Urinary	Urinary Bladder Urothelial Cells
Head and Neck	Nasopharynx Respiratory Epithelial Cells, Oral Mucosa Squamous Epithelial Cells, Salivary Gland Glandular Cells
Ovary	Ovarian Stroma Cells
Carcinoid (Healthy)	Colon Endothelial Cells, Colon Glandular Cells, Colon Peripheral Nerve Ganglion, Duodenum Glandular Cells, Pancreas Exocrine Glandular Cells, Pancreas Islets of Langerhans, Prostate Glandular Cells

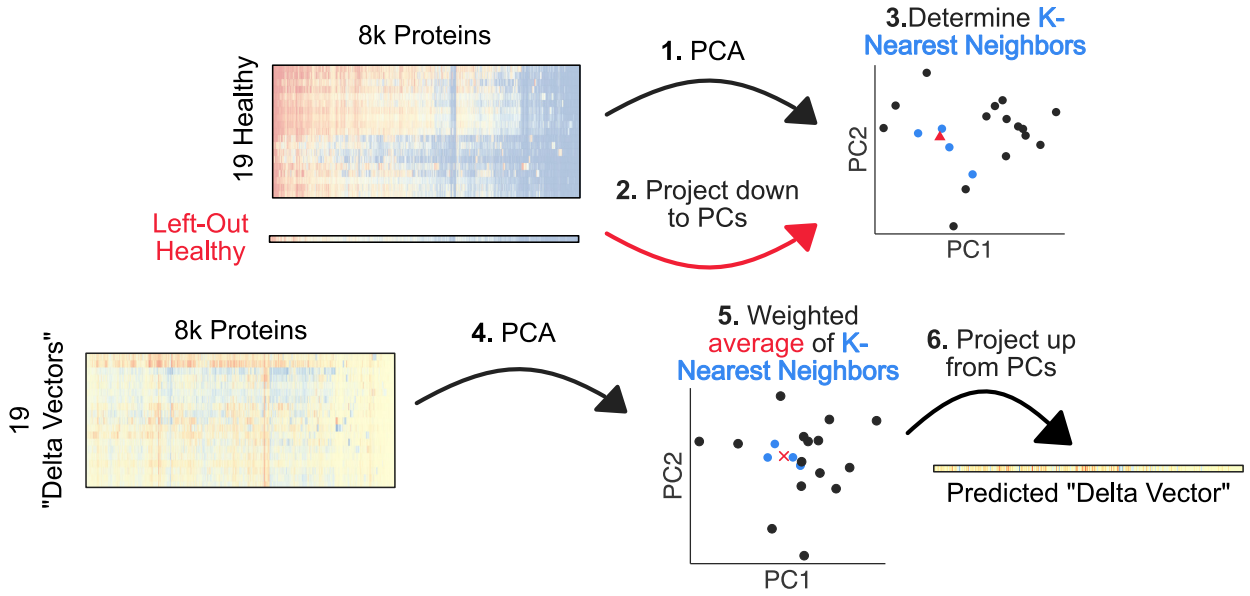

Figure 3.1: Schematic of K-nearest neighbors regression framework. We designed a weighted K-nearest neighbors regression framework to predict the protein expression changes a healthy tissue would undergo when becoming cancerous, given a vector of protein expression profile of a healthy tissue. First, we extract features from the training set of 19 healthy tissue protein expression vectors by PCA. Second, we project the left out healthy vector down to the same PCA space, and third, determine K-nearest neighbors to use for the prediction task. Fourth, we extract the features from the 19 delta vectors by PCA, and fifth, predict the delta vector for the left-out healthy sample by taking the weighted average of the K-nearest neighbor's delta vectors. Finally, sixth, we project the predicted delta vector from PCA space back to a vector of protein expression values to calculate the error.

and modularity maximization automatically chooses the number of communities that maximizes the modularity function. Then, we apply the mean filter within each community.

For the diffusion-based methods, we choose optimized smoothing parameters for the human protein expression data set using a method described by the netSmooth authors [150] to maximize the entropy of a 2D embedding of the data. As the healthy data and delta vectors have different data distributions, we choose optimized smoothing parameters for each data set separately. Briefly, the healthy tissue protein expression or delta vectors were embedded in a PCA space with the first two principal components. This space was discreteized into a four by four grid, equally spaced from the data points at the minimum and maximum of each PC. We calculated the Shannon entropy, $H(x) = -\sum_i P(x_i) \log P(x_i)$, of this discretized embedding, and chose the smallest smoothing parameter that maximized the entropy. For netSmooth, the smoothing parameter was 0.2 for the healthy tissues and 0.3 for the delta vectors. And for the Laplacian exponential diffusion kernel, it was 0.2 and 0.1 for healthy tissues and delta vectors, respectively.

3.3 Results

3.3.1 Network filters

A network filter is specified by a function $f[i, \mathbf{x}, G]$, which takes as input the index of the measurement (node) to be denoised, the list of all measurements $\mathbf{x}$, and the network structure G among those measurements. The output is the denoised value $\hat{x}_i$. Here, we consider only local network filters, which use the measurement values of i's immediate neighbors in G, denoted by the node set ν_i, which are likely to be the most biologically relevant for denoising. Each filter is applied synchronously, so that all denoised values are obtained simultaneously to prevent feedback within the denoising process.

We note that the idea of a network filter can naturally generalize to exploit information, if available, about the sign or strength of interactions in G. This information can be encoded by an edge weight w_{ij}, which can capture inhibitory or excitatory interactions that are strong or weak.

Below, we focus on the case in which this information is not available.

When a measurement x_i correlates with the values of its neighbors x_{ν_i} in the network (assortativity), a network filter should adjust x_i to be more similar to the measured values of its neighbors (Fig. 3.2A). Among the many choices of functions with this qualitative behavior, the mean and median have useful mathematical properties, and connect with past work [157]. This setting is analogous to a smoothing operation in image processing, in which a pixel's value is replaced by the mean or median of its value and its neighbors' values. In the context of a network, the mean and median "smoothing" filters have the forms:

$$f_{\bullet,1}[i, \mathbf{x}, G] = \frac{1}{1 + k_i} \left(x_i + \sum_{j \epsilon \nu_i} x_j w_{ij} \right) \quad , \tag{3.1}$$

where $w_{ij} = 1$ and k_i is the degree of node i, reflecting unweighted interactions, and

$$f_{\bullet,2}[i, \mathbf{x}, G] = \text{median}[\{x_i, \, x_{\nu_i}\}] \quad . \tag{3.2}$$

When a measurement x_i anti-correlates with the values of its neighboring nodes, a network filter should adjust x_i to be more distant from its neighbors (Fig. 3.2A). This setting is analogous to enhancing the contrast in an image, e.g., when using the technique of unsharp masking to enhance the high frequency signal in an image to make it sharper. In the context of a network, this "sharpening" filter has the form:

$$f_{\circ}[i, \mathbf{x}, G] = \alpha(x_i - f_{\bullet,1}[i, \mathbf{x}, G]) + \bar{\mathbf{x}} \tag{3.3}$$

where α is a constant scaling factor, and $\bar{\mathbf{x}} = n^{-1} \sum_i x_i$ is the global mean. Because α is a free parameter, its value should be determined de novo for each data set. For the data sets in this study, we empirically determined the optimal $\alpha = 0.8$ using cross validation.

When a system exhibits large-scale mixing patterns of assortative and disassortative relationships, a network should first be partitioned into structural modules using a community detection algorithm, so that relationships within each module are more homogeneous. Let $\vec{s} = \mathcal{A}(G)$ denote the result of applying a community detection algorithm $\mathcal{A}$ to network G, and say that G_{s_i} denotes

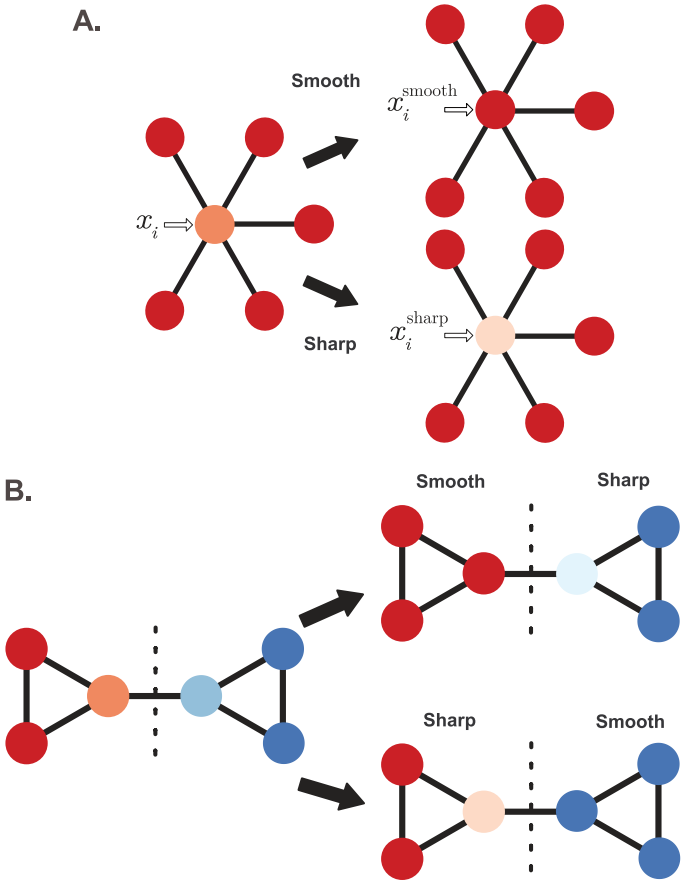

Figure 3.2: Schematics of network filters. Network filters are tools that denoise real-valued biological data using a biologically meaningful network to exploit the correlation ("smoothing")or anti-correlation ("sharpening") among neighboring measurements. **A.** A measurement x_i and its neighboring values in network, where the color intensity is proportional to the measured value. In applying the smooth filter, x_i is adjusted to be more similar to its neighbors; in applying the sharp filter, x_i is adjusted to be more distant from its neighbors. **B.** Measurements can also first be partitioned into groups (dashed line) by detecting structural modules within the network, and then different filters applied to different modules, ignoring between-module edges, e.g., if the signals are assortative in some communities and disassortative in others.

the subgraph of nodes and connections within the module s_i that contains node i. Given such a modular decomposition $\vec{s}$, a filter can then be applied to only the subgraph G_{s_i} that contains measurement i. As a result, relationships that span the boundary between two modules will have no influence on the filtered values (Fig. 3.2B).

After partitioning, the same filter can be applied to every community, or sharp and smooth filters can be applied to communities with more or less assortative values, respectively. We define such a "patchwork filter" as:

$$f[i, \mathbf{x}, G_{s_i}] = \begin{cases} f_{\circ}[i, \mathbf{x}, G_{s_i}], & \text{if } \mathrm{r_{s_i}} < 0 \\ f_{\bullet,1}[i, \mathbf{x}, G_{s_i}], & \text{if } \mathrm{r_{s_i}} \geq 0 \end{cases}, \tag{3.4}$$

where r_{s_i} is the standard assortativity coefficient calculated over observed values within community s_i [152]. While any community detection algorithm can be used for $\mathcal{A}$, here we use methods from three classes of algorithms: modularity maximization [166], spectral partitioning [165], and statistical inference. For community detection by statistical inference, we use the degree-corrected stochastic block model or DC-SBM [163] or the "metadata-aware" version of DC-SBM [164], which are considered state-of-the-art methods [170].

3.3.2 Tests using synthetic data

We evaluated the performance of these network filters in two controlled experiments with either non-modular or modular synthetic networks, and varying structures and levels of noise. And, we compare the performance of network filters to other network-based denoising methods that combine values of nodes weighted by a diffusion matrix [150, 151].

In the first experiment, we generated simple random graphs with heavy-tailed degree distributions (see Methods section 3.2.1) and assigned each node a value drawn from a Normal distribution with mean $\mu = 100$ and standard deviation $\sigma = 10$. These values were drawn in such a way that the assortativity coefficient of the network ranged from $r \in [-0.8, 0.8]$ (see Methods section 3.2.2). As a result, connected values ranged from being highly anticorrelated to highly correlated. To sim-

ulate independent measurement noise, we permuted the values among a uniformly random 25% of nodes, and then denoised these "corrupted" values. We find qualitatively similar results for other choices of the fraction permuted. Results report the mean absolute error (MAE) of a denoised value, averaged over 5000 replications.

Without a filter, the average error of a "denoised" value is independent of the underlying correlation (assortativity) among connected values, because this nearby information is left unexploited (Fig. 3.3A). In contrast, applying a network filter to denoise the corrupted values can substantially improve their accuracy, depending on how strongly coupled a measurement's true value is with its neighbors', and what filter is applied to recover that information. For the particular parameters of this experiment, filtering can reduce the error by 37–50% over no filter, and by roughly 20% even in the case of uncorrelated signals ($r = 0$), due to a regression to the mean effect. Error reductions are largest when a network "smoothing" filter is applied to strongly assortative signals, and when a network "sharpening" filter is applied to strongly disassortative signals. That is, denoising works best when the underlying signal structure is matched with the assumptions of the filter.

When the wrong filter is applied, however, error rates can increase relative to not filtering. In such a case, the filter creates more errors in the data than it corrects. On the other hand, this "mismatch" penalty only degrades the overall accuracy at very high levels of correlation (anti-correlation) among the signals, where its magnitude exceeds the natural benefits of filtering at all (Fig. 3.3A). When the underlying correlations are moderate ($|r| < 0.4$), the average benefits of network filtering will tend to outweigh the average error induced applying the wrong filter.

We also applied two other network methods to these non-modular synthetic graphs. These methods denoise data by combining node values weighted by a diffusion kernel. In the method called netSmooth [150], every node is weighted by a personalized PageRank random walk vector [167], which are linearly combined to create a denoised value. The second method is conceptually similar, but uses a graph Laplacian exponential diffusion kernel to weight nodes before linearly combining them to create the new denoised value [151]. Both methods have an adjustable parameter that determines the smoothness of the resulting denoised values. For greater values of this smoothing

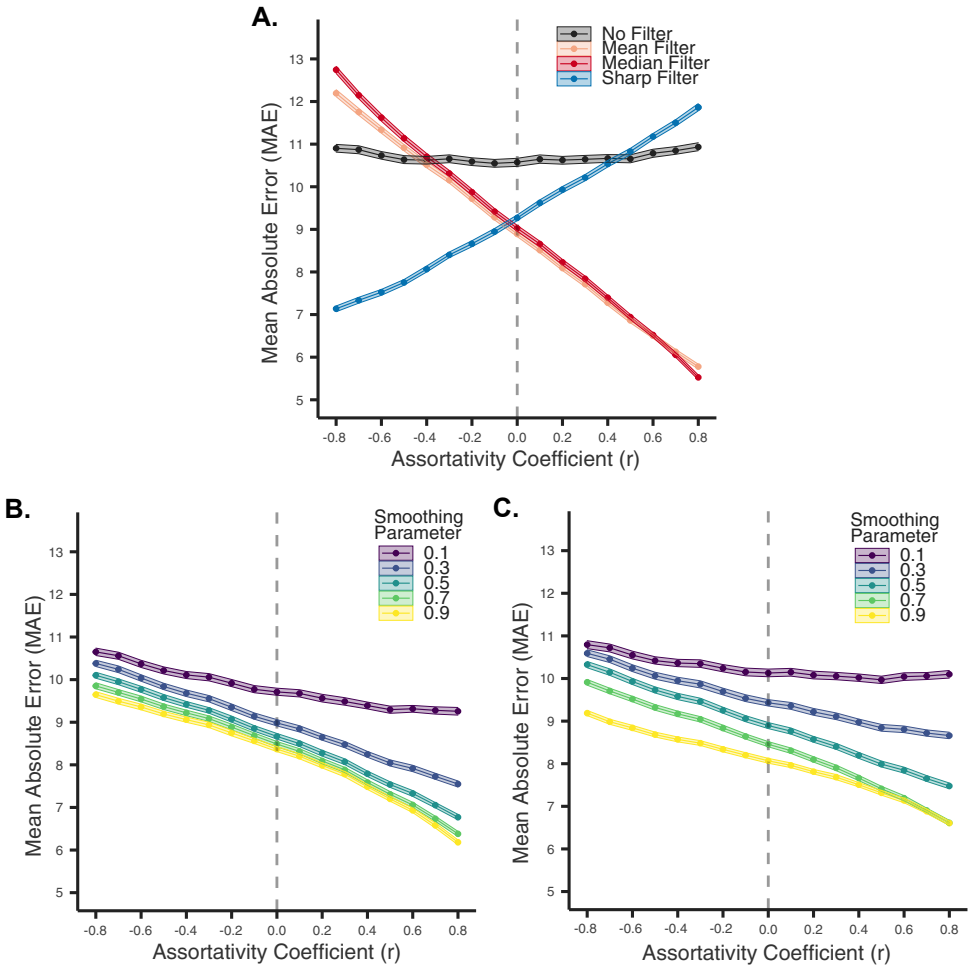

Figure 3.3: Filter performance on non-modular synthetic networks. Network filter tests on synthetic graphs with varying structures and known noise. The Mean Absolute Error (MAE) of **A.** network filters, **B.** Laplacian exponential diffusion kernel, and **C.** netSmooth on the permuted nodes as a function of the assortativty coefficient of 5,000 instances of noisy non-modular graphs. The smooth filters (mean and median) perform best on assortative data ($r > 0$), while the sharp filter is optimal for disassortative data ($r < 0$). When data are neither assortative nor disassortative ($r \approx 0$), netSmooth and Laplacian exponential kernels perform best. The shaded areas indicate 99% bootstrapped confidence intervals.

parameter, the methods place less weight on the node's original noisy value and more weight on distant nodes.

We applied both methods to the same synthetic random graphs as the network filters, while varying the smoothing parameters between low smoothing (parameter = 0.1), and high smoothing (parameter = 0.9). The Laplacian exponential kernel (Fig. 3.3B) and netSmooth (Fig. 3.3C) decrease the error of the noisy data as the assortativity increases. Furthermore, both methods show lower error as the smoothing parameter increases. These diffusion-based methods perform better than the smoothing network filters at either highly dissassortative or weakly assortative values. Since these methods will typically use a larger number of node's values to denoise, their regression to the mean effect tends to be more accurate than the more localized smoothing network filters. However, when a node's value becomes more correlated with its neighbors' values, the smoothing network filters decrease the noise more than the diffusion-based methods. And while the diffusion based methods work better than the smoothing filters on disassortative data, the sharp filter is the best performing method for weakly to strongly disassortative data.

These tests assume that the network structure itself is not noisy. However, in real biological networks, there can be both missing and spurious edges [171]. We tested the robustness of network filters to noise in network structure. After creating a synthetic graph and assigning data to nodes, we add different levels of noise by replacing true edges with new edges between nodes chosen uniformly at random [162]. Thus, this process simulates both cases where the network is missing edges and contains false edges. We find that a noisy network decreases the performance of the mean filter (Fig. 3.4A) and median filter 3.4B) on graphs with assortative data ($r > 0$), and the sharp filter on graphs with disassortative data ($r < 0$) 3.4C). However, the network filters still substantially reduce the error compared to the no-filter baseline. When the network is very noisy (90% rewired edges), applying a filter reduces the error compared to the no-filter baseline. This pattern is due to a regression to the mean effect, since rewiring the network effectively shrinks the assortativity coefficient closer to zero.

In the second experiment, we again generated simple random graphs with heavy-tailed degree

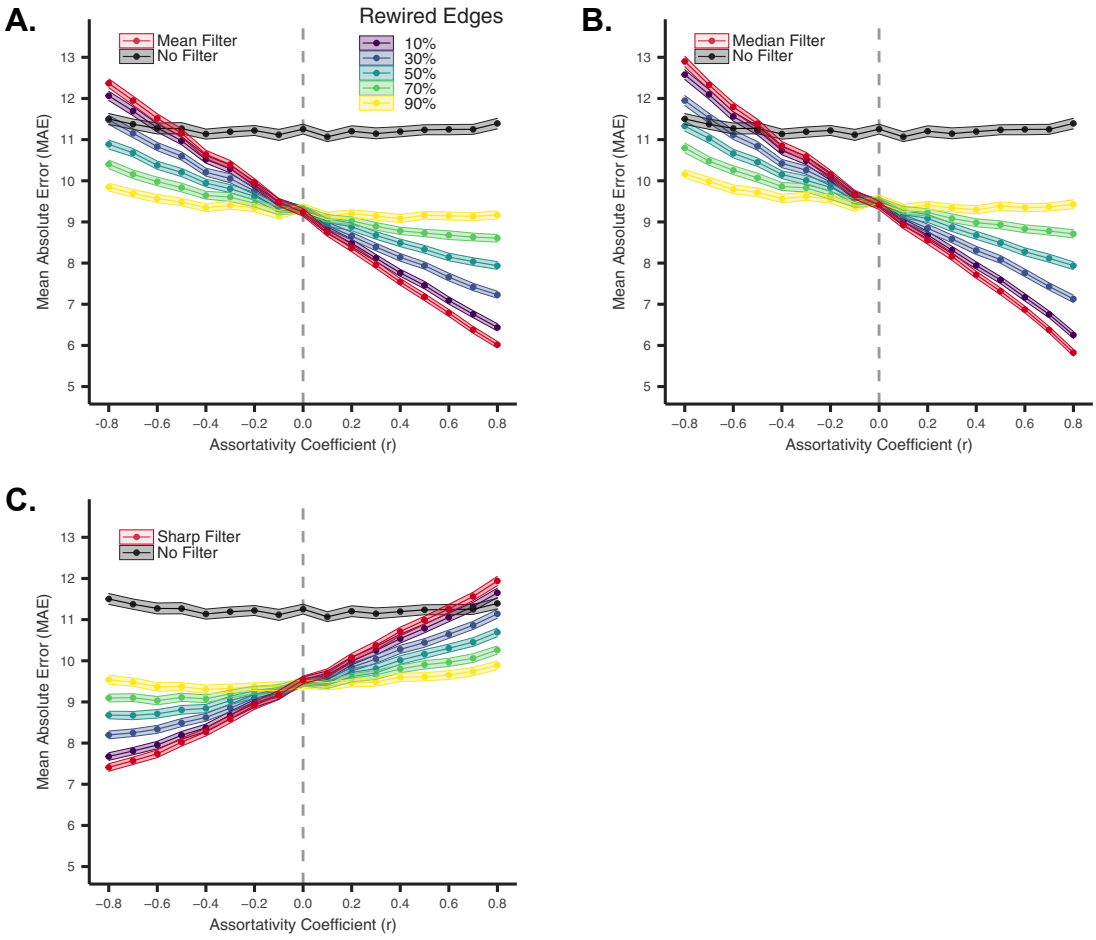

Figure 3.4: Filter performance on rewired synthetic networks. As a test of robustness to incomplete and noisy network structure, we rewire the synthetic networks to remove real edges and add false edges. We plot the average MAE of the **A.** mean filter, **B.** median filter, and **C.** sharp filter applied to the true network and noisy networks. The shaded areas indicate 99% bootstrapped confidence intervals.

distributions, but now also with modular structure, which better captures the structure of empirical biological networks (see Methods 3.2.1). These modules denote groups of nodes that connect to other groups in statistically similar ways. For instance, protein interaction networks can be decomposed into groups with similar biological function, and these groups can have distinct types or levels of signal assortativity [156]. In this situation, applying a single filter to all parts of the network could introduce bias in the denoised values, by pooling nearby measurements indiscriminately, compared to filtering modules independently.

Here, we plant $\kappa = 5$ modules in the same kind of synthetic network as our first experiment, set each module to have a different mean value, and then vary the fraction of modules that have a positive assortativity coefficient $|r| \in [0.4, 0.7]$ vs. a negative coefficient (see Methods section 3.2.1). This kind of signal heterogeneity across modules mitigates the denoising benefits of a simple regression to the mean, and provides a harder test for denoising methods. Given these choices, we generated values within a module, and simulated measurement noise as in the previous experiment (see Methods sections 3.2.1 and3.2.2). In addition to the previous filters, we also apply the "patchwork" filter in this experiment.

As before, the average error of a denoised value with no filter provides a consistent baseline against which we may assess improvements from filtering (Fig. 3.5D). And similarly, the error for both the smooth and median filters falls steadily as the fraction of modules with assortative signals increases. For the particular parameters of this experiment, the median filter performs roughly 20% better than the mean filter, reflecting the median's well-known robustness to outliers, which arise here from the planted signal heterogeneity.

The global sharp filter works poorly for all ratios when applied uniformly across the whole network (Fig. 3.5B). Because each module has a distinct mean value, the global sharp filter generates errors by assuming the global mean is a good representation of the whole network.

In contrast, the patchwork filter with different community detection algorithms exhibits less dynamic range in its error(Fig. 3.5D). When paired with the DC-SBM, it is substantially more accurate than any other filter across different degrees of modular assortativity. For the particular

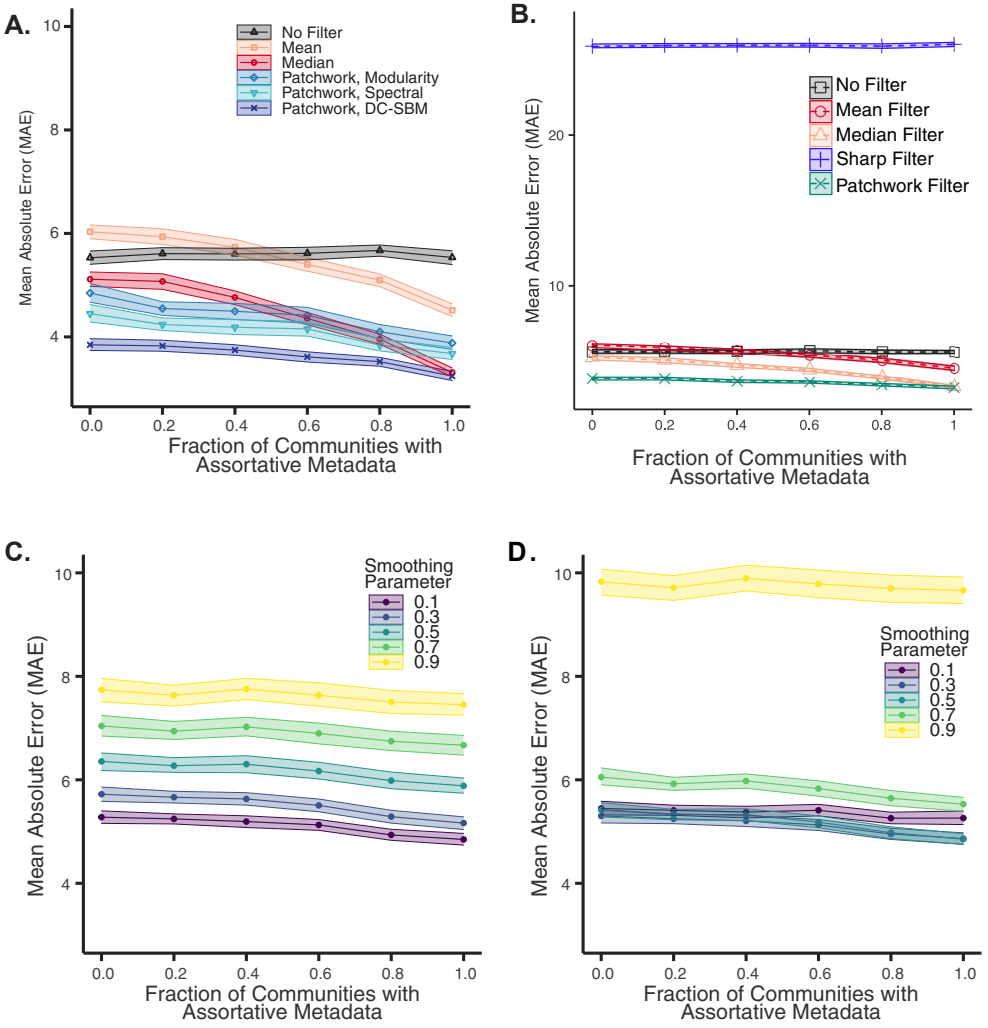

Figure 3.5: Filter performance on modular synthetic networks. The mean absolute error (MAE) of **A.** network filters (without the sharp filter), **B.** network filters including the sharp filter, **C.** Laplacian exponential diffusion kernel, and **D.** netSmooth on the permuted nodes as a function of the fraction of communities with assortative data values for 100 instances of noisy modular graphs. Each network instance has 5 communities and we vary how many communities have assortative vs. disassortative data values with a moderate assortativity coefficient $|r| \in [0.4, 0.7]$. The shaded areas indicate 99% bootstrapped confidence intervals.

parameters of this experiment, the patchwork filter paired with the DC-SBM reduces the mean error by 30–41% compared to no filtering and by 3–36% compared to median or mean filtering. Only when all of the modules are assortative does the median filter come close to the DC-SBM patchwork filter's accuracy. This advantage arises because the patchwork filter avoids applying the same filter to different types of underlying signals, if the structure of those signals correlates with the structure of the network (as it does here). That is, applying a single filter to a modular network can introduce errors when denoising, if the local mixing patterns across modules are heterogeneous. Pairing a community detection algorithm with network filters can avoid this problem by identifying large groups of nodes that should be filtered together, in much the same way that different image filters can be applied after first segmenting an image into distinct regions.

However, for the modularity maximization and spectral partitioning algorithms, the patchwork filter does not perform as well as when paired with the DC-SBM because the algorithms do not partition the network as closely to the true community structure. Thus, the patchwork filter uses measurements from outside a single community more often with these algorithms. Despite imperfect partitioning, the patchwork filter paired with modularity and spectral partitioning algorithms performs 14%-28% better than the mean filter across all levels of modular assortativity. The median filter outperforms the spectral patchwork (9%) and modularity patchwork (15%) at the highest level of modular assortativity, but the patchwork filter still outperforms, or matches the median filter across the rest of the levels of modular assortativity.

We also applied the diffusion-based methods to these synthetic modular networks. The error for both the Laplacian exponential kernel (Fig. 3.5E) and netSmooth (Fig. 3.5F) only slightly decreases as the fraction of modules with assortative signals increases. In contrast to the non-modular case, increasing the smoothing parameter for both methods increases the error across all settings. This loss of accuracy occurs because increasing the smoothing parameter places greater weight on more distant nodes which are more likely to be drawn form a different distribution. Hence, the diffusion kernels are more likely to combine values from nodes from different communities leading to a higher error rate.

3.3.3 Denoising protein expression levels in cancer

To evaluate the utility of network filters for denoising biological data in realistic settings, we construct a machine learning task in which we predict the precise changes in human protein expression levels when a healthy tissue becomes cancerous (see Methods sections 3.2.4 and 3.2.5). This task has potential applications to detecting pre-cancerous lesions [172,173]. We then quantify the improvement in out-of-sample prediction accuracy when using a network filter to denoise the input expression data before model training, compared to training on unfiltered data.

For this experiment, protein expression data are drawn from the Human Protein Atlas (HPA) [168], which provides large-scale immunohistochemistry (IHC) measurements for over 12,000 human proteins in 20 tissues, each in both healthy and cancerous states. Antibody based methods like IHC are known to be noisy and prone to variation from uncontrolled experimental parameters [174], which makes this data set a realistic example of noisy molecular profiling data. A standard principal component analysis (PCA) of the raw HPA expression data reveals that the first component correlates with variations in tissue type, while the second correlates with differences between tissue state (healthy vs. cancerous) (Fig. 3.6A). Some tissues, however, change more than others, and the changes are not always in the same direction. Hence, predicting the precise changes represents a useful and non-trivial machine learning task that network filtering may improve.

For the network filters and diffusion-based methods, we use a comprehensive map of the human protein-protein interaction network (PPIN) [169], which combines data from several interactome databases and is curated for biological interactions with high levels of evidence. While this network represents a broad collection of authoritative interactome data, the completeness of the human PPIN is still uncertain [171], and we do not regard this network as itself noise-free. Taking the intersection of proteins contained in both expression data and interaction network (see Methods section 3.2.4) yields data on $n = 8{,}199$ proteins in a network with $m = 37{,}607$ edges.

In the machine learning task, we perform a K-nearest neighbor regression on an embedded

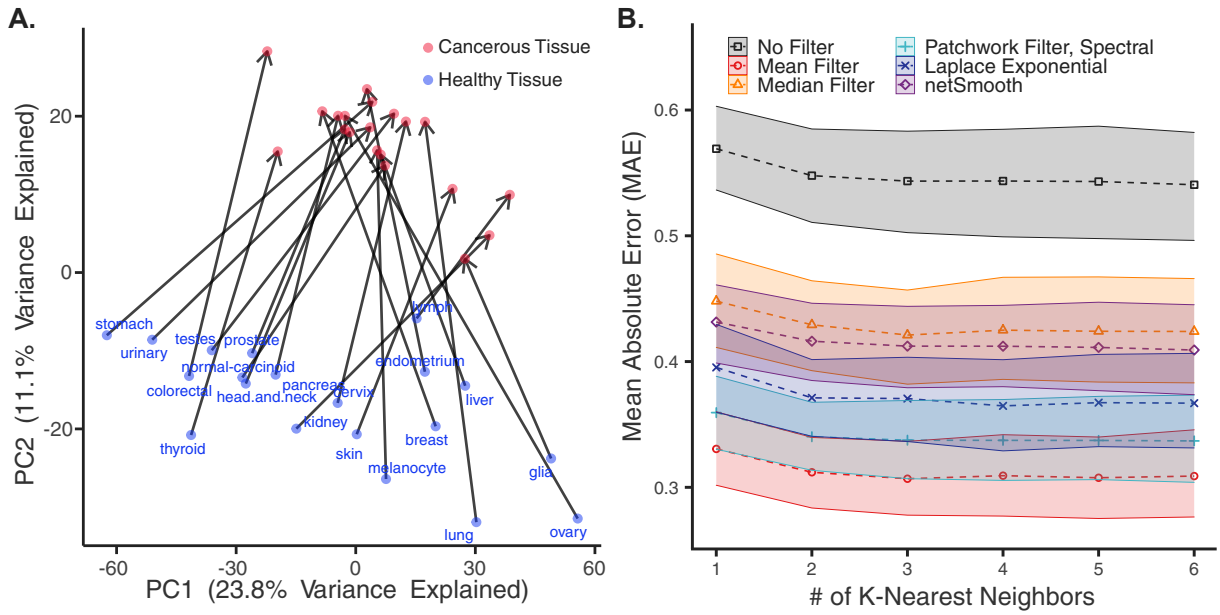

Figure 3.6: Denoising to predict protein expression changes in healthy and cancerous tissues. Tests of the network filters on a cancer protein expression prediction task. In this test, we predict the protein expression changes that occur when a healthy tissue becomes cancerous, quantified by the out-of-sample prediction accuracy with and without using network filters to preprocess the data before training. **A.** The first two principal components of immunohistochemistry data of healthy and cancerous tissues in the Human Protein Atlas. Arrows connect a healthy tissue (blue) to the corresponding cancer (red). The first component captures variations across tissues, while the second captures variation in state (healthy vs. cancerous). Predicting the precise changes between healthy and cancerous tissues is a non-trivial task. Therefore, we perform a K-Nearest Neighbors regression on the HPA data, with and without preprocessing with network filters. We evaluate the model by leave-one-out cross validation, and calculating the MAE of the predicted and actual data values for the left out healthy-cancerous pair. **B.** All network filters and diffusion methods improve the MAE compared to the no-filter baseline. We compare this across different choices of K, as it is a free parameter. The shaded areas represent 95% bootstrapped confidence intervals.

representation of the protein expression data to learn how expression levels change with tissue state (see Methods section 3.2.5). We evaluate the trained model via the MAE between the predicted and the actual changes in protein expression under leave-one-out cross validation (in which we train on 19 tissue pairs, and predict on the 20th) with or without denoising the expression data with a network filter or diffusion-based method prior to model training. Because the number K is a free parameter that controls the complexity of the learned model, we evaluate the robustness of our results by systematically varying K. For the patchwork filter, we partitioned the graph into 10 modules using the DC-SBM [163] or spectral algorithm [165], while the modularity maximization algorithm [166] automatically chooses the number of modules. Then, we apply the mean filter within each module. In this data, most measured values are weakly assortative across protein interaction edges, and only a few detected modules exhibit any disassortative signal, and even then their internal r is relatively close to zero (Fig. 3.7). In this situation, the smooth filter typically outperforms the sharp filter (Fig. 3.3A).

We used the method proposed by Ronen and Akalin to optimize the smoothing parameter for the diffusion based methods by maximizing the entropy of points embedded in a 2-dimensional PCA space [150]. Since the distributions of the healthy tissue and delta vector data are quite different, we optimized the smoothing parameters of each individually.

Across model complexities, we find that denoising before model training using any type of network filter or diffusion-based method provides a substantial reduction in prediction error relative to training on unfiltered data (Fig. 3.6B, Fig. 3.8). The median filter and netSmooth have very similar performance with around 22% improvement in MAE from no filter. The Laplacian exponential diffusion kernel, patchwork filter paired with spectral community detection, and mean network filters have the lowest MAE, improving upon the raw data by 32%, 37%, and 43%, respectively.

Error rates tend to decrease with greater model complexity K, suggesting that more complex models are better able to capture variations in the precise expression level changes between tissue states. This decrease in error also occurs without first filtering the expression data. However, the improvement in prediction accuracy from increasing the model complexity without filtering is

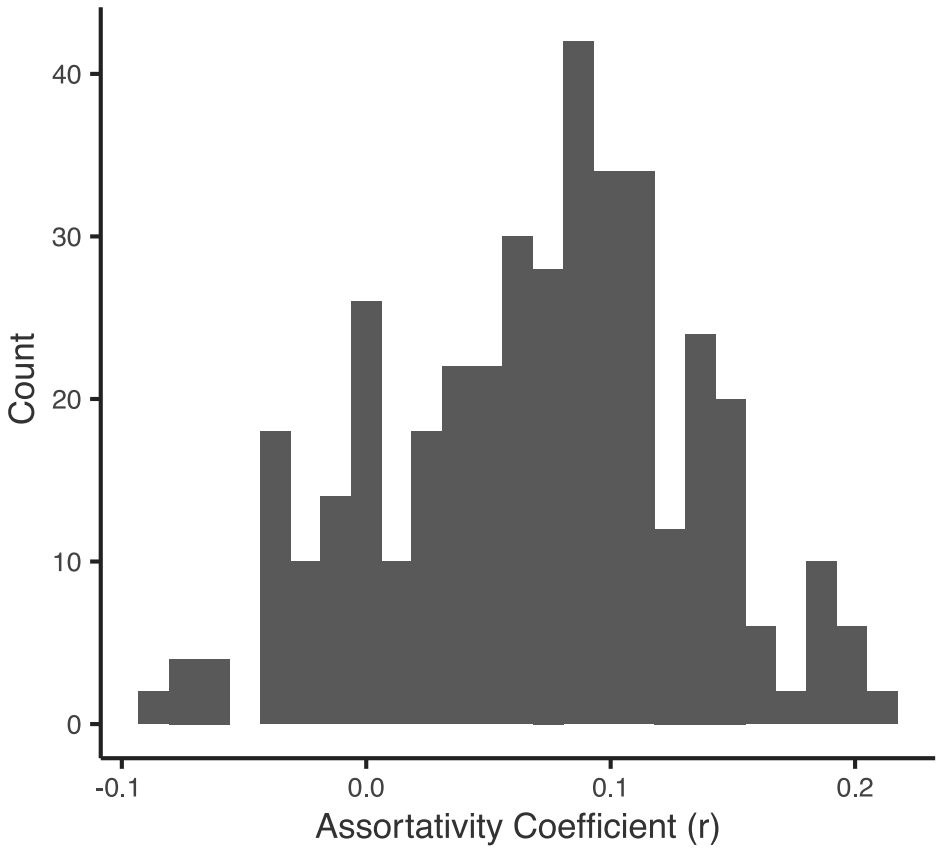

Figure 3.7: Distribution of assortativity coefficients of network modules with Human Protein Atlas data. We partition a protein-protein interaction network into 10 modules using the DC-SBM, and map data from the Human Protein Atlas to this network. Then we calculate the assortativity coefficient of each module with the protein expression of 40 different tissue types. Most modules are slightly assortative, while a few are very slightly disassortative.

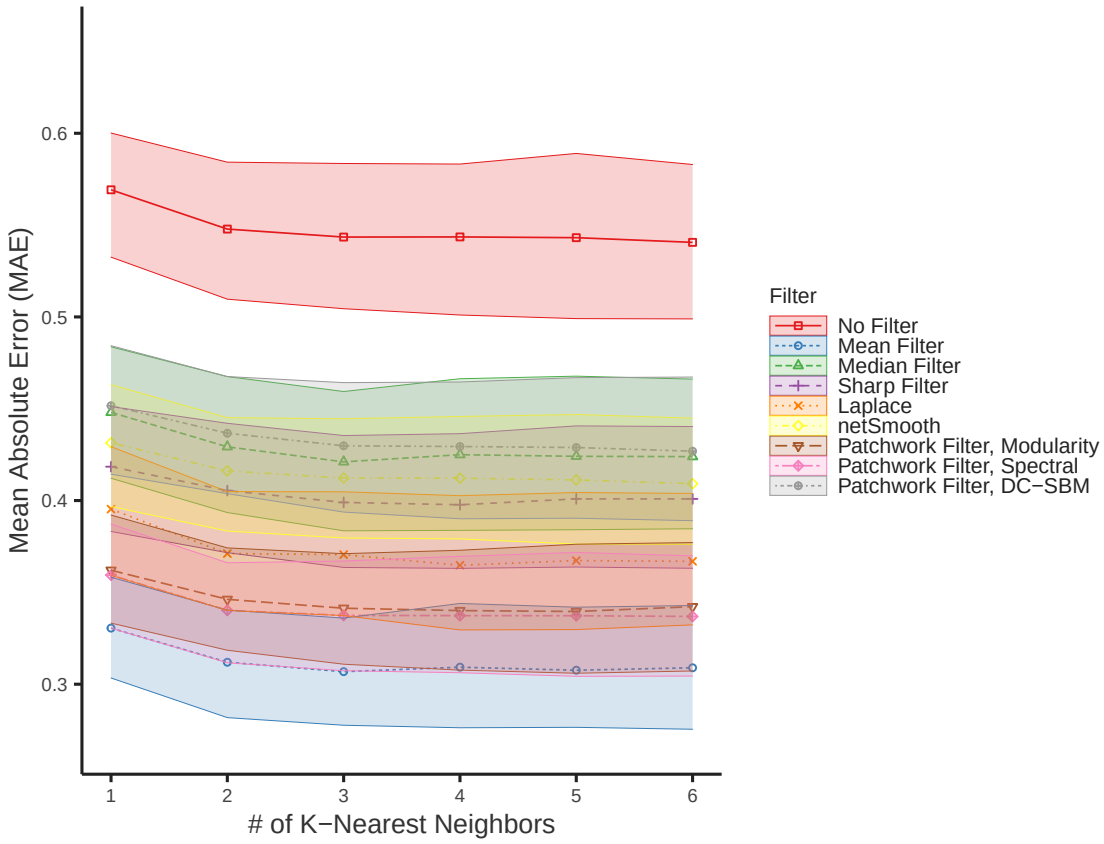

Figure 3.8: KNN regression of Human Protein Atlas data with all network filters. We perform a K-Nearest Neighbors regression on the HPA data, with and without preprocessing with network filters. Here we show all simple global network filters, the patchwork filter with different community detection algorithms, and diffusion based comparison methods.

modest (5.2% at $K = 6$) compared to the improvement from first applying the best network filter (42% at $K = 1$, and 43% at $K = 6$).

We note that in this real-world setting, the patchwork filter, which first partitions the protein interaction network into protein groups, performs better with the spectral or modularity maximization algorithms than with the DC-SBM. The patchwork filter paired with these algorithms performed very well, but the mean filter still performed better than them. This behavior suggests that the partitions produced by the community detection algorithms did not correlate sufficiently strongly with the underlying variation in biological signals to correctly localize the most relevant adjacent measurements, in contrast to our controlled experiments (Fig. 3.3D). Developing community detection algorithms that choose more biologically relevant partitions may be a useful direction of future work.

3.4 Discussion

Large data sets of biological signals, such as system-wide measurements of molecular concentrations, are often noisy. However, these measurements are not fully independent because they reflect the dynamics of a single interconnected system. Using a network to represent the underlying biological relationships among a set of measurements, we can leverage the size of these data sets to systematically denoise many measurements at once, improving the data's utility for understanding the structure and dynamics of complex biological systems or making accurate predictions in systems biology.

Experiments using synthetic data with realistic biological network structures and a variety of underlying signals indicates that network filters can substantially reduce noise in large biological data sets across a broad range of circumstances (Fig. 3.3A, 3.5D, Fig. 3.4). The greatest benefit is obtained when the type of filter is matched to the underlying relationship among the signals, e.g., smoothing for assortative signals (correlation) and sharpening for disassortative signals (anti-correlation). However, for modest levels of correlation, even the wrong kind of filter yields some benefit because of a regression to the mean effect, in which combining several related signals filters

out more noise than it introduces through bias. When signal types are heterogeneous across the network, so that the strength or direction of the correlation differs in different parts of the network, a "patchwork" filter often performs better. In this approach, we first partition the network into smaller, more homogeneous modules (groups of interrelated measurements) and then apply filters independently to the measurements now localized within each module (Fig. 3.3D).

In a more realistic setting, in which we train a machine learning algorithm to predict changes in human protein expression levels when healthy tissue becomes cancerous, applying a network filter based on a high-quality protein interaction network before model training substantially improves prediction accuracy, compared to training on unfiltered data (Fig. 3.6B). In this experiment, the protein interaction network itself is not noise-free [171], indicating that filtering using an imperfect network can be better than not filtering at all. Our experiment on rewiring network edges further supports that network filters still work well on noisy network structures (Fig. 3.4).

In each experiment, we compared our network filters to techniques relying on network diffusion algorithms to weight the nodes before combining them. Both netSmooth and the Laplacian exponential diffusion kernel have similar characteristics to the smoothing network filters. In the non-modular synthetic graphs, they perform better with more assortative underlying data. However, on modular graphs with heterogeneous data values, the performance only slightly increases as more communities have assortative data values, and decreases when communities have disassortative values.

We find an apparent trade-off between the size of the local area of nodes used to denoise a value and the range of values that can be recovered. The diffusion-based techniques outperform local smoothing network filters when there is no correlation or anti-correlation between neighboring values. This improvement is caused by a larger regression to the mean effect from using many more neighbors to denoise any given value. While this effect is beneficial in the experiment with non-modular synthetic graphs, it strongly hinders their performance on modular graphs with heterogenous data values because the diffusion-based techniques tend to use values outside their community, which are drawn from different underlying distributions. Furthermore, increasing the

smoothing parameter increases the weight of values outside of the community, strongly deteriorating their performance. Thus, regression to the mean is not beneficial in this experiment since each community has a different distribution of data values. On the other hand, the mean and median filters are more localized and hence make fewer errors due to combining neighbors' values from different communities.

Network filters are ultimately systems-level tools applied to a group of related biological measurements to reduce the overall noise in the system of measurements. On balance, applying network filters reduces the noise in a system of measurements, as evidenced by our tests on synthetic and real datasets. However, there is no guarantee that every individual node's measurement is less noisy after applying a network filter. Furthermore, network filters increase the correlation (or anti-correlation) between the set of denoised values, which reduces the effective sample size. Thus, narrowing the focus to individual nodes after filtering the whole dataset is not the intended use case of network filters. Network filters have the greatest potential for answering questions that take the dataset as a whole, like our machine learning example, rather than considering data of single nodes, such as differential gene expression analysis. Such problems will require more specialized tools specifically suited to the input data.

Network filters could be useful for datasets beyond the ones we describe here, as they only require that a network explains the causal structure of a system of measurements. But some input data may not benefit in its raw form by using network filters particularly if it does not make sense to average together a set of the raw values. For example, in the IHC data from the HPA, each protein is on the same scale of none, low, medium, or high expression level which we converted to a numeric value between zero to three. Since the values of each protein are on the same scale, averaging them together in the smooth filter is reasonable and will produce a value that has shifted to look more like its neighbor nodes. However, other types of data such as intensities from mass spectrometry based proteomics or raw read counts from RNA-seq can have wildly different scales between proteins and transcripts, which is inherent in the measurement platform. Taking the average of these measurements could create nonsensical values that are largely different from the

raw values, and thus may not denoise the data very well. In these cases, transformations of the raw data, like z-score standardization of a node's values across different samples, may be more appropriate.

There are a number of potentially valuable directions for future work on network filters, which may improve their error rates or adapt them to more complicated settings or tasks. Techniques from image processing, both simple and advanced, represent a particularly promising direction to explore [175–177]. For instance, here, we only considered the network filters combine measurements associated with directly adjacent nodes. As a result, the denoised values associated with low degree nodes in the network derive from a relatively smaller number of measurements, and hence are likely to have larger residual noise than will higher degree nodes. Modifying the network filter for low degree nodes to look beyond nearest neighbors, e.g., to ensure a minimum number of pooled measurements per node, may provide better guarantees on the accuracy of the denoised value. An example of this type of technique in image processing include the Gaussian filter [178].

Image segmentation, in which an image is first partitioned into visually distinct pieces, e.g., separating the foreground from the background, is a common preprocessing step in image analysis. The patchwork filter considered here is a simple adaptation of this idea, but it relies on off-the-shelf community detection algorithms to partition the nodes, considers different modules independently, and ignores connections that run between modules. While this approach should retain the most informative relationships among the measurements it also serves to reduce the degrees of many nodes, which may lessen the benefits of filtering, as described above. Furthermore, the patchwork filter will not work well on networks with disassortative community structure where nodes in the same community tend to not form edges between each other. In such cases, the patchwork filter would significantly reduce the degree of all nodes and limit the potential for network filters to denoise their data. Thus, the patchwork filter may perform best with community detection algorithms that return assortative community structures and sever the least number of edges within communities.

Developing filters that utilize the edges between modules could mitigate the induced low-degree effects that come from applying a patchwork filter to account for signal heterogeneity in

the system. Such between-module edges should likely be considered separately from within-module edges, e.g., by adjusting their weights w_{ij} to more accurately capture the character of the particular signal relationship between the modules containing nodes i and j.

The benefits of a patchwork filter necessarily depends on how closely the network partition correlates with the underlying biological structure of the system. Off-the-shelf community detection algorithms may not always provide such partitions [179]. While the DC-SBM was able to recover partitions that were good for denoising in the synthetic data task, it did not perform as well as the modularity maximization and spectral algorithms on the real world data example. Since the assortativity coefficients for the Human Protein Atlas range from 0 to 0.1, the benefit is dominated by the regression to the mean effect, which does better on higher degree nodes to reduce the noise. Thus, the community detection method that finds partitions optimal for denoising may differ network to network [170]. Trying a few different community detection methods like we did here should aid in finding network partitions that best correlate with the system's underlying structure. In some settings, developing application-specific partitioning algorithms, or algorithms that can exploit biologically meaningful node attributes [164], may improve the behavior of a patchwork filter. For data sets where the data is relatively homogenous, a smoothing or sharpening filter applied to the network as a whole may provide more benefits than the patchwork filter.

Finally, the network filters defined here make few specific assumptions about the underlying noise-generating process itself. In specific applications, much more may be known about the direction, magnitude, and clustering of errors across large-scale measurements. For instance, in molecular profiling data, endogenous biological factors like cell cycle effects likely induce distinct noise patterns compared to exogenous technical factors like sample preparation or instrument variation. Developing more application specific error models that could be combined with network filters may provide more powerful denoising techniques than the general filters described here.

Chapter 4

Conclusions and outlook

In Chapter 2, I investigated how intermittent treatment makes melanoma cells sensitive to rechallenge. In this work, we challenge the prevailing drug addiction model to explain the beneficial response to intermittent treatment compared to continuous treatment. This model proposes that there is an alternating selection between drug sensitive and drug resistant cells during drug treatment and drug withdrawal, respectively. While our system shows evidence of drug addiction, drug resensitization has a much greater contribution to cell death and overall reduced cell numbers in intermittent treatment compared to continuous treatment.

Using RNA-seq, we discovered that drug treatment induces transcriptomic reprogramming and an EMT-like phenotype switch resulting in a more drug tolerant population. Drug withdrawal only partially reverts this transcriptomic shift away from the drug tolerant invasive phenotype. Interestingly, some of the highly reported markers of the drug tolerant invasive state ($MITF^{low}/AXL^{high}$) do not revert to expression levels seen in the sensitive, melanocytic cell state. However, our cells clearly regain sensitivity to drug during withdrawal as indicated by a left-shift in the dose response curve and increased percent of propidium iodide stained cells upon drug re-addition.

We demonstrated that the reversible gene expression from our bulk RNA-seq data is not due to selection against a subpopulation. Instead, single cells switch from one transcriptomic state to another ($L1CAM^{High}$ to $L1CAM^{Low}$). This was evident from the unimodal distribution of L1CAM expresssion in the early days of drug withdrawal that was at intermediate levels between those seen

at Day 7 (resistant L1CAM^{High}) or Day 14 (sensitive L1CAM^{Low}). In essence, we see cells that were caught in the act of reverting from the resistant state to the sensitive state. Our propidium iodide staining and growth curve experiments also show that there is not much cell growth or cell death during these timepoints. Certainly not enough to explain a 10-fold decrease in median L1CAM protein expression.

There are many future directions this project could take to understand intermittent treatment in more detail. In particular, the most important avenue is to test more melanoma cell lines to see if they demonstrate a beneficial response to intermittent drug treatment relative to continuous treatment. In Appendix A, I show results for several other melanoma cell lines I tested for their responses to intermittent drug treatment. In short, the conditions used for WM239A-BRAF^{V600E} cells did not show a beneficial intermittent treatment effect in the other cell lines I've tested. I have made changes to drug concentration, intermittent schedule, and seeding density, but have not seen a beneficial intermittent treatment response in other cell lines. Thus, we don't quite understand all the components that make intermittent treatment successful.

Multiple cell lines do show a decrease in cell numbers with drug rechallenge after a period of drug withdrawal. With more optimization of the conditions, some of these cell lines may show reduced cell numbers with intermittent treatment compared to continuous treatment. WM239A cells without an over-expressed oncogene capable of activating the MAPK pathway do not show the beneficial intermittent response, so perhaps this oncogene overexpression is required in the other cell types too.

One interesting observation in our RNA-seq dataset was that the some genes do not change expression levels with oncogene induction, acute drug treatment, or continuous drug treatment. But somehow these genes somehow acquire responsiveness to MAPK signaling across the drug-off/drug-on/drug-off intermittent schedule. These are very interesting, and we have not studied them in much detail. Some of these appear in Fig. 2.13, such as IL1B, AREG, FGFR1, and MET. Potentially, these genes require a high threshold of ppERK seen in the drug-off intermittent weeks to activate their transcription. It would be interesting to conduct a phosphoproteomics experiment

to investigate if there are new ERK target proteins that are only phosphorylated upon pathway hyperactivation. These new targets may regulate the expression of these genes that seem to acquire MAPK signaling dependency, and potentially be responsible for drug resensitization.

In Chapter 3, I developed a suite of tools called network filters that can be used to denoise large scale biological data. Network filters are flexible tools that can exploit a variety of network data, including networks of molecular binding interactions. We can extend network filters to exploit information about the sign or strength of interactions or to allow the type of interaction to vary across different modules within the network. These filters can also be applied to networks of any size, ranging from local signaling pathways to entire protein interaction networks. While our focus was on biological data, network filters are truly agnostic to the source of the data. In fact, they can be applied to any network that correlates with the underlying causal structure of a set of measured variables. By exploiting these underlying relationships, a network filter pools correlated information, which mitigates independent noise, in much the same way that image processing techniques use information from nearby pixels to denoise an image.

A major innovation of this study was paring network filters with community detection algorithms. The patchwork filter can theoretically adapt to networks where there are heterogeneous patterns of assortativity and disassortativity and apply smoothing or sharpening filters to different nodes. In tests of synthetic data, the patchwork filter could identify communities with homogeneous mixing and apply the appropriate network filter within those communities. However, the patchwork filter did not have optimal performance in the real data machine learning task. Fundamentally, this means the communities identified from the three different community detection algorithms did not partition the graph into units that optimally correlate with the underlying biological signals. An inherent limitation to the patchwork filter that is severing edges between nodes in different communities decreases the degree of the nodes, and low degree nodes are more susceptible to errors. Isolating communities is good in instances where the patchwork filter applies different filters to communities with opposite mixing patterns. However, in the case of the protein protein interaction network where there is not a strong correlation between mixing pattern and community structure,

reducing the effective node degrees performance decreased the performance of the patchwork filter more than the benefit of separating communities. This effect was evident since the spectral community detection algorithm severed fewer edges between nodes and outperformed the DC-SBM, which across the board severed many more edges.

For the patchwork filter to succeed on a wider variety of networks, it will be important to use community detection methods that are designed to identify groups of connected nodes with correlated or anti-correlated data. The DC-SBM, modularity, and spectral community detection algorithms we used on the Human Protein Atlas dataset were general-off-the shelf implementations that did not use the associated node data during partitioning. Thus, the communities they identified were based solely on network structure. Using a metadata-aware version of the DC-SBM in the synthetic data task partitioned the graph near-opitmally for the patchwork filter performance. However, this algorithm would not converge on a solution for some of the cancer datasets paired with protein-protein interaction network. Adapting this community detection algorithm or others to identify communities with homogenous data mixing patterns would greatly increase the power of the patchwork filter.

Bibliography

[1] Schadendorf D, Fisher DE, Garbe C, Gershenwald JE, Grob JJ, Halpern A, et al. Melanoma. *Nature Reviews Disease Primers*. 2015;1(1):1–20.

[2] Miller AJ, Mihm Jr MC. Melanoma. *New England Journal of Medicine*. 2006;355(1):51–65.

[3] SEER Cancer Stat Facts: Melanoma of the Skin. Bethesda, MD: National Cancer Institute;. Available from: `https://seer.cancer.gov/statfacts/html/melan.html`.

[4] Yeh I, von Deimling A, Bastian BC. Clonal BRAF mutations in melanocytic nevi and initiating role of BRAF in melanocytic neoplasia. *Journal of the National Cancer Institute*. 2013;105(12):917–919.

[5] Viros A, Sanchez-Laorden B, Pedersen M, Furney SJ, Rae J, Hogan K, et al. Ultraviolet radiation accelerates BRAF-driven melanomagenesis by targeting TP53. *Nature*. 2014;511(7510):478–482.

[6] Michaloglou C, Vredeveld LC, Soengas MS, Denoyelle C, Kuilman T, Van Der Horst CM, et al. BRAF E600-associated senescence-like cell cycle arrest of human naevi. *Nature*. 2005;436(7051):720–724.

[7] Bansal R, Nikiforov MA. Pathways of oncogene-induced senescence in human melanocytic cells. *Cell Cycle*. 2010;9(14):2854–2860.

[8] Haferkamp S, Scurr LL, Becker TM, Frausto M, Kefford RF, Rizos H. Oncogene-induced senescence does not require the p16INK4a or p14ARF melanoma tumor suppressors. *Journal of Investigative Dermatology*. 2009;129(8):1983–1991.

[9] Kuilman T, Michaloglou C, Vredeveld LC, Douma S, van Doorn R, Desmet CJ, et al. Oncogene-induced senescence relayed by an interleukin-dependent inflammatory network. *Cell*. 2008;133(6):1019–1031.

[10] Thompson JF, Scolyer RA, Kefford RF. Cutaneous melanoma. *The Lancet*. 2005;365(9460):687–701.

[11] Sauter ER, Yeo UC, von Stemm A, Zhu W, Litwin S, Tichansky DS, et al. Cyclin D1 is a candidate oncogene in cutaneous melanoma. *Cancer Research*. 2002;62(11):3200–3206.

[12] Mikesh LM, Kumar M, Erdag G, Hogan KT, Molhoek KR, Mayo MW, et al. Evaluation of molecular markers of mesenchymal phenotype in melanoma. *Melanoma Research*. 2010;20(6):485.

[13] Da Forno PD, Pringle JH, Hutchinson P, Osborn J, Huang Q, Potter L, et al. WNT5A expression increases during melanoma progression and correlates with outcome. *Clinical Cancer Research*. 2008;14(18):5825–5832.

[14] Dissanayake SK, Wade M, Johnson CE, O'Connell MP, Leotlela PD, French AD, et al. The Wnt5A/protein kinase C pathway mediates motility in melanoma cells via the inhibition of metastasis suppressors and initiation of an epithelial to mesenchymal transition. *Journal of Biological Chemistry*. 2007;282(23):17259–17271.

[15] Lewis TS, Shapiro PS, Ahn NG. Signal transduction through MAP kinase cascades. *Advances in Cancer Research*. 1998;74:49–139.

[16] Santarpia L, Lippman SM, El-Naggar AK. Targeting the MAPK–RAS–RAF signaling pathway in cancer therapy. *Expert Opinion on Therapeutic Targets*. 2012;16(1):103–119.

[17] Akbani R, Akdemir KC, Aksoy BA, Albert M, Ally A, Amin SB, et al. Genomic classification of cutaneous melanoma. *Cell*. 2015;161(7):1681–1696.

[18] Roskoski Jr R. RAF protein-serine/threonine kinases: structure and regulation. *Biochemical and Biophysical Research Communications*. 2010;399(3):313–317.

[19] Davies H, Bignell GR, Cox C, Stephens P, Edkins S, Clegg S, et al. Mutations of the BRAF gene in human cancer. *Nature*. 2002;417(6892):949–954.

[20] Dhanasekaran N, Reddy EP. Signaling by dual specificity kinases. *Oncogene*. 1998;17(11):1447–1455.

[21] Kyriakis JM, App H, Zhang Xf, Banerjee P, Brautigan DL, Rapp UR, et al. Raf-1 activates MAP kinase-kinase. *Nature*. 1992;358(6385):417–421.

[22] Posada J, Yew N, Ahn N, Vande Woude G, Cooper J. Mos stimulates MAP kinase in Xenopus oocytes and activates a MAP kinase kinase in vitro. *Molecular and Cellular Biology*. 1993;13(4):2546–2553.

[23] O'Shaughnessy EC, Palani S, Collins JJ, Sarkar CA. Tunable signal processing in synthetic MAP kinase cascades. *Cell*. 2011;144(1):119–131.

[24] Mansour SJ, Matten WT, Hermann AS, Candia JM, Rong S, Fukasawa K, et al. Transformation of mammalian cells by constitutively active MAP kinase kinase. *Science*. 1994;265(5174):966–970.

[25] Stuart SA, Houel S, Lee T, Wang N, Old WM, Ahn NG. A Phosphoproteomic Comparison of B-RAFV600E and MKK1/2 Inhibitors in Melanoma Cells*[S]. *Molecular & Cellular Proteomics*. 2015;14(6):1599–1615.

[26] Basken J, Stuart SA, Kavran AJ, Lee T, Ebmeier CC, Old WM, et al. Specificity of phosphorylation responses to mitogen activated protein (MAP) kinase pathway inhibitors in melanoma cells. *Molecular & Cellular Proteomics*. 2018;17(4):550–564.

[27] Meloche S, Pouysségur J. The ERK1/2 mitogen-activated protein kinase pathway as a master regulator of the G1-to S-phase transition. *Oncogene*. 2007;26(22):3227–3239.

[28] Shaulian E, Karin M. AP-1 in cell proliferation and survival. *Oncogene*. 2001;20(19):2390–2400.

[29] Murphy LO, Smith S, Chen RH, Fingar DC, Blenis J. Molecular interpretation of ERK signal duration by immediate early gene products. *Nature Cell Biology*. 2002;4(8):556–564.

[30] Min M, Rong Y, Tian C, Spencer SL. Temporal integration of mitogen history in mother cells controls proliferation of daughter cells. *Science*. 2020;368(6496):1261–1265.

[31] Balmanno K, Cook S. Tumour cell survival signalling by the ERK1/2 pathway. *Cell Death & Differentiation*. 2009;16(3):368–377.

[32] Ewings KE, Hadfield-Moorhouse K, Wiggins CM, Wickenden JA, Balmanno K, Gilley R, et al. ERK1/2-dependent phosphorylation of BimEL promotes its rapid dissociation from Mcl-1 and Bcl-xL. *The EMBO Journal*. 2007;26(12):2856–2867.

[33] Arvind R, Shimamoto H, Momose F, Amagasa T, Omura K, Tsuchida N. A mutation in the common docking domain of ERK2 in a human cancer cell line, which was associated with its constitutive phosphorylation. *International Journal of Oncology*. 2005;27(6):1499–1504.

[34] Bott CM, Thorneycroft SG, Marshall CJ. The sevenmaker gain-of-function mutation in p42 MAP kinase leads to enhanced signalling and reduced sensitivity to dual specificity phosphatase action. *FEBS Letters*. 1994;352(2):201–205.

[35] Taylor CA, Cormier KW, Keenan SE, Earnest S, Stippec S, Wichaidit C, et al. Functional divergence caused by mutations in an energetic hotspot in ERK2. *Proceedings of the National Academy of Sciences USA*. 2019;116(31):15514–15523.

[36] Yarden Y, Schlessinger J. Epidermal growth factor induces rapid, reversible aggregation of the purified epidermal growth factor receptor. *Biochemistry*. 1987;26(5):1443–1451.

[37] Honegger A, Kris R, Ullrich A, Schlessinger J. Evidence that autophosphorylation of solubilized receptors for epidermal growth factor is mediated by intermolecular cross-phosphorylation. *Proceedings of the National Academy of Sciences USA*. 1989;86(3):925–929.

[38] Nicholson RI, Gee JMW, Harper ME. EGFR and cancer prognosis. *European Journal of Cancer*. 2001;37:9–15.

[39] Wu SG, Yu CJ, Tsai MF, Liao WY, Yang CH, Jan IS, et al. Survival of lung adenocarcinoma patients with malignant pleural effusion. *European Respiratory Journal*. 2013;41(6):1409–1418.

[40] Batzer A, Rotin D, Urena J, Skolnik E, Schlessinger J. Hierarchy of binding sites for Grb2 and Shc on the epidermal growth factor receptor. *Molecular and Cellular Biology*. 1994;14(8):5192–5201.

[41] Chardin P, Camonis JH, Gale NW, Van Aelst L, Schlessinger J, Wigler MH, et al. Human Sos1: a guanine nucleotide exchange factor for Ras that binds to GRB2. *Science*. 1993;260(5112):1338–1343.

[42] Prior IA, Lewis PD, Mattos C. A comprehensive survey of Ras mutations in cancer. *Cancer Research*. 2012;72(10):2457–2467.

[43] Smith MJ, Neel BG, Ikura M. NMR-based functional profiling of RASopathies and oncogenic RAS mutations. *Proceedings of the National Academy of Sciences USA*. 2013;110(12):4574–4579.

[44] Bollag G, Clapp DW, Shih S, Adler F, Zhang YY, Thompson P, et al. Loss of NF1 results in activation of the Ras signaling pathway and leads to aberrant growth in haematopoietic cells. *Nature Genetics*. 1996;12(2):144–148.

[45] Nissan MH, Pratilas CA, Jones AM, Ramirez R, Won H, Liu C, et al. Loss of NF1 in cutaneous melanoma is associated with RAS activation and MEK dependence. *Cancer Research*. 2014;74(8):2340–2350.

[46] Garbe C, Eigentler TK, Keilholz U, Hauschild A, Kirkwood JM. Systematic review of medical treatment in melanoma: current status and future prospects. *The Oncologist*. 2011;16(1):5.

[47] Tsai J, Lee JT, Wang W, Zhang J, Cho H, Mamo S, et al. Discovery of a selective inhibitor of oncogenic B-Raf kinase with potent antimelanoma activity. *Proceedings of the National Academy of Sciences USA*. 2008;105(8):3041–3046.

[48] Kim G, McKee AE, Ning YM, Hazarika M, Theoret M, Johnson JR, et al. FDA approval summary: vemurafenib for treatment of unresectable or metastatic melanoma with the BRAFV600E mutation. *Clinical Cancer Research*. 2014;20(19):4994–5000.

[49] Bollag G, Hirth P, Tsai J, Zhang J, Ibrahim PN, Cho H, et al. Clinical efficacy of a RAF inhibitor needs broad target blockade in BRAF-mutant melanoma. *Nature*. 2010;467(7315):596–599.

[50] Kefford R, Arkenau H, Brown M, Millward M, Infante J, Long G, et al. Phase I/II study of GSK2118436, a selective inhibitor of oncogenic mutant BRAF kinase, in patients with metastatic melanoma and other solid tumors. *Journal of Clinical Oncology*. 2010;28(15_suppl):8503–8503.

[51] Koelblinger P, Thuerigen O, Dummer R. Development of encorafenib for BRAF-mutated advanced melanoma. *Current Opinion in Oncology*. 2018;30(2):125.

[52] Hatzivassiliou G, Song K, Yen I, Brandhuber BJ, Anderson DJ, Alvarado R, et al. RAF inhibitors prime wild-type RAF to activate the MAPK pathway and enhance growth. *Nature*. 2010;464(7287):431–435.

[53] Roskoski Jr R. Allosteric MEK1/2 inhibitors including cobimetanib and trametinib in the treatment of cutaneous melanomas. *Pharmacological Research*. 2017;117:20–31.

[54] Ohren JF, Chen H, Pavlovsky A, Whitehead C, Zhang E, Kuffa P, et al. Structures of human MAP kinase kinase 1 (MEK1) and MEK2 describe novel noncompetitive kinase inhibition. *Nature Structural & Molecular Biology*. 2004;11(12):1192–1197.

[55] Ascierto PA, Dummer R, Gogas HJ, Flaherty KT, Arance A, Mandala M, et al. Update on tolerability and overall survival in COLUMBUS: landmark analysis of a randomised phase 3 trial of encorafenib plus binimetinib vs vemurafenib or encorafenib in patients with BRAF V600–mutant melanoma. *European Journal of Cancer*. 2020;126:33–44.

[56] Flaherty KT, Puzanov I, Kim KB, Ribas A, McArthur GA, Sosman JA, et al. Inhibition of mutated, activated BRAF in metastatic melanoma. *New England Journal of Medicine*. 2010;363(9):809–819.

[57] Chapman PB, Hauschild A, Robert C, Haanen JB, Ascierto P, Larkin J, et al. Improved survival with vemurafenib in melanoma with BRAF V600E mutation. *New England Journal of Medicine*. 2011;364(26):2507–2516.

[58] Shi H, Moriceau G, Kong X, Lee MK, Lee H, Koya RC, et al. Melanoma whole-exome sequencing identifies V600E B-RAF amplification-mediated acquired B-RAF inhibitor resistance. *Nature Communications*. 2012;3(1):1–8.

[59] Poulikakos PI, Persaud Y, Janakiraman M, Kong X, Ng C, Moriceau G, et al. RAF inhibitor resistance is mediated by dimerization of aberrantly spliced BRAF (V600E). *Nature*. 2011;480(7377):387–390.

[60] Yao Z, Torres NM, Tao A, Gao Y, Luo L, Li Q, et al. BRAF mutants evade ERK-dependent feedback by different mechanisms that determine their sensitivity to pharmacologic inhibition. *Cancer Cell*. 2015;28(3):370–383.

[61] Yao Z, Gao Y, Su W, Yaeger R, Tao J, Na N, et al. RAF inhibitor PLX8394 selectively disrupts BRAF dimers and RAS-independent BRAF-mutant-driven signaling. *Nature Medicine*. 2019;25(2):284–291.

[62] Long GV, Fung C, Menzies AM, Pupo GM, Carlino MS, Hyman J, et al. Increased MAPK reactivation in early resistance to dabrafenib/trametinib combination therapy of BRAF-mutant metastatic melanoma. *Nature Communications*. 2014;5(1):1–9.

[63] Van Allen EM, Wagle N, Sucker A, Treacy DJ, Johannessen CM, Goetz EM, et al. The genetic landscape of clinical resistance to RAF inhibition in metastatic melanoma. *Cancer Discovery*. 2014;4(1):94–109.

[64] Nazarian R, Shi H, Wang Q, Kong X, Koya RC, Lee H, et al. Melanomas acquire resistance to B-RAF (V600E) inhibition by RTK or N-RAS upregulation. *Nature*. 2010;468(7326):973–977.

[65] Ramirez M, Rajaram S, Steininger RJ, Osipchuk D, Roth MA, Morinishi LS, et al. Diverse drug-resistance mechanisms can emerge from drug-tolerant cancer persister cells. *Nature Communications*. 2016;7(1):1–8.

[66] Yang C, Tian C, Hoffman TE, Jacobsen NK, Spencer SL. Melanoma subpopulations that rapidly escape MAPK pathway inhibition incur DNA damage and rely on stress signalling. *Nature Communications*. 2021;12(1):1–14.

[67] Lito P, Pratilas CA, Joseph EW, Tadi M, Halilovic E, Zubrowski M, et al. Relief of profound feedback inhibition of mitogenic signaling by RAF inhibitors attenuates their activity in BRAFV600E melanomas. *Cancer Cell*. 2012;22(5):668–682.

[68] Gerosa L, Chidley C, Fröhlich F, Sanchez G, Lim SK, Muhlich J, et al. Receptor-driven ERK pulses reconfigure MAPK signaling and enable persistence of drug-adapted BRAF-mutant melanoma cells. *Cell Systems*. 2020;11(5):478–494.

[69] Hoek KS, Eichhoff OM, Schlegel NC, Döbbeling U, Kobert N, Schaerer L, et al. In vivo switching of human melanoma cells between proliferative and invasive states. *Cancer Research*. 2008;68(3):650–656.

[70] Zipser MC, Eichhoff OM, Widmer DS, Schlegel NC, Schoenewolf NL, Stuart D, et al. A proliferative melanoma cell phenotype is responsive to RAF/MEK inhibition independent of BRAF mutation status. *Pigment Cell & Melanoma Research*. 2011;24(2):326–333.

[71] Müller J, Krijgsman O, Tsoi J, Robert L, Hugo W, Song C, et al. Low MITF/AXL ratio predicts early resistance to multiple targeted drugs in melanoma. *Nature Communications*. 2014;5(1):1–15.

[72] Anastas JN, Kulikauskas RM, Tamir T, Rizos H, Long GV, Von Euw EM, et al. WNT5A enhances resistance of melanoma cells to targeted BRAF inhibitors. *The Journal of Clinical Investigation*. 2014;124(7):2877–2890.

[73] Verfaillie A, Imrichova H, Atak ZK, Dewaele M, Rambow F, Hulselmans G, et al. Decoding the regulatory landscape of melanoma reveals TEADS as regulators of the invasive cell state. *Nature Communications*. 2015;6(1):1–16.

[74] Rambow F, Marine JC, Goding CR. Melanoma plasticity and phenotypic diversity: therapeutic barriers and opportunities. *Genes & Development*. 2019;33(19-20):1295–1318.

[75] Smalley I, Kim E, Li J, Spence P, Wyatt CJ, Eroglu Z, et al. Leveraging transcriptional dynamics to improve BRAF inhibitor responses in melanoma. *EBioMedicine*. 2019;48:178–190.

[76] Arozarena I, Wellbrock C. Phenotype plasticity as enabler of melanoma progression and therapy resistance. *Nature Reviews Cancer*. 2019;19(7):377–391.

[77] Boumahdi S, de Sauvage FJ. The great escape: tumour cell plasticity in resistance to targeted therapy. *Nature Reviews Drug discovery*. 2020;19(1):39–56.

[78] Frederick BA, Helfrich BA, Coldren CD, Zheng D, Chan D, Bunn PA, et al. Epithelial to mesenchymal transition predicts gefitinib resistance in cell lines of head and neck squamous cell carcinoma and non–small cell lung carcinoma. *Molecular Cancer Therapeutics*. 2007;6(6):1683–1691.

[79] Zhang Z, Lee JC, Lin L, Olivas V, Au V, LaFramboise T, et al. Activation of the AXL kinase causes resistance to EGFR-targeted therapy in lung cancer. *Nature Genetics*. 2012;44(8):852–860.

[80] Oliveras-Ferraros C, Corominas-Faja B, Cufí S, Vazquez-Martin A, Martin-Castillo B, Iglesias JM, et al. Epithelial-to-mesenchymal transition (EMT) confers primary resistance to trastuzumab (Herceptin). *Cell Cycle*. 2012;11(21):4020–4032.

[81] Eichhoff OM, Weeraratna A, Zipser MC, Denat L, Widmer DS, Xu M, et al. Differential LEF1 and TCF4 expression is involved in melanoma cell phenotype switching. *Pigment Cell & Melanoma Research*. 2011;24(4):631–642.

[82] Hugo W, Shi H, Sun L, Piva M, Song C, Kong X, et al. Non-genomic and immune evolution of melanoma acquiring MAPKi resistance. *Cell*. 2015;162(6):1271–1285.

[83] Biechele TL, Kulikauskas RM, Toroni RA, Lucero OM, Swift RD, James RG, et al. Wnt/β-catenin signaling and AXIN1 regulate apoptosis triggered by inhibition of the mutant kinase BRAFV600E in human melanoma. *Science Signaling*. 2012;5(206):ra3–ra3.

[84] Conrad WH, Swift RD, Biechele TL, Kulikauskas RM, Moon RT, Chien AJ. Regulating the response to targeted MEK inhibition in melanoma: enhancing apoptosis in NRAS-and BRAF-mutant melanoma cells with Wnt/β-catenin activation. *Cell Cycle*. 2012;11(20):3724–3730.

[85] Connacher MK, Tay JW, Ahn NG. Rear-polarized Wnt5a-receptor-actin-myosin-polarity (WRAMP) structures promote the speed and persistence of directional cell migration. *Molecular Biology of the Cell*. 2017;28(14):1924–1936.

[86] Das Thakur M, Salangsang F, Landman AS, Sellers WR, Pryer NK, Levesque MP, et al. Modelling vemurafenib resistance in melanoma reveals a strategy to forestall drug resistance. *Nature*. 2013;494(7436):251–255.

[87] Kong X, Kuilman T, Shahrabi A, Boshuizen J, Kemper K, Song JY, et al. Cancer drug addiction is relayed by an ERK2-dependent phenotype switch. *Nature*. 2017;550(7675):270–274.

[88] Hong A, Moriceau G, Sun L, Lomeli S, Piva M, Damoiseaux R, et al. Exploiting drug addiction mechanisms to select against MAPKi-resistant melanoma. *Cancer Discovery*. 2018;8(1):74–93.

[89] Leung GP, Feng T, Sigoillot FD, Geyer FC, Shirley MD, Ruddy DA, et al. Hyperactivation of MAPK signaling is deleterious to RAS/RAF-mutant melanoma. *Molecular Cancer Research*. 2019;17(1):199–211.

[90] Algazi AP, Othus M, Daud AI, Lo RS, Mehnert JM, Truong TG, et al. Continuous versus intermittent BRAF and MEK inhibition in patients with BRAF-mutated melanoma: A randomized phase 2 trial. *Nature Medicine*. 2020;26(10):1564–1568.

[91] Dooley AJ, Gupta A, Bhattacharyya M, Middleton MR. Intermittent dosing with vemurafenib in BRAF V600E-mutant melanoma: review of a case series. *Therapeutic Advances in Medical Oncology*. 2014;6(6):262–266.

[92] Schreuer M, Jansen Y, Planken S, Chevolet I, Seremet T, Kruse V, et al. Combination of dabrafenib plus trametinib for BRAF and MEK inhibitor pretreated patients with advanced BRAFV600-mutant melanoma: an open-label, single arm, dual-centre, phase 2 clinical trial. *The Lancet Oncology*. 2017;18(4):464–472.

[93] Valpione S, Carlino MS, Mangana J, Mooradian MJ, McArthur G, Schadendorf D, et al. Rechallenge with BRAF-directed treatment in metastatic melanoma: a multi-institutional retrospective study. *European Journal of Cancer*. 2018;91:116–124.

[94] Tietze JK, Forschner A, Loquai C, Mitzel-Rink H, Zimmer L, Meiss F, et al. The efficacy of rechallenge with BRAF inhibitors after previous progression to BRAF inhibitors in melanoma: a retrospective multicenter study. *Oncotarget*. 2018;9(76):34336.

[95] Stagno A, Vari S, Annovazzi A, Anelli V, Russillo M, Cognetti F, et al. Case Report: Rechallenge With BRAF and MEK Inhibitors in Metastatic Melanoma: A Further Therapeutic Option in Salvage Setting? *Frontiers in Oncology*. 2021;11.

[96] Matter AV, Micaletto S, Urner-Bloch U, Dummer R, Goldinger SM. Long-Term Response to Intermittent Binimetinib in Patients with NRAS-Mutant Melanoma. *The Oncologist*. 2020;25(11):e1593.

[97] Holderfield M, Deuker MM, McCormick F, McMahon M. Targeting RAF kinases for cancer therapy: BRAF-mutated melanoma and beyond. *Nature Reviews Cancer*. 2014;14(7):455–467.

[98] Giugliano F, Crimini E, Tarantino P, Zagami P, Uliano J, Corti C, et al. First line treatment of BRAF mutated advanced melanoma: does one size fit all? *Cancer Treatment Reviews*. 2021;p. 102253.

[99] Dummer R, Ascierto PA, Gogas HJ, Arance A, Mandala M, Liszkay G, et al. Encorafenib plus binimetinib versus vemurafenib or encorafenib in patients with BRAF-mutant melanoma (COLUMBUS): a multicentre, open-label, randomised phase 3 trial. *The Lancet Oncology*. 2018;19(5):603–615.

[100] Halle BR, Johnson DB. Defining and Targeting BRAF Mutations in Solid Tumors. *Current Treatment Options in Oncology*. 2021;22(4):1–15.

[101] Tangella LP, Clark ME, Gray ES. Resistance mechanisms to targeted therapy in BRAF-mutant melanoma-A mini review. *Biochimica et Biophysica Acta (BBA)-General Subjects*. 2020;p. 129736.

[102] Proietti I, Skroza N, Bernardini N, Tolino E, Balduzzi V, Marchesiello A, et al. Mechanisms of acquired braf inhibitor resistance in melanoma: A systematic review. *Cancers*. 2020;12(10):2801.

[103] Prahallad A, Sun C, Huang S, Di Nicolantonio F, Salazar R, Zecchin D, et al. Unresponsiveness of colon cancer to BRAF (V600E) inhibition through feedback activation of EGFR. *Nature*. 2012;483(7387):100–103.

[104] Wagle N, Emery C, Berger MF, Davis MJ, Sawyer A, Pochanard P, et al. Dissecting therapeutic resistance to RAF inhibition in melanoma by tumor genomic profiling. *Journal of Clinical Oncology*. 2011;29(22):3085. This has the picture everyone uses for vemurafenib response.

[105] Corcoran RB, Dias-Santagata D, Bergethon K, Iafrate AJ, Settleman J, Engelman JA. BRAF gene amplification can promote acquired resistance to MEK inhibitors in cancer cells harboring the BRAF V600E mutation. *Science Signaling*. 2010;3(149):ra84–ra84.

[106] Rambow F, Rogiers A, Marin-Bejar O, Aibar S, Femel J, Dewaele M, et al. Toward minimal residual disease-directed therapy in melanoma. *Cell*. 2018;174(4):843–855.

[107] Su Y, Wei W, Robert L, Xue M, Tsoi J, Garcia-Diaz A, et al. Single-cell analysis resolves the cell state transition and signaling dynamics associated with melanoma drug-induced resistance. *Proceedings of the National Academy of Sciences USA*. 2017;114(52):13679–13684.

[108] Shaffer SM, Dunagin MC, Torborg SR, Torre EA, Emert B, Krepler C, et al. Rare cell variability and drug-induced reprogramming as a mode of cancer drug resistance. *Nature*. 2017;546(7658):431–435.

[109] Widmer DS, Cheng PF, Eichhoff OM, Belloni BC, Zipser MC, Schlegel NC, et al. Systematic classification of melanoma cells by phenotype-specific gene expression mapping. *Pigment cell & Melanoma Research*. 2012;25(3):343–353.

[110] Song C, Piva M, Sun L, Hong A, Moriceau G, Kong X, et al. Recurrent tumor cell–intrinsic and–extrinsic alterations during MAPKi-induced melanoma regression and early adaptation. *Cancer Discovery*. 2017;7(11):1248–1265.

[111] Fallahi-Sichani M, Becker V, Izar B, Baker GJ, Lin JR, Boswell SA, et al. Adaptive resistance of melanoma cells to RAF inhibition via reversible induction of a slowly dividing de-differentiated state. *Molecular Systems Biology*. 2017;13(1):905.

[112] Ramsdale R, Jorissen RN, Li FZ, Al-Obaidi S, Ward T, Sheppard KE, et al. The transcription cofactor c-JUN mediates phenotype switching and BRAF inhibitor resistance in melanoma. *Science Signaling*. 2015;8(390):ra82–ra82.

[113] Tétu P, Vercellino L, de Moura CR, Baroudjian B, Dumaz N, Mourah S, et al. Mitogen-activated protein kinase blockade in melanoma: intermittent versus continuous therapy, from preclinical to clinical data. *Current Opinion in Oncology*. 2021;33(2):127–132.

[114] Xue Y, Martelotto L, Baslan T, Vides A, Solomon M, Mai TT, et al. An approach to suppress the evolution of resistance in BRAF V600E-mutant cancer. *Nature Medicine*. 2017;23(8):929–937.

[115] Moriceau G, Hugo W, Hong A, Shi H, Kong X, Clarissa CY, et al. Tunable-combinatorial mechanisms of acquired resistance limit the efficacy of BRAF/MEK cotargeting but result in melanoma drug addiction. *Cancer Cell*. 2015;27(2):240–256.

[116] Sun C, Wang L, Huang S, Heynen GJ, Prahallad A, Robert C, et al. Reversible and adaptive resistance to BRAF (V600E) inhibition in melanoma. *Nature*. 2014;508(7494):118–122.

[117] de Moura CR, Vercellino L, Jouenne F, Baroudjian B, Sadoux A, Louveau B, et al. Intermittent versus continuous dosing of MAPK inhibitors in the treatment of BRAF-mutated melanoma. *Translational Oncology*. 2020;13(2):275–286.

[118] Sanchez IM, Purwin TJ, Chervoneva I, Erkes DA, Nguyen MQ, Davies MA, et al. In vivo ERK1/2 reporter predictively models response and resistance to combined BRAF and MEK inhibitors in melanoma. *Molecular Cancer Therapeutics*. 2019;18(9):1637–1648.

[119] Subramanian A, Tamayo P, Mootha VK, Mukherjee S, Ebert BL, Gillette MA, et al. Gene set enrichment analysis: a knowledge-based approach for interpreting genome-wide expression profiles. *Proceedings of the National Academy of Sciences USA*. 2005;102(43):15545–15550.

[120] Mootha VK, Lindgren CM, Eriksson KF, Subramanian A, Sihag S, Lehar J, et al. PGC-1α-responsive genes involved in oxidative phosphorylation are coordinately downregulated in human diabetes. *Nature Genetics*. 2003 Jul;34(3):267–273.

[121] Barretina J, Caponigro G, Stransky N, Venkatesan K, Margolin AA, Kim S, et al. The Cancer Cell Line Encyclopedia enables predictive modelling of anticancer drug sensitivity. *Nature*. 2012;483(7391):603–607.

[122] Sachindra LL, Novak D, Wu H, Hüser L, Granados K, Orouji E, et al. New role of ID3 in melanoma adaptive drug-resistance. *Oncotarget*. 2017;8(66):110166.

[123] Lake D, Corrêa SA, Müller J. Negative feedback regulation of the ERK1/2 MAPK pathway. *Cellular and Molecular Life Sciences*. 2016;73(23):4397–4413.

[124] Metzner T, Bedeir A, Held G, Peter-Vörösmarty B, Ghassemi S, Heinzle C, et al. Fibroblast growth factor receptors as therapeutic targets in human melanoma: synergism with BRAF inhibition. *Journal of Investigative Dermatology*. 2011;131(10):2087–2095.

[125] Straussman R, Morikawa T, Shee K, Barzily-Rokni M, Qian ZR, Du J, et al. Tumour micro-environment elicits innate resistance to RAF inhibitors through HGF secretion. *Nature*. 2012;487(7408):500–504.

[126] Ng YK, Lee JY, Supko KM, Khan A, Torres SM, Berwick M, et al. Pan-erbB inhibition potentiates BRAF inhibitors for melanoma treatment. *Melanoma Research*. 2014;24(3):207.

[127] Young HL, Rowling EJ, Bugatti M, Giurisato E, Luheshi N, Arozarena I, et al. An adaptive signaling network in melanoma inflammatory niches confers tolerance to MAPK signaling inhibition. *Journal of Experimental Medicine*. 2017;214(6):1691–1710.

[128] Yu L, Favoino E, Wang Y, Ma Y, Deng X, Wang X. The CSPG4-specific monoclonal antibody enhances and prolongs the effects of the BRAF inhibitor in melanoma cells. *Immunologic Research*. 2011;50(2-3):294–302.

[129] Caramel J, Papadogeorgakis E, Hill L, Browne GJ, Richard G, Wierinckx A, et al. A switch in the expression of embryonic EMT-inducers drives the development of malignant melanoma. *Cancer Cell*. 2013;24(4):466–480.

[130] Konieczkowski DJ, Johannessen CM, Abudayyeh O, Kim JW, Cooper ZA, Piris A, et al. A melanoma cell state distinction influences sensitivity to MAPK pathway inhibitors. *Cancer Discovery*. 2014;4(7):816–827.

[131] Ernst AK, Putscher A, Samatov TR, Suling A, Galatenko VV, Shkurnikov MY, et al. Knock-down of L1CAM significantly reduces metastasis in a xenograft model of human melanoma: L1CAM is a potential target for anti-melanoma therapy. *PloS One*. 2018;13(2):e0192525.

[132] Kiefel H, Bondong S, Pfeifer M, Schirmer U, Erbe-Hoffmann N, Schäfer H, et al. EMT-associated up-regulation of L1CAM provides insights into L1CAM-mediated integrin signalling and NF-κB activation. *Carcinogenesis*. 2012;33(10):1919–1929.

[133] Delord JP, Robert C, Nyakas M, McArthur GA, Kudchakar R, Mahipal A, et al. Phase I dose-escalation and-expansion study of the BRAF inhibitor encorafenib (LGX818) in metastatic BRAF-mutant melanoma. *Clinical Cancer Research*. 2017;23(18):5339–5348.

[134] Grippo J, Zhang W, Heinzmann D, Yang K, Wong J, Joe A, et al. A phase I, randomized, open-label study of the multiple-dose pharmacokinetics of vemurafenib in patients with BRAF V600E mutation-positive metastatic melanoma. *Cancer Chemotherapy and Pharmacology*. 2014;73(1):103–111.

[135] Silva AS, Kam Y, Khin ZP, Minton SE, Gillies RJ, Gatenby RA. Evolutionary approaches to prolong progression-free survival in breast cancer. *Cancer Research*. 2012;72(24):6362–6370.

[136] Zhang J, Cunningham JJ, Brown JS, Gatenby RA. Integrating evolutionary dynamics into treatment of metastatic castrate-resistant prostate cancer. *Nature Communications*. 2017;8(1):1–9.

[137] Park DS, Luddy KA, Robertson-Tessi M, O'Farrelly C, Gatenby RA, Anderson AR. Searching for Goldilocks: How evolution and ecology can help uncover more effective patient-specific chemotherapies. *Cancer Research*. 2020;80(23):5147–5154.

[138] West J, You L, Zhang J, Gatenby RA, Brown JS, Newton PK, et al. Towards multidrug adaptive therapy. *Cancer Research*. 2020;80(7):1578–1589.

[139] Woodworth MB, Girskis KM, Walsh CA. Building a lineage from single cells: genetic techniques for cell lineage tracking. *Nature Reviews Genetics*. 2017;18(4):230.

[140] McKenna A, Gagnon JA. Recording development with single cell dynamic lineage tracing. *Development*. 2019;146(12):dev169730.

[141] Pastushenko I, Blanpain C. EMT transition states during tumor progression and metastasis. *Trends in Cell Biology*. 2018;.

[142] Muranen T, Selfors LM, Worster DT, Iwanicki MP, Song L, Morales FC, et al. Inhibition of PI3K/mTOR leads to adaptive resistance in matrix-attached cancer cells. *Cancer Cell*. 2012;21(2):227–239.

[143] Michiels S, Koscielny S, Hill C. Prediction of cancer outcome with microarrays: a multiple random validation strategy. *The Lancet*. 2005;365(9458):488–492.

[144] Button KS, Ioannidis JP, Mokrysz C, Nosek BA, Flint J, Robinson ES, et al. Power failure: why small sample size undermines the reliability of neuroscience. *Nature Reviews Neuroscience*. 2013;14(5):365.

[145] Barbie DA, Tamayo P, Boehm JS, Kim SY, Moody SE, Dunn IF, et al. Systematic RNA interference reveals that oncogenic KRAS-driven cancers require TBK1. *Nature*. 2009;462(7269):108.

[146] Ronan T, Qi Z, Naegle KM. Avoiding common pitfalls when clustering biological data. *Science Signaling*. 2016;9(432):re6–re6.

[147] Sørlie T, Perou CM, Tibshirani R, Aas T, Geisler S, Johnsen H, et al. Gene expression patterns of breast carcinomas distinguish tumor subclasses with clinical implications. *Proceedings of the National Academy of Sciences USA*. 2001;98(19):10869–10874.

[148] Gupta A, Wang H, Ganapathiraju M. Learning structure in gene expression data using deep architectures, with an application to gene clustering. In: Bioinformatics and Biomedicine (BIBM), 2015 IEEE International Conference on. IEEE; 2015. p. 1328–1335.

[149] Tan J, Ung M, Cheng C, Greene CS. Unsupervised feature construction and knowledge extraction from genome-wide assays of breast cancer with denoising autoencoders. In: Pacific Symposium on Biocomputing; 2015. p. 132–143.

[150] Ronen J, Akalin A. netSmooth: Network-smoothing based imputation for single cell RNA-seq. *F1000Research*. 2018;7.

[151] Dørum G, Snipen L, Solheim M, Saebo S. Smoothing gene expression data with network information improves consistency of regulated genes. *Statistical Applications in Genetics and Molecular Biology*. 2011;10(1).

[152] Newman MEJ. Mixing patterns in networks. *Physical Review E*. 2003;67(2):026126.

[153] Ideker T, Ozier O, Schwikowski B, Siegel AF. Discovering regulatory and signalling circuits in molecular interaction networks. *Bioinformatics*. 2002;18(suppl_1):S233–S240.

[154] Goncalves A, Leigh-Brown S, Thybert D, Stefflova K, Turro E, Flicek P, et al. Extensive compensatory cis-trans regulation in the evolution of mouse gene expression. *Genome Research*. 2012;22(12):2376–2384.

[155] Bauer PM, Fulton D, Bo YC, Sorescu GP, Kemp BE, Jo H, et al. Compensatory phosphorylation and protein-protein interactions revealed by loss of function and gain of function mutants of multiple serine phosphorylation sites in endothelial nitric-oxide synthase. *The Journal of Biological Chemistry*. 2003;278(17):14841–14849.

[156] Peel L, Delvenne JC, Lambiotte R. Multiscale mixing patterns in networks. *Proceedings of the National Academy of Sciences USA*. 2018;115(16):4057–4062.

[157] Rudolph JD, de Graauw M, van de Water B, Geiger T, Sharan R. Elucidation of signaling pathways from large-scale phosphoproteomic data using protein interaction networks. *Cell Systems*. 2016;3(6):585–593.

[158] Mansourpour M, Rajabi M, Blais J. Effects and performance of speckle noise reduction filters on active radar and SAR images. In: Proc. ISPRS. vol. 36; 2006. p. W41.

[159] Aiello W, Chung F, Lu L. A random graph model for power law graphs. *Experimental Mathematics*. 2001;10(1):53–66.

[160] Chung F, Lu L. Connected components in random graphs with given expected degree sequences. *Annals of Combinatorics*. 2002;6:125–145.

[161] Alam M, Khan M, Vullikanti A, Marathe M. An efficient and scalable algorithmic method for generating large-scale random graphs. In: SC'16: Proceedings of the International Conference for High Performance Computing, Networking, Storage and Analysis. IEEE; 2016. p. 372–383.

[162] Middendorf M, Ziv E, Wiggins CH. Inferring network mechanisms: the Drosophila melanogaster protein interaction network. *Proceedings of the National Academy of Sciences USA*. 2005;102(9):3192–3197.

[163] Karrer B, Newman MEJ. Stochastic blockmodels and community structure in networks. *Physical Review E*. 2011;83(1):016107.

[164] Newman MEJ, Clauset A. Structure and inference in annotated networks. *Nature Communications*. 2016;7:11863.

[165] Ng A, Jordan M, Weiss Y. On spectral clustering: Analysis and an algorithm. *Advances in Neural Information Processing Systems*. 2001;14:849–856.

[166] Blondel VD, Guillaume JL, Lambiotte R, Lefebvre E. Fast unfolding of communities in large networks. *Journal of Statistical Mechanics: Theory and Experiment*. 2008;2008(10):P10008.

[167] Jeh G, Widom J. Scaling personalized web search. In: Proceedings of the 12th International Conference on World Wide Web. Acm; 2003. p. 271–279.

[168] Uhlén M, Fagerberg L, Hallström BM, Lindskog C, Oksvold P, Mardinoglu A, et al. Tissue-based map of the human proteome. *Science*. 2015;347(6220):1260419.

[169] Das J, Yu H. HINT: High-quality protein interactomes and their applications in understanding human disease. *BMC Systems Biology*. 2012;6(1):92.

[170] Ghasemian A, Hosseinmardi H, Clauset A. Evaluating Overfit and Underfit in Models of Network Community Structure. *IEEE Transactions on Knowledge and Data Engineering*. 2019;32(9):1722–1735.

[171] Hart GT, Ramani AK, Marcotte EM. How complete are current yeast and human protein-interaction networks? *Genome Biology*. 2006;7(11):120.

[172] Campbell JD, Mazzilli SA, Reid ME, Dhillon SS, Platero S, Beane J, et al. The case for a pre-cancer genome atlas (PCGA). *Cancer Prevention Research*. 2016;9(2):119–124.

[173] Spira A, Yurgelun MB, Alexandrov L, Rao A, Bejar R, Polyak K, et al. Precancer atlas to drive precision prevention trials. *Cancer Research*. 2017;77(7):1510–1541.

[174] Vyberg M, Nielsen S. Proficiency testing in immunohistochemistry—experiences from Nordic Immunohistochemical Quality Control (NordiQC). *Virchows Archiv*. 2016 Jan;468(1):19–29.

[175] Motwani MC, Gadiya MC, Motwani RC, Harris FC. Survey of image denoising techniques. In: Proceedings of GSPX; 2004. p. 27–30.

[176] Agostinelli F, Anderson MR, Lee H. Adaptive multi-column deep neural networks with application to robust image denoising. In: Advances in Neural Information Processing Systems; 2013. p. 1493–1501.

[177] Öktem R, Egiazarian K, Lukin VV, Ponomarenko NN, Tsymbal OV. Locally adaptive DCT filtering for signal-dependent noise removal. *EURASIP Journal on Advances in Signal Processing*. 2007;2007(1):042472.

[178] Deng G, Cahill L. An adaptive Gaussian filter for noise reduction and edge detection. In: 1993 IEEE Conference Record Nuclear Science Symposium and Medical Imaging Conference. IEEE; 1993. p. 1615–1619.

[179] Peel L, Larremore DB, Clauset A. The ground truth about metadata and community detection in networks. *Science Advances*. 2017;3(5):e1602548.

[180] Fortunato S. Community detection in graphs. *Physics Reports*. 2010;486(3-5):75–174.

[181] Newman MEJ. The structure and function of complex networks. *SIAM Review*. 2003;45(2):167–256.

[182] Shaw PJ, Rawlins DJ. The point-spread function of a confocal microscope: its measurement and use in deconvolution of 3-D data. *Journal of Microscopy*. 1991;163(2):151–165.

[183] Braschi B, Denny P, Gray K, Jones T, Seal R, Tweedie S, et al. Genenames.org: the HGNC and VGNC resources in 2019. *Nucleic Acids Research*. 2018;47(D1):D786–D792.

[184] Marioni JC, Mason CE, Mane SM, Stephens M, Gilad Y. RNA-seq: an assessment of technical reproducibility and comparison with gene expression arrays. *Genome Research*. 2008;18(9):1509–1517.

[185] Eliuk S, Makarov A. Evolution of Orbitrap Mass Spectrometry Instrumentation. *Annual Review of Analytical Chemistry*. 2015;8:61—80.

Appendix A

Intermittent drug treatment of several melanoma cell lines

The focus of this appendix is on intermittent treatment of melanoma cell lines related to Chapter 2. These cell lines (WM1617, WM115, C32, A375, WM164) did not reproducibly show a better response to intermittent treatment compared to continuous treatment. While these many of these data show negative results and are not publication worthy, they should hopefully be a useful starting point for future research to identify the optimal conditions to see a beneficial intermittent treatment effect in melanoma cell lines besides WM239A. This work was largely done by myself with some experiments of WM1617 and PrestoBlue optimization done by former undergraduate Steven Sloan, and some experiments with A375 were done by former undergraduate Jason Haw.

A.1 WM1617 and WM1617-BRAF^{V600E}

In Chapter 2, we typically used WM239A cells that had a cumate inducible BRAF^{V600E} construct integrated in the genome. We found that this was important for WM239A cells to show a beneficial response to intemittent drug treatment compared to continuous treatment. Thus, I created another metastatic melanoma cell line WM1617 with the BRAF^{V600E} cumate inducible system. This already has a BRAF^{V600E} mutation, unlike WM239A cells, which are BRAF^{V600D}. I performed a dose response experiment with LGX818 for 72 hours to compare the level of resistance this oncogene induced (Fig. A.1). The untransfected ("parental") WM1617 cells and the non-induced WM1617-BRAF^{V600E} cells had very similar dose response curves (Fig. A.1A). There may be a slight right shift for the non-induced cells, indicating a slight leakiness to the vector. For

cells cumate induced for 72 hours before the dose response, they show about a 10-fold increase in the apparent IC_{50}. This indicates that the amplified $BRAF^{V600E}$ promoted the resistance to LGX818 in WM1617 cells. These dose response curves are normallized individually to make an easy comparison in drug sensitivity, but this transformation erases differences in growth rates between cell lines. Looking at an absolute scale shows that cumate induced WM1617-$BRAF^{V600E}$ cells have a loss of cell fitness at low concentrations of drug (Fig. A.1B). This likely indicates that the cells have hyperactive ERK and are "drug addicted". Also, at the drug concentration I use for growth curve experiments (500nM), there is very little difference in absolute cell numbers between all the cell lines.

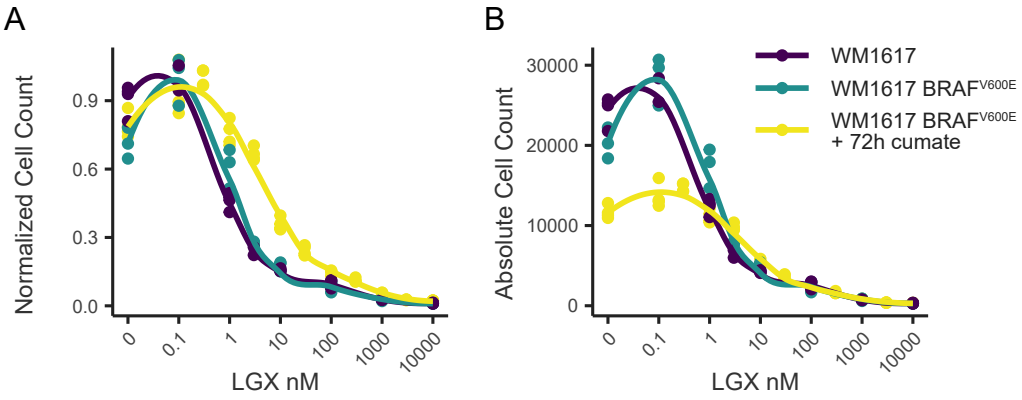

Figure A.1: WM1617 LGX818 Dose Responses. WM1617 cells were seeded in 96 well plates at 2500 cells per well after 72 h of cumate induction or not. Then the cells were treated with various concentrations of LGX818 for 72 h before CellTiter-Glo 2.0 viability assay. **A.** Each cell line is normalized to the mean highest viability LGX818 concentration. WM1617-$BRAF^{V600E}$ cells induced with cumate have about a 10-fold greater IC_{50}. **B.** The same data as in **A.** but shown on an absolute cell number scale. This shows that cumate induction reduces the proliferation rate of WM1617-$BRAF^{V600E}$ cells.

Next, I wanted to compare the response to continuous vs intermittent drug treatment in WM1617 untransfected and WM1617-$BRAF^{V600E}$ cells. To be consistent with the WM239A-$BRAF^{V600E}$ experiments in Chapter 2, I seeded 96 well plates at 500 or 750 cells per well, and treated cells with 500 nM LGX818. The intermittent treatment schedule was 7 days-on, 7-days off drug, and cell viability was measured at the end of each week with the CellTiter-Glo 2.0 assay.

The continuous drug treatment with 500 nM LGX818 suppressed growth throughout the four week experiment in all conditions (Figure A.2). The intermittently treated cells substantially outgrew during the first week off, and then were suppressed again by drug treatment. This suppression was short lived, as the cell numbers in week 4 were consistently higher than in week 2. There was no major qualitative difference in behavior between the WM1617 untransfected and WM1617-BRAF^{V600E} cell lines at either 500 cells or 750 cell initial seeding density.

From this experiment it seemed that the 500 nM LGX818 was too high. WM1617, either BRAF^{V600E} amplified or not, did not outgrow with continuous treatment. However, WM239A BRAF amplified cells start to significantly outgrow after two weeks of continuous treatment with 500 nM LGX818. This is probably because the BRAF amplification in WM1617 cells increased the IC_{50} by only 10-fold, whereas in WM239A cells it was close to 100-fold.

Next, we tried lower drug concentrations of LGX818 when treating WM1617 cells to see if that would show a beneficial response to intermittent drug treatment. Once again we compared WM1617 untransfected and 72 hr cumate-induced WM1617-BRAF^{V600E} cells in a continuous vs intermittent (7 d-on/7 d-off) drug treatment schedule. We see the same behavior with 500 nM LGX818, repeating the result that continuous treatment suppresses growth compared to intermittent treatment (Fig. A.3A). The growth curves are qualitatively the same with 30 nM LGX818 treatment. But with 3 nM LGX818, cells numbers were repressed at day 21 with intermittent treatment compared to continuous treatment. Still, there was signficant outgrowth of both intermittent and continuously treated cells. At week four, it appears that continuous had growth repression, but this is likely caused by cells overgrowing the well, which causes cells to detach from the plate. This was a promising result that suggested that intermittent treatment might suppress growth more than continuous treatment in another melanoma cell line. We also noted that the BRAF^{V600E} amplification did not have a major effect on how the WM1617 cell line responded in these growth curve experiments. Thus we continued with the WM1617 untransfected cell line for future experiments.

We wanted to see if the growth repression by intermittent treatment was reproducible in an

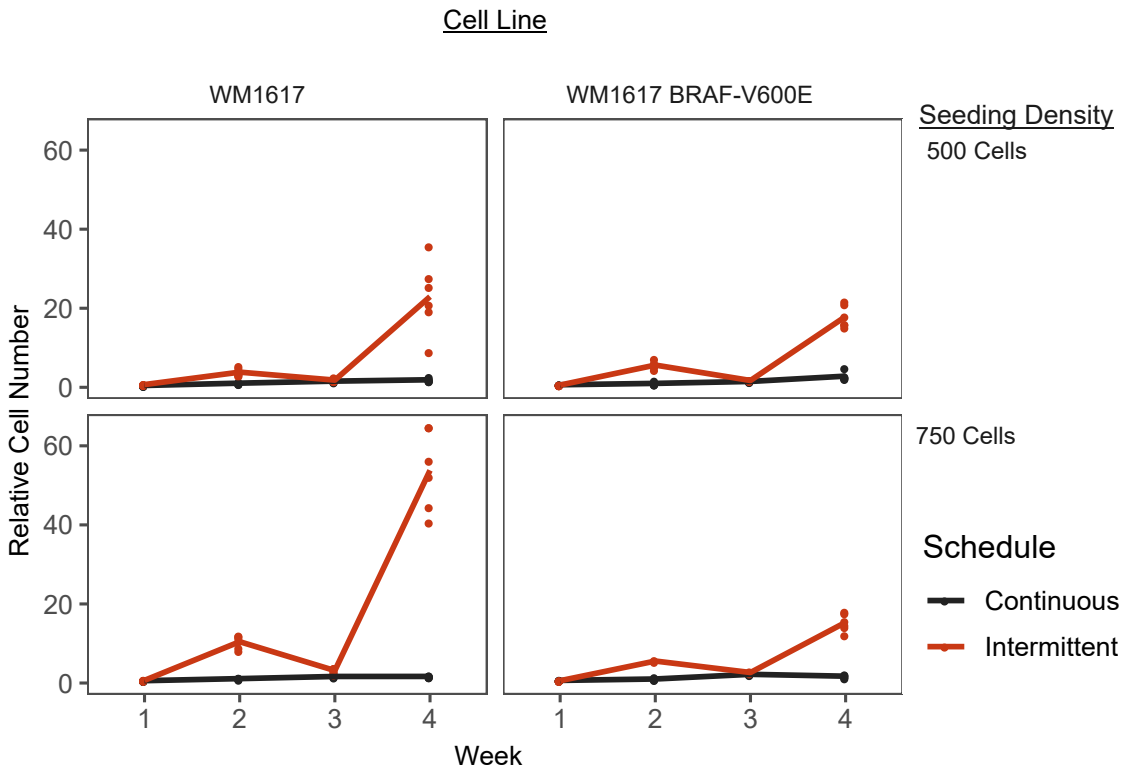

Figure A.2: Intermittent vs continuous treatment of WM1617 and WM1617-BRAF^{V600E} cells. WM1617 and WM1617-BRAF^{V600E} cells were seeded in 96 well plates at 500 or 750 cells per well after 72 h of cumate induction. Then the cells were treated continuously or intermittently with 500 nM LGX818. The intermittent schedule was 7 days on/7 days off. The intermittently treated cells outgrew the continuously treated cells in all conditions.

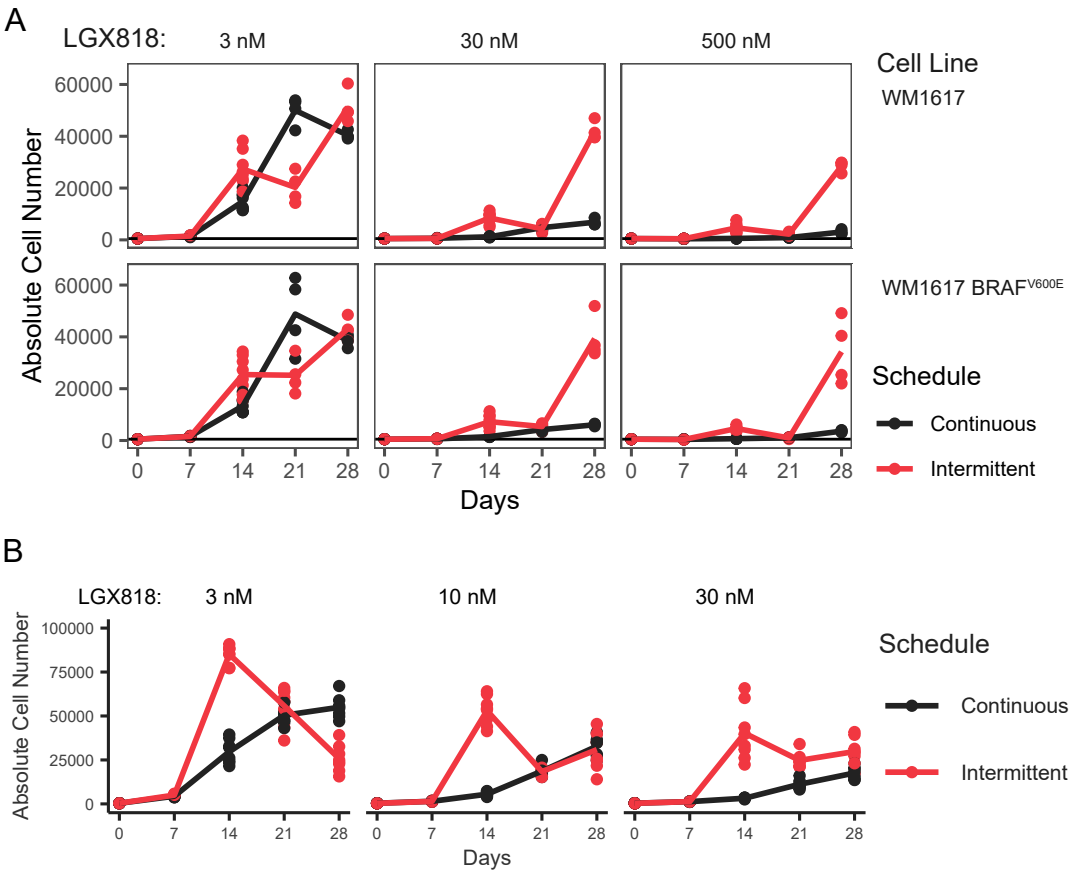

Figure A.3: Intermittent vs continuous treatment of WM1617 cells with different drug concentrations. **A.** WM1617 and WM1617-BRAF^{V600E} cells were seeded in 96 well plates at 500 cells per well after 72 h of cumate induction. Then the cells were treated continuously or intermittently with 3 nM, 30 nM, or 500 nM LGX818. The same as in **B.**, but the cells were WM1617 untransfected, and 3 nM, 10 nM, or 30 nM LGX818 was used. The intermittent schedule was 7 days on/7 days off for both panels.

independent experiment. Also, we wanted to see if an intermediate drug concentration between 3 nM and 30 nM could make the growth suppression of intermittent treatment bigger. Thus, we conducted a growth curve experiment in WM1617 untransfected cells with 3 nM, 10 nM, and 30 nM LGX818 with the same continuous and intermittent treatment schedules (Fig. A.3B). Unfortunately, the results did not match the last experiment. For cells treated with 3 nM drug, the intermittent cells significantly outgrew in the 7 days off drug during week 2 (day 14 time-point). They then outgrew the plate and started to come off the plate, which is the reason of the apparent decrease in cell numbers on days 21 and 28. Thus 3 nM intermittent treatment did not actually reduce cell numbers compared to continuous treatment in this experiment. The 10 nM showed outgrowth during week 2, but the cell numbers were repressed during week 3 with drug rechallenge. Then in week 4 the cells did not significantly out grow continuously treated cells. The 30 nM conditions showed a similar growth curve, but the intermittently treated cells had consistently higher cell numbers than continuously treated cells.

In many of these intermittent vs continuous treatment assays, the WM1617 cells significantly outgrew in the 7 days off drug treatment. This could mean that they don't experience lasting "drug addiction" during the week off. We thought that shortening the drug holiday would give the cells less time to grow out and potentially show reduced cell numbers compared to continuously treated cells.

To efficiently test a different treatment schedule, we used the PrestoBlue HS cell viability assay instead of the CellTiter Glo 2.0 assay. Unlike CellTiter Glo where cells are lysed during the assay, PrestoBlue allowed us to re-assay the same 96-well plate seven times across two weeks. This assay did not show toxicity in the cells, and had linear agreement with CellTiter Glo.

In this experiment, we tested continuous treatment with 3 nM or 10 nM LGX818 to intermittent (4 days on/3 days off). Cells were assayed with the PrestoBlue every 2-3 days for 16 days. Across the first drug-on drug-off cycle, there was essentially no difference between continuous vs intermittent for 3 nM or 10 nM. Then in the second cycle, the 3 nM intermittently treated cells outgrew the continuously treated cells. Unexpectedly, the intermittently treated cells increased

with cell numbers despite drug re-addition through days 9 and 11. In previous experiments with an intermittent drug treatment of 7 days on/7 days off, cells typically died upon drug re-addition. The intermittent and continuous schedules had comparable cell numbers up to day 11, but then the intermittently treated cells grew out faster than continuous treatment.

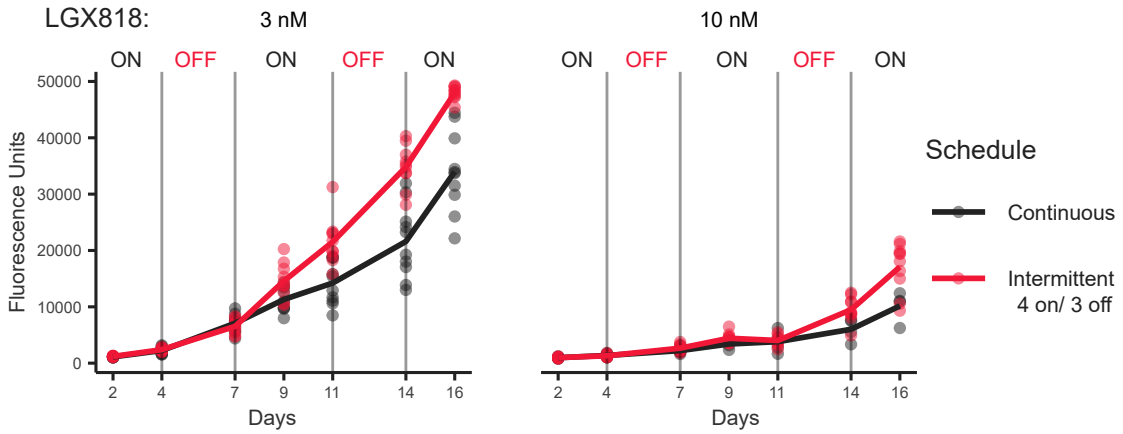

Figure A.4: 4 days on/3 days off intermittent schedule vs continuous treatment in WM1617 with PrestoBlue. WM1617 cells were seeded in 96 well plates at 500 cells per well. Then the cells were treated continuously or intermittently with 3 nM or 10 nM LGX818. The intermittent schedule was 4 days on drug/3 days off drug. The same wells were repeatedly assayed for cell viability using the PrestoBlue HS assay.

Overall, intermittent drug treatment did not reliably reduce cell fitness compared to continuous treatment in WM1617 cells. While one experiment showed that intermittent treatment may potentially reduce cell numbers compared to continuous treatment, it was not reproducible in a follow-up experiment. In experiments with a 7-on/7-off intermittent schedule, the cells grew out significantly during the drug holidays. In the 4-on/3-off experiment, the cells gradually grew out faster than continuous and it was delayed by a higher drug concentration. Interestingly, there was no major difference in growth curves for WM1617 untransfected and WM1617-BRAF^{V600E} cells.

There are multiple avenues of future work that could still be done with WM1617 cells where they may show a benefit from intermittent drug treatment. The WM1617-BRAF^{V600E} cells I created showed 10-fold greater IC_{50} to LGX818 compared to uninduced and untransfected WM1617. They

also had a slower proliferation rate which we attribute to the detrimental effects of hyperactive ERK signaling. However, WM239A-BRAF^{V600E} cells I used in Chapter 2 were much more strongly resistant than their untransfected parental cell line. Perhaps this much stronger induction of drug resistance is important to see a beneficial response to intermittent treatment. The WM1617-BRAF^{V600E} were always induced with 30 μg /ml cumate for 72 hours before seeding the experiments in this appendix. While this concentration and timepoint showed strong BRAF^{V600E} induction in WM239A cells, it might not have been as strong in WM1617-BRAF^{V600E} cells.

A.2 WM115

We also tested the WM115 melanoma cell line. These were derived from the same patient as WM239A, but they are from a primary site as opposed to a lymph node metastasis. As an initial test of this cell line, we grew the cells under several concentrations of LGX818, measuring the cell viability by PrestoBlue. This assay allowed us to assay the same plate every 2-3 days without killing the cells. The intermittent schedule was determined in real-time based on if the cells were growing out during the drug holiday. The schedule ended up being 13 days on/4 days off/6 days on/6 days off.

Cell under the lower LGX818 concentrations (0.05 nM, 0.5 nM) grew out over the 29 day experiment (Fig. A.5). The cells treated with 5, 50, 500 nM concentrations did not grow out. After the initial 13 days on, the cell numbers were increasing in the 5 nM and 50 nM conditions which triggered our decision to switch to a drug holiday for 4 days. There was not much change in the cell numbers during this holiday. Then the 5 nM and 50 nM conditions showed major loss of cells that was not recovered upon a second drug holiday. The cells treated with 500 nM saw major cell loss within the first few days and never recovered.

Based on the apparent resenstization upon drug holidays for cells treated with 5 nM and 50 nM, we repeated this experiment to test if intermittent treatment would suppress cell numbers compared to continuous treatment. We changed the intermittent schedule to be 10 days on/4 days off/7 days on. We thought the shorter initial drug treatment might be better to see a beneficial

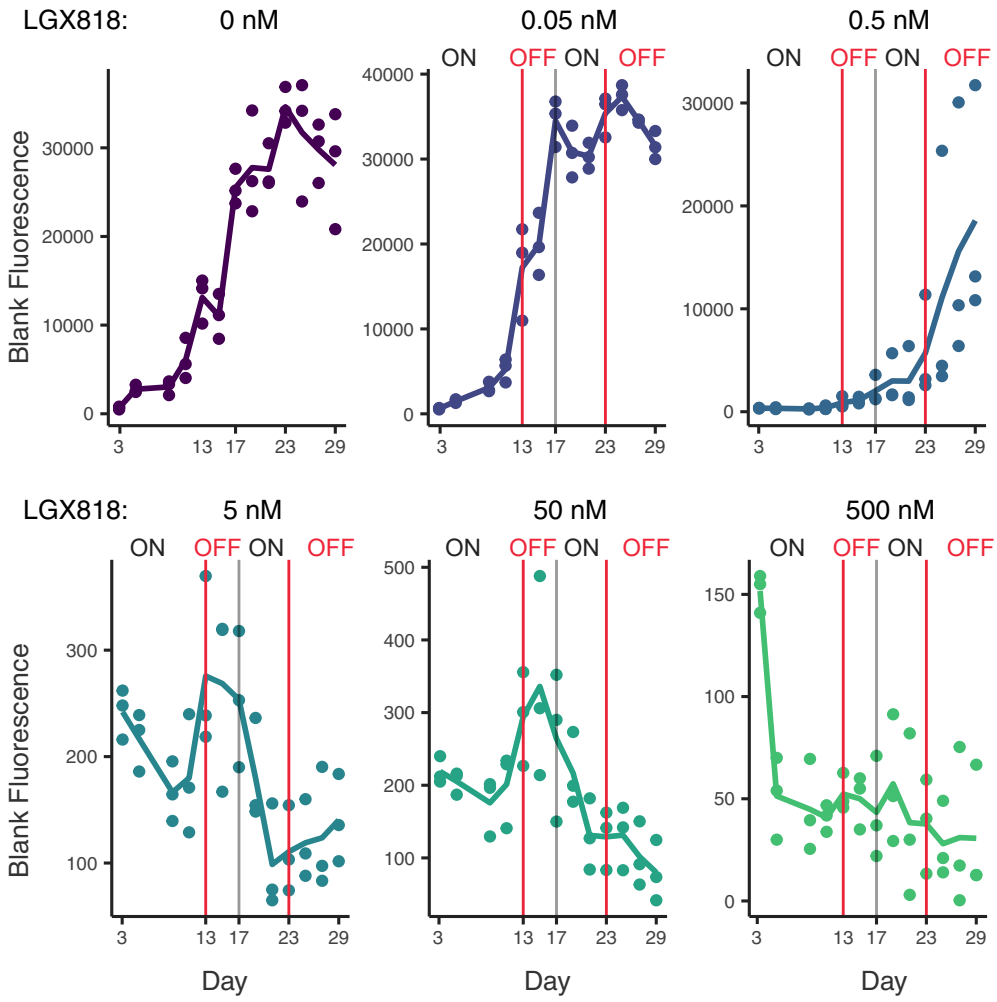

Figure A.5: WM115 Intermittent LGX818 treatment. WM115 cells were treated intermittented with various concentrations of LGX818, and cell viability was measured repeatedly using Presto-Blue. Cells treated with 5 nM and 50 nM showed promise for a beneficial intermittent treatment response.

intermittent effect compared to continuous treatment. During the drug holiday, the cell numbers significantly expanded, but showed sensitivity upon drug rechallenge (Fig. A.6). Surprisingly, the continuously treated WM115 cells did not grow out. There might have been a slight outgrowth between day 7 and 10, but the cell numbers further declined for the 21 day experiment. On day 21 there was no difference between the intermittent and continuous treatment.

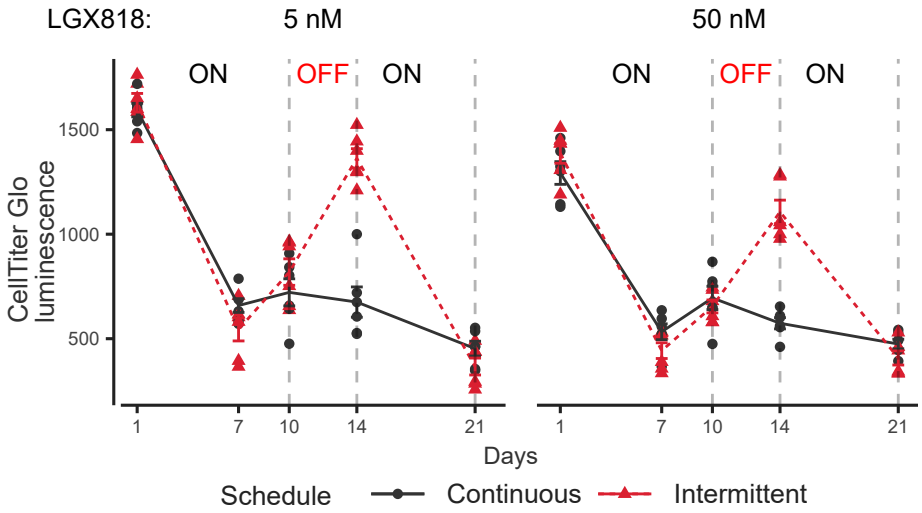

Figure A.6: WM115 Continuous vs. Intermittent LGX818 treatment. WM115 cells were treated either continuously or intermittently, and cell viability was measured using the CellTiter-Glo 2.0 assay. Neither 5 nM nor 50 nM showed lower cell numbers with intermittent treatment than continuous treatment, but the cell numbers were roughly the same on the last time point.

We have not done any follow up experiments with WM115 cells. While it is promising that the cells numbers decrease upon rechallenge, the continuously treated cells never grew out in this timeframe. One potential future direction is to increase the length of the experiment to see if continuously treated cells would out grow the intermittently treated cells. Additionally, transfecting the $BRAF^{V600E}$ construct in these cells may shorten the time it takes for the continuously treated cells to grow out.

A.3 C32

Like WM115 cells, we initially tried several LGX818 concentrations for their response to intermittent drug treatment. Again, we did not have a pre-defined intermittent schedule, but decided after each assay whether we would switch to drug-on/drug-off. There were no continuously treated cells for this experiment. The C32 cells grew out with 0.05 nM or 0.5 nM LGX818 drug treatment, but significantly regressed with LGX818 treatment at 5 nM and higher (Fig. A.7). After 13 days it looked like the cells numbers had leveled out, so we switched to drug-off. The cell numbers for day 15 were not much different than day 13. Two days later on day 17, cell numbers greatly increased, so the cells were switched back to drug on. Drug re-addition lead to a decrease in cell numbers over 6 days. We then switched to a drug holiday on day 23. Interestingly, the cells didn't expand as quickly in this second drug holiday. There was essentially no regrowth between days 23 and 29 for 50 nM and 500 nM treated cells. The 5 nM treated cells did show increased cell numbers 6 days after drug withdrawal on day 29.

We tried this experiment again to compare intermittent vs continuous treatment. We also used two different intermittent treatment schedules for 5 nM and 50 nM LGX818. Using the PrestoBlue viability assay allowed us to repeatedly measure the same cells without sacrificing them.

C32 cells continuously treated cells did not significantly outgrow after 35 days of treatment with 5 nM or 50 nM LGX818 (Fig. A.8). Some of the continuously treated wells started to show colony growth, but the overall cell numbers stayed well below confluency.

The wells treated with a 4 days-on/3 days-off schedule on 5nM LGX818 started to regrow on day 9, which was 2 days after the first drug re-addition (Fig. A.8A). The C32 cells on a 4/3 schedule only started to regress between days 2 and 4 of drug re-addition. For the last drug-on cycle we kept the drug on for 7 days. These cells had significantly reduced cell numbers between day 32 and 35. Over the whole course of treatment, the 4/3 schedule out grew cells that only had a single drug holiday break between days 18-23. During this break they started to significantly outgrow the

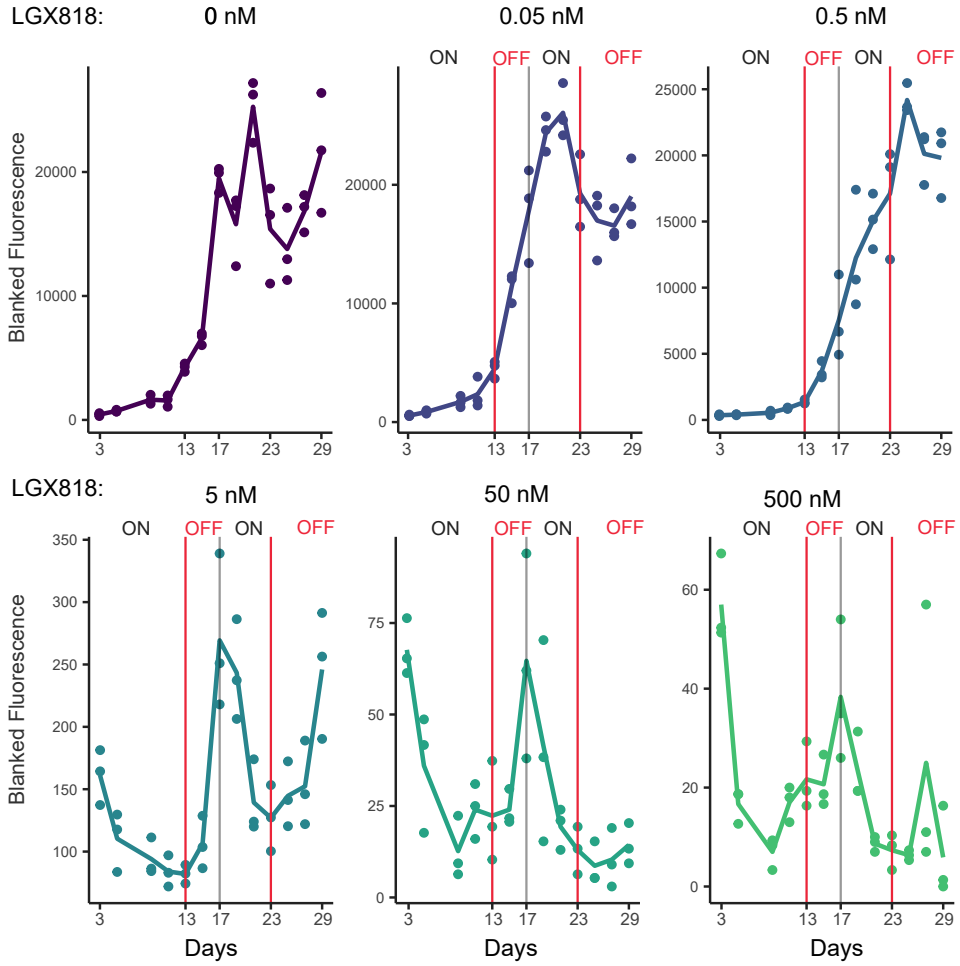

Figure A.7: C32 Intermittent LGX818 treatment. C32 cells were treated intermittented with various concentrations of LGX818, and cell viability was measured repeatedly using PrestoBlue. Cells treated with 5 nM, 50 nM, and 500 nM showed promise for a beneficial intermittent treatment response.

continuously treated cells, but the drug treatment from days 23-35 reduced their cell numbers to match the continuous treated cells. The cells treated with 50 nM LGX818 were suppressed during the whole course of the experiment (Fig. A.8B). Drug holidays did not make the cells grow out. This is presumably because there were so few cells, and cells will not proliferate quickly at low cell densities. There was colony growth in a couple wells of 50 nM continuously treated cells, but not intermittently treated cells. This may be due to random clones, and not anything to do with continuous vs intermittent treatment.

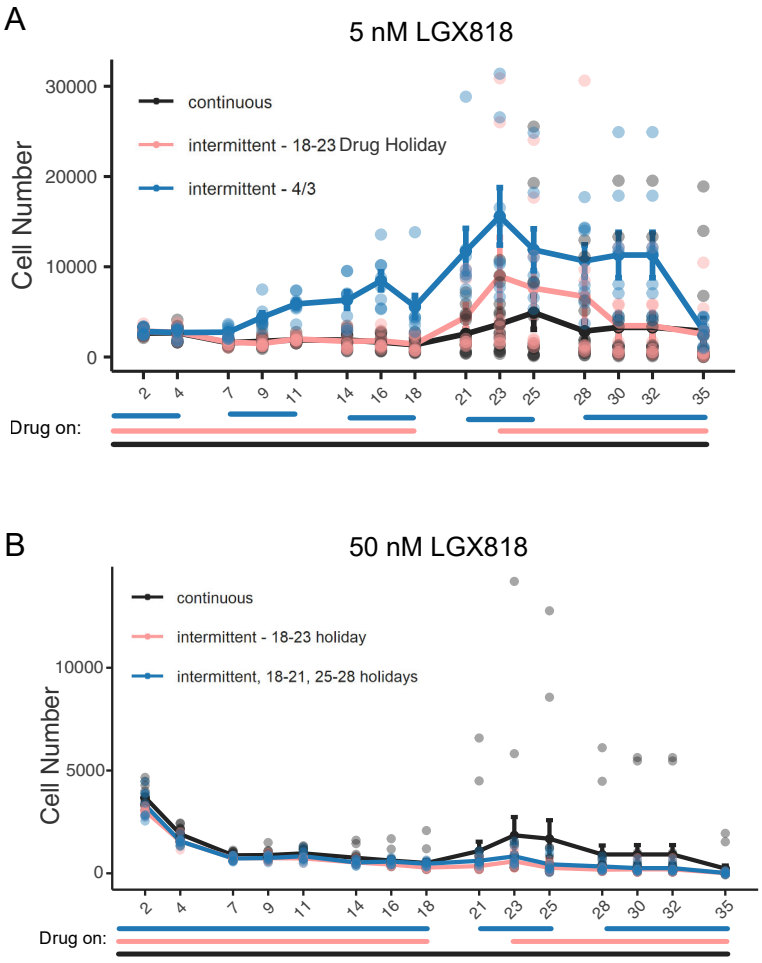

Figure A.8: C32 Continuous vs. Intermittent LGX818 treatment. C32 cells were treated continuously or intermittently with 5 nM and 50 nM LGX818. Cell viability was measured repeatedly with PrestoBlue. The intermittent schedule varied between the two drug concentrations. The solid line indicates when the cells in each schedule were under drug treament.

From the 5 nM LGX818 4 days-on/3 days-off, it seems like 4 days on drug was too short of a period to see significant cell number loss. Extending the drug on period to 7-days lead to significant loss of cells to approximately match the cell numbers of continuously drug treated cells. Like WM115s, the continuously treated cells did not grow out. This means that the length of the experiment may need to be longer to see a beneficial intermittent treatment effect. It is promising that the C32 cells still responded to drug after drug holidays. This may mean that if continuously treated cells start to proliferate under drug, intermittent treatment may show reduced cells numbers. Transfecting the $BRAF^{V600E}$ inducible construct may also speed up the time it takes for continuously treated cells to outgrow intermittently treated cells.

A.4 A375

We also tested A375 for their growth responses in intermittent vs continuous treatment schedules. These cells grow faster than the other cells lines used, so I thought they might benefit from a shorter drug-off period to reduce out growth. Thus, we used a 4 days on/3 days off intermittent schedule vs continuous drug treatment. These were seeded at 250 or 500 cells per well of a 96 well plate and treated with 500 nM or 1 μM of LGX818. The intermittently treated cells significantly outgrew the continuous during the 3 day drug holiday (Fig. A.9). Cells treated with a higher concentration of LGX818 grew out slower during the drug holiday compared to the lower concentration. This might be due to the slow off-rate of LGX818. Upon drug re-addition, the cells did not die, which typically happens at high cell densities. The continuously treated cells did proliferate over the 11 days of treatment, indicating that they show adaptive drug tolerance to these drug concentrations

A.5 WM164

The WM164 is another $BRAF^{V600E}$ melanoma cell line we tested for its response to intermittent drug treatment. Again, we only did an intermittent schedule and not continuous schedule for this cell line. The cells were assayed every 2-3 days using PrestoBlue. WM164 cells grew very

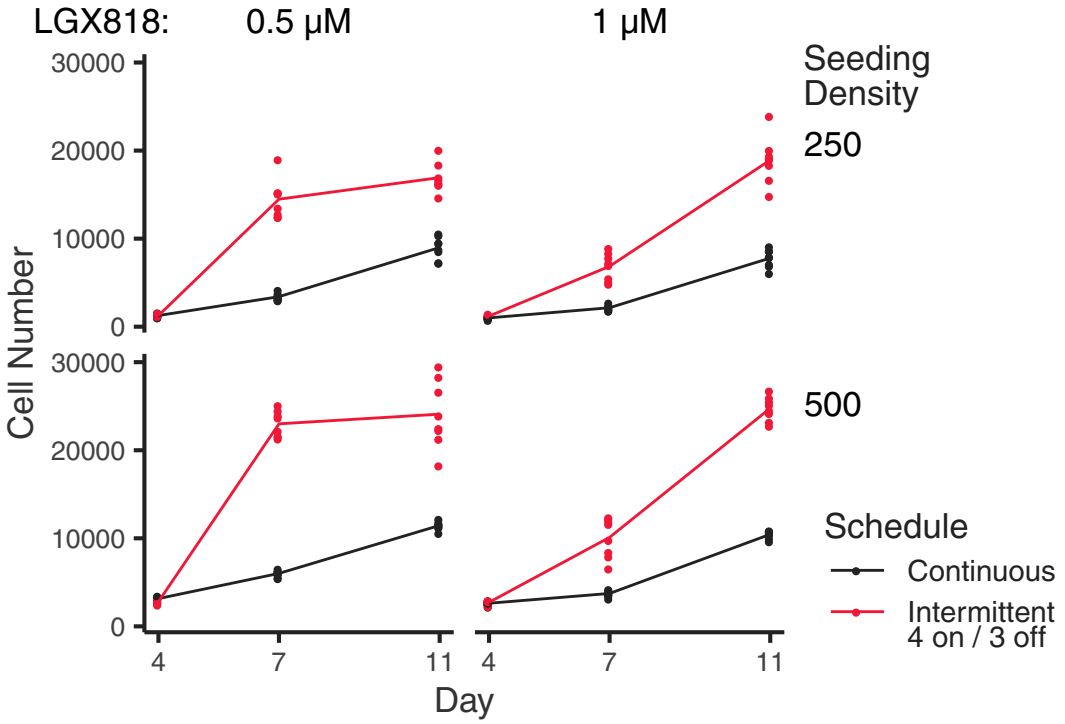

Figure A.9: A375 Continuous vs. Intermittent LGX818 treatment. A375 cells wre seeded in 96 well plates at different initial densities and were treated continuously or intermittently with LGX818 at 0.5 μM or 1 μM. The intermittent schedule was 4 days-on/3 days-off, and CellTiter-Glo 2.0 was used to measure cell viability. The A375 cells quickly outgrew the continuously treated cells during drug withdrawal, and did not decrease in cell numbers after drug re-addition.

fast, similar to the rate of A375 cells. Across all drug concentrations of LGX818 we used, the WM164 cells significantly grew out (Fig. A.10). The cells numbers did not decline for any drug concentration upon drug rechallenge. This is not a promising sign that they would ever show an intermittent treatment response. However, it may be worth trying a shorter drug holiday than 7 days.

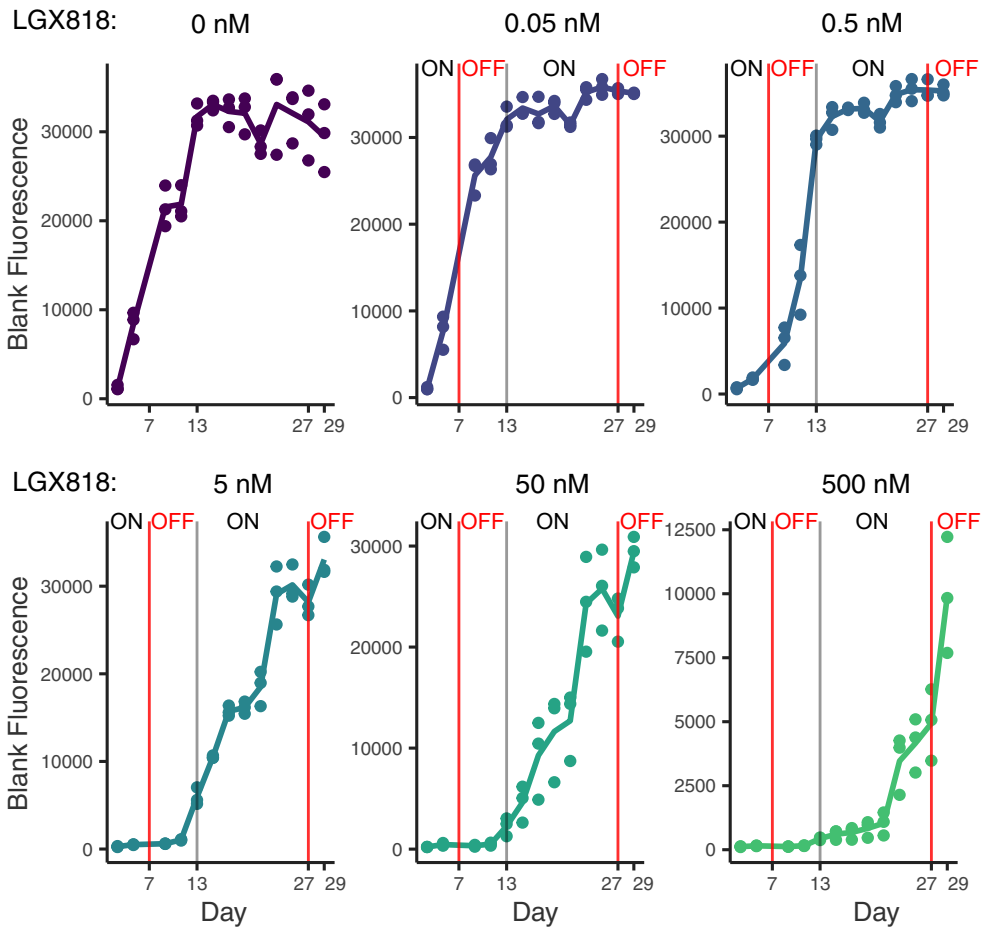

Figure A.10: WM164 Intermittent LGX818 treatment. WM164 cells were treated intermittently with the indicated concentration of LGX818. These cells were largely unresponsive to drug re-addition, and grew out significantly.

Appendix B

Investigating the role of neural cell adhesion molecule L1CAM in drug tolerance of melanoma

In this appendix, I expand on the work I performed to test the role of L1CAM in drug tolerance. In Chapter 2, I show that L1CAM expression is increased upon drug removal, and it reverts upon drug withdrawal in an adaptive, non-selection manner. We want to further test if knocking down L1CAM after 7 days of drug treatment can revert cells to a more sensitive state. If cells lose fitness with L1CAM knockdown while under continuous LGX818 drug treatment, this would be evidence that L1CAM expression may be a bona fide marker for the drug tolerant cell state.

B.1 L1CAM knockdown by siRNA

We first wanted to determine how well siRNAs could knockdown L1CAM expression in our cell line. We transfected 25 nM control non-targeting siRNAs or L1CAM targeting siRNAs using Lipofectamine 3000. We used a pool of 4 different L1CAM targeting siRNAs and long with the individual siRNAs. L1CAM expression was quantified by western blotting. Both the pooled control, and individual control siRNAs had high L1CAM expression, and there was not much variance between them (Fig. B.1). All of the L1CAM targeting siRNAs showed knockdown, with the one labeled "2" being the most efficient. Interestingly, the individual siRNAs had stronger or at least as strong knockdown as the pool of all 4 siRNAs.

We also tested the transfection efficiency of the siRNA. For this experiment, the pooled

L1CAM siRNA was transfected at either 25 nM or 50 nM and compared to mock transfection (no siRNA). After 72 hours, we stained the cells using a fluorescently labeled L1CAM primary antibody and analyzed protein expression by flow cytometry. Both concentrations knocked down L1CAM expression in many cells, and the L1CAM signal significantly overlapped with unstained cells (Fig. B.2). Interestingly, the distribution of L1CAM expression was essentially the same for both 25 nM and 50 nM siRNA. Thus, for future experiments 25 nM siRNA was typically used.

B.2 Effect of L1CAM knockdown on continuously drug treated cells

We wanted to test if L1CAM knockdown could reverse drug tolerance in WM239A-BRAF^{V600E} cells. Cells were cumate induced for 72 hours and seeded in 96 well plates at different densities. The cells were treated with 500 nM LGX818 for 7 days. Based on our Chapter 2 data, this leads to an increase in the IC_{50} by about 10-fold. On day 7 of drug treatment, we transfected the cells with 25 nM pool L1CAM siRNA or control pool siRNA, or didn't transfect the cells. Cell viability was assayed by CellTiter-Glo 2.0 on day 10 (3 days post-transfection) and day 14 (7 days post-transfection). For wells with 500 cells or 1000 cells initial seeding density, the L1CAM knockdown reduced cell fitness compared to the control siRNA and untransfected (Fig. B.3). However, there was no effect due to knockdown at the highest seeding density. The conclusion from this experiment was that L1CAM is necessary for fitness of WM239A-BRAF^{V600E} under the presence of drug, but the result is density dependent.

To determine if the result is reproducible, I repeated this experiment 3 times, but I did not see any difference in growth due to L1CAM knockdown. These experiments were done 3-5 months later than the first due to the COVID-19 stay-at-home orders. We figured the negative results may be due to siRNA degradation making knockdown less efficient. Thus, we ordered a new batch of siRNAs. We also wanted to test if the individual siRNAs might inhibit growth better than the pooled siRNA. We repeated the experiment, seeding 1000 cells per 96 well dish. Cells were treated for 7 days with LGX818 before the transfection of siRNA, or mock conditions. Cells were kept under continuous drug treatment for the whole 14 day experiment.

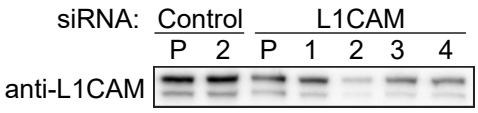

Figure B.1: L1CAM siRNA knockdown efficiency. WM239A-BRAF^{V600E} cells that have been grown under drug for several months express high L1CAM. The cells were treated with 25 nM of the indicated siRNA, and lysates were harvested 72 h later for western blotting. Control siRNAs were non-targeting (P is Dharmacon SmartPool, # is individual siRNA ID).

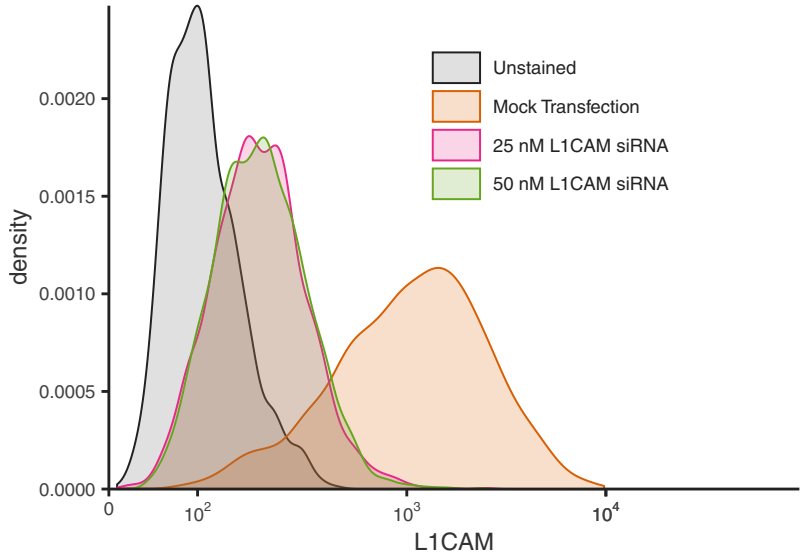

Figure B.2: L1CAM siRNA transfection efficiency. WM239A cells were transfected with the Dharmacon SmartPool siRNA for L1CAM or mock treated with just Lipofectamine 3000. After incubating for 72 h, the cells were prepared for flow cytometry with a fluorescently labeled L1CAM primary antibody.

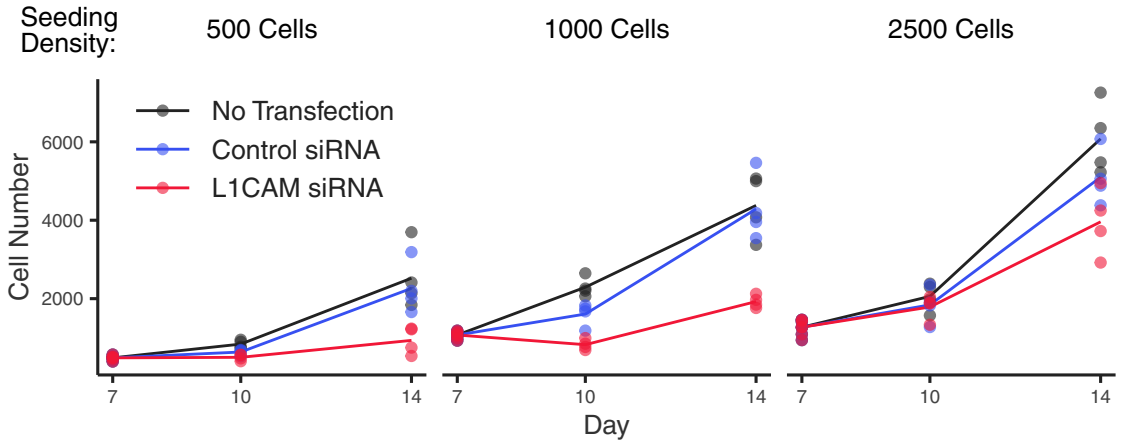

Figure B.3: L1CAM knockdown with pooled siRNA reduces fitness with LGX818 treatment. WM239A-BRAF^{V600E} cells were induced with cumate for 72 h and plated at the indicated densities in 96 well dishes. Cells were continuously treated over 14 days with 500 nM LGX818. On day 7 of drug treatment, the cells transfected with 25 nM control or L1CAM Dharmacon SmartPool siRNAs or not transfected. Cell viability was measured using the CellTiter Glo assay.

The L1CAM pooled siRNA did show reduced cell numbers compared to the control siRNA and mock conditions (Fig. B.4). The difference between the control siRNA and pooled L1CAM siRNA increased over the 7 days of drug treatment. However, the individual siRNAs did not show the same enhanced reduction in cell numbers. L1CAM siRNA number 2 had similar number to the control, while L1CAM siRNAs 3 and 4 had higher cell numbers. While the pooled siRNA has all these individual siRNAs in it, for some reason they didn't show the same growth defect. Of course, we didn't test L1CAM siRNA 1 in this experiment, because it had the least efficient knockdown. Perhaps, that siRNA could be the reason why the pooled L1CAM siRNA transfected cells showed the greatest loss of fitness. More simply, it could be an off-target effect that is exaggerated by multiple siRNAs. This could make sense, as the pooled siRNA had less knockdown efficiency in a western blot than these individual siRNAs (Fig. B.1). This experiment was done at a much lower cell density than the conditions for the Western Blot, so the ratio of siRNA to cell is greater. Thus, the western blot may not show the actual level of knockdown in this particular experiment. The pooled control siRNA also showed a growth defect to the OptiMEM and OptiMEM + Lipofectamine mock transfection conditions, which is problematic and could be indicative that the siRNA is stressing the cells. Since this siRNA experiment has been repeated several times with mixed results, L1CAM simply may not be important for cell fitness under continuous LGX818 drug treatment.

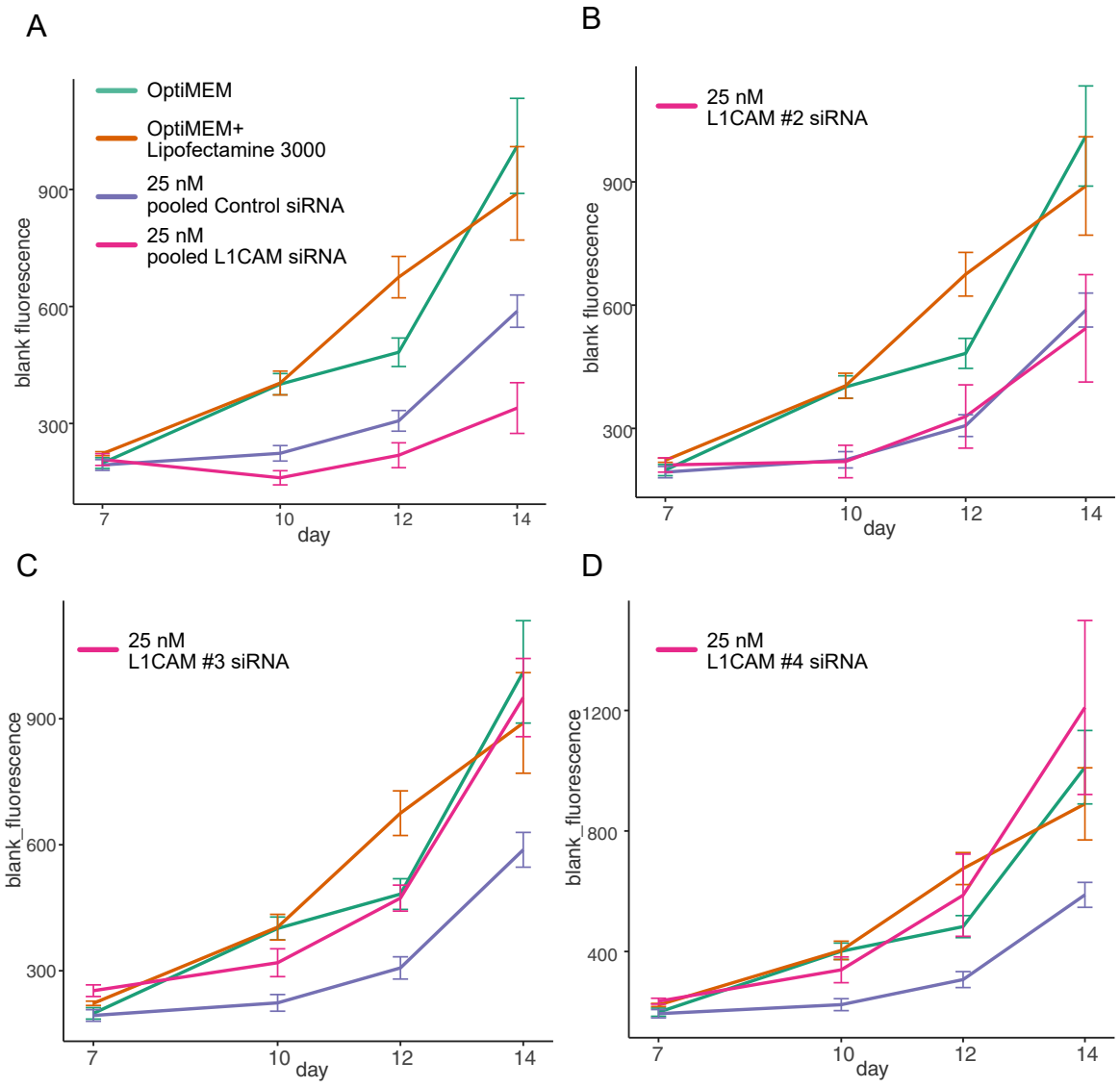

Figure B.4: L1CAM knockdown may not affect fitness under LGX818 treatment. 96 well plate was seeded at 1000 cells per well, and treated with 500 nM LGX818 for 7 days. Then cells were transfected with pooled control siRNA or **A** pooled L1CAM siRNA, **B** L1CAM siRNA # 2, **C** L1CAM siRNA # 3, **D** L1CAM siRNA # 4. Cells were treated continuously with 500 nM LGX818 for 7 more days, and cell viability was measured repeated with the PrestoBlue assay. Note that the OpiMEM, OptiMEM + Lipofectamine, and siRNA control growth curves are repeated in each panel for an easier comparison.